Ion-photon entanglement over a 17 km-long optical fibre deployed across Innsbruck

A master's thesis submitted to the faculty of mathematics, computer science and physics, of the University of Innsbruck in partial fulfillment of the requirements for the degree of

Master of Science (MSc)

carried out at the Institute of Experimental Physics
under the supervision of

Assoc. Prof. Dr. Benjamin Peter Lanyon (principal supervisor),
Dr. Viktor Krutianskii (co-supervisor)

presented by

Tatjana Runggaldier

October 31, 2025

Abstract

Quantum networks offer new possibilities for secure communication, distributed quantum computing, and precision sensing. A key challenge in building such networks is the faithful distribution of photons entangled with matter-based quantum systems over long distances via deployed optical fibres that traverse, e.g., cities and eventually countries. This thesis reports on entanglement between the electronic state of a single trapped $^{40}\mathrm{Ca}^{+}$ ion and the polarisation of a photon transmitted through 17 km of deployed optical fibre across and beyond the city of Innsbruck. The fibre is characterised in detail, with particular attention to drifts in the polarisation of light sent through it. Polarisation drift compensation of polarised light sent through the 17 km-long deployed fibre is performed and represents a key part of this thesis. Single polarised photons emitted from a $^{40}\mathrm{Ca}^{+}$ ion are then sent through the deployed fibre and their polarisation is measured. Finally, photons that are entangled with a $^{40}\mathrm{Ca}^{+}$ ion are sent through the fibre and the joint distributed ion-photon state is measured. The highest probability of generation, transmission and detection of ion-entangled photons achieved is 0.00104(4). The fidelity of the ion-photon entangled state with respect to an ideal Bell state reaches up to 0.89(3), proving that the distributed ion-photon state is strongly entangled. These results represent a key step toward practical implementations of quantum networks using trapped ions and existing fibre infrastructure.

Zusammenfassung

Quantennetzwerke bieten neue Möglichkeiten für sichere Kommunikation, verteiltes Quantencomputing und Präzisionssensoren. Eine Herausforderung beim Aufbau solcher Netzwerke besteht in der Verteilung von Photonen, die mit anderen Quantensystemen verschränkt sind, über große Entfernungen mittels optischer Glasfasern, die beispielsweise Städte und Länder durchqueren. Diese Arbeit befasst sich mit der Verschränkung zwischen dem elektronischen Zustand eines einzelnen gefangenen $^{40}\mathrm{Ca}^{+}$-Ions und der Polarisation eines Photons, das durch eine 17 km lange optische Glasfaser durch die Stadt Innsbruck und darüber hinaus übertragen wird. Die Glasfaser wird umfassend charakterisiert, wobei besonderes Augenmerk auf Veränderungen in der Polarisation des durch sie gesendeten Lichts gelegt wird. Ein zentraler Bestandteil dieser Arbeit ist die Kompensation der Polarisationsänderung des durch die Glasfaser gesendeten Lichts. Polarisierte Photonen, die von einem $^{40}\mathrm{Ca}^{+}$-Ion emittiert werden, werden durch die Glasfaser gesendet und ihre Polarisation wird analysiert. Schließlich werden Photonen, die mit einem $^{40}\mathrm{Ca}^{+}$-Ion verschränkt sind, durch die Glasfaser gesendet und der Ion-Photon-Zustand wird gemessen. Die höchste erreichte Wahrscheinlichkeit für die Erzeugung, Übertragung und Detektion von Photonen beträgt 0,00104(4). Die Güte des Ion-Photon-Verschränkungszustands in Bezug auf einen idealen Bell-Zustand erreicht bis zu 0,89(3), was beweist, dass der Ion-Photon-Zustand stark verschränkt ist. Diese Ergebnisse stellen einen wichtigen Schritt in Richtung der praktischen Umsetzung von Quantennetzwerken unter Verwendung gefangener Ionen und bestehender Glasfaserinfrastruktur dar.

Contents

List of Acronyms

AOD	acousto-optic deflector
AOM	acousto-optic modulator
BCMRT	bichromatic cavity-mediated Raman transition
CMRT	cavity-mediated Raman transition
cps	counts per second
DFG	difference frequency generation
DQS	Distributed Quantum Systems group at the University of Innsbruck
EMCCD	electron-multiplying charge-coupled device
FBG	fibre Bragg grating
FPGA	field-programmable gate array
FWHM	full width at half maximum
GL	Glan-laser polariser
HWP	half-waveplate
IDE	integrated development environment
IKB	Innsbrucker Kommunalbetriebe
IQOQI	Institute for Quantum Optics and Quantum Information
LAN	local area network
MC	Monte Carlo
NEG	non-evaporable getter
OTDR	optical time domain reflectometer
PBS	polarising beam splitter
PDL	polarisation-dependent loss
PMT	photo-multiplier tube
PPLN	periodically poled lithium niobate
QFC	quantum frequency conversion
QGIS	quantum geographic information system
QWP	quarter-waveplate
RF	radio-frequency
SNSPD	superconducting nanowire single photon detector
TTL	transistor-transistor logic
USB	Universal Serial Bus
ZID	Zentraler Informatik Dienst at the University of Innsbruck

1. Introduction

Quantum technologies are ushering in a new era of information processing. Unlike computers made from classical systems, computers made from quantum systems rely on quantum bits (in short, qubits, describing units of quantum information) that can exist in multiple states at once, enabling entirely new ways to store and process data. Quantum systems have the potential to solve complex scientific problems [1–3], increase the security of communication [4, 5], and enable new forms of sensing [6, 7]. Envisioned networks of such quantum systems, called *quantum networks*, are made up of two main components [8, 9]. The first component is a set of matter-based systems that can compute and store quantum information. These matter-based systems are referred to as network nodes. The second component is a set of connections between nodes that carry quantum information, encoded in photons and sent through optical fibres or free space. These connections of the network are called quantum channels [8, 9]. Entanglement is a fundamental phenomenon in quantum mechanics where two or more quantum systems become interconnected in such a way that the state of one system cannot be described independently of the state of the other(s). The ability to distribute entanglement between the nodes of a quantum network is the key to many of the applications of quantum networks [10–13].

The first experiment to establish and store entanglement between two remote matter-based qubits, each representing the node of a network, was reported in 2007 [14]. Specifically, the authors entangled the electronic states of remote atomic ions, each in separate traps a few metres apart. Since then, significant progress has been made in entangling remote ions. One such advancement is the entanglement of two ions separated by two metres, approaching the fidelity and rate of local operations [15]. Another milestone was the first entanglement of two ions located in different buildings, using two completely independent setups [16]. Beyond trapped ions, remote entanglement has also been demonstrated in other quantum systems, including neutral atoms [17], nitrogen-vacancy centres [18], and quantum dots [19].

To build quantum networks with nodes separated by kilometres and connected via optical fibres, the transmission probability of photons through these fibres must be optimised. Photons at telecom wavelengths experience significantly lower losses in optical fibres compared to other wavelengths. Therefore, photons, such as those emitted from ions and intended to be entangled with the ions, should either be generated at, or converted to, telecom wavelengths. The first experimental demonstration of the quantum conversion of single photons emitted from a quantum system from one wavelength to another – known as quantum frequency conversion (QFC) – was reported in 2012 [20]. Efforts to apply QFC to photons emitted by ions began in 2018 and were reported in Refs. [21–23]. In our group, the Distributed Quantum Systems group at the University of Innsbruck (DQS), QFC has been used to demonstrate ion-photon entanglement over 50 km of optical fibre in 2019 [23], to realise a telecom-wavelength quantum repeater node in 2023 [24], and to demonstrate multimode ion-photon entanglement over 101 km in 2024 [25]. However, these results were achieved using fibre spools located within our lab.

A current challenge is to move beyond the lab and build a quantum network using fibres that are deployed outside of the lab. Fibre deployed outside the controlled environment of a lab is exposed to various external conditions, such as temperature fluctuations, mechanical stress and strain, sunlight, artificial lighting, and optical crosstalk from adjacent fibres. Before the start of my master's project (January 2024), work involving the use of matter-entangled telecom photons going over fibres deployed outside of labs has been reported using a quantum dot [26], single atoms [27] and a solid-state quantum memory [28].

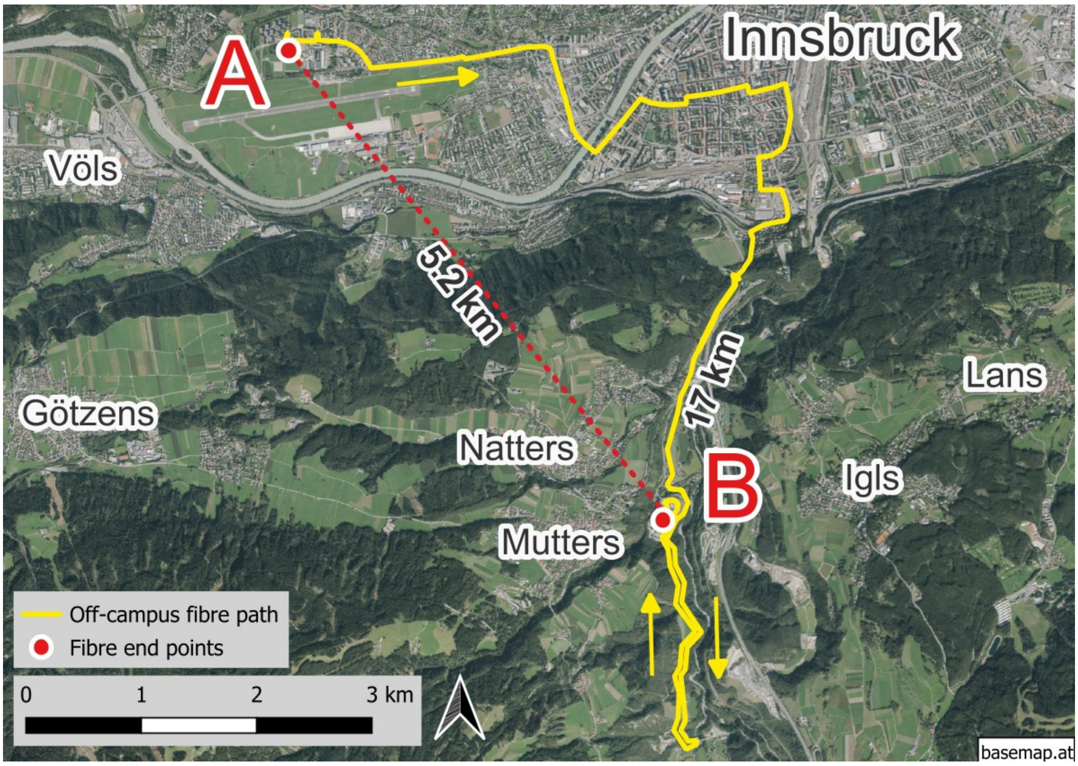

Figure 1.1: Fibre path from Technik campus (A) to Mutters (B). The fibre network consists of two fibres, which follow the path shown in yellow. One end of the fibres, labelled A, is located in the room 1/33 (Lanyon lab) on the first floor of the Viktor-Franz-Hess Haus at Technikerstraße 25, Innsbruck. This building is situated on the Technik campus of the University of Innsbruck. The other end, labelled B, is in an office on the top floor of the building at Gewerbepark Mutters-Gärberbach 7, which serves as a storage facility for the university library. The height difference between the two locations is 0.1 km, estimated using the quantum geographic information system (QGIS)[1] software [29]. The fibre path shown is our best estimate, based on the locations of 29 joining points provided by Innsbrucker Kommunalbetriebe (IKB), and has a total length of approximately 17 km. Arrows indicate the direction of the fibre path from A to B. The entire figure was created using the QGIS software [29], with basemap.at [30] as the source of the geographical map (satellite imagery from 2022, available as open source).

---

[1] The use of the name "quantum" in QGIS has nothing to do with quantum mechanics.

This thesis reports on the effort to measure ion-photon entanglement that extends beyond the lab using infrastructure provided by a commercial telecommunications company for the transmission of single photons. Specifically, the setup used in this thesis consists of one ion trap (the network node), a 17 km-long off-campus fibre path (the quantum channel), and a photon detection station. The ion trap is located in room 1/33 (called from now on Lanyon lab) on the first floor of the Viktor-Franz-Hess Haus at Technikerstraße 25, Innsbruck, which is part of the Technik campus of the University of Innsbruck. The photon detection station is situated in an office on the top floor of the central depot of the library of the University of Innsbruck, located in an industrial zone in the municipality of Mutters. The address is Gewerbepark Mutters-Gärberbach 7. The off-campus fibre path is shown in Figure 1.1, where the location of the Lanyon Lab is labelled as A and the Mutters photon detection station as B. At the time I started with my master's thesis, the setup consisted of the ion trap and the off-campus fibre, which was connected in a loop. In Mutters, the fibre was already installed, but the location was otherwise just a "normal" office with some cabinets, a table, and an office chair, without any lab equipment. Photographs of the Mutters office at the beginning and end of my master's thesis can be found in Appendix A.1.

The goals of this thesis are:

A) Characterise the off-campus fibre path, including background light, changes in the polarisation of transmitted light, transmission efficiency, and polarisation-dependent loss.

B) Perform polarisation drift compensation to correct for changes introduced by the off-campus fibre.

C) Measure the polarisation of polarised photons sent through the off-campus fibre path over time, as well as ion-photon entanglement across the off-campus fibre path.

Other parallel efforts to build deployed quantum networks are underway at several locations. These parallel efforts cited in this paragraph were published in 2024, after the start of my master's project. In Saarbrücken [31], researchers use a trapped ion as a network node and have demonstrated photon-photon entanglement, ion-photon entanglement, and quantum state teleportation. In Boston [32], time-bin encoded photonic qubits are transmitted, received, and stored using a nanocavity-coupled silicon-vacancy centre in diamond. This network spans approximately 40 km of deployed fibre and includes multiple nodes. In Delft/The Hague [33], heralded entanglement was achieved between two independently operated diamond spin qubits, connected via 25 km of deployed optical fibre using QFC to the telecom band.

The content of this thesis is structured as follows: Chapter 2 introduces fundamental concepts of quantum information, including qubits, photon polarisation, and the principles of quantum state and process tomography. These concepts are essential for understanding the results presented in this thesis. Chapter 3 describes the experimental tools and techniques used throughout the thesis, including the network node based on $^{40}\mathrm{Ca}^+$ ions, QFC, and other key established techniques. Chapter 4 details the implementation of the fibre network and its integration into the overall experimental setup. It also introduces the remote photon detection station located in Mutters and describes the setup used for polarisation drift compensation. The core results are presented in three chapters: Chapter 5 discusses the characterisation of the fibre link; Chapter 6 focuses on the implementation and performance of the polarisation drift compensation system; and Chapter 7 presents experiments involving polarised photons and the observation of remote ion-photon entanglement. Finally, Chapter 8 provides a summary of the findings and an outlook on future developments.

2. Concepts of quantum information

This chapter introduces concepts of quantum information that aim to facilitate the understanding of the experiments presented in this thesis. The chapter starts with the fundamentals of quantum information in Section 2.1, discussing quantum states, operations, and measurements. Next, Section 2.2 focuses on how information can be encoded into photon polarisation qubits and on how operations on these qubits can be implemented. Finally, the reconstruction of quantum states and processes from measurements is presented in Section 2.3, including a measure to compare the obtained results.

2.1. Fundamentals of quantum information

The basic concepts in quantum information can be grouped as follows: quantum states, operations, and measurements. The following sections introduce each of these topics. Unless stated otherwise, the formulas given in this section are from Ref. [34].

2.1.1. Quantum states

Quantum information can be encoded in a two-level system known as a quantum bit (in short *qubit*), whose state is described by a unit vector in a two-dimensional complex vector space known as Hilbert space. The vector can be written in Dirac notation using the basis states $|0\rangle$ and $|1\rangle$ in analogy to the classical binary digits (bits) consisting of zeros and ones. In contrast to classical digits, qubits can be in any state $|\Psi\rangle$, which is a wavefunction that is a solution to the Schrödinger equation. The state $|\Psi\rangle$ can be expressed as a linear combination (called *superposition*) of the two orthonormal states $|0\rangle$ and $|1\rangle$ as

$$|\Psi\rangle = \alpha\,|0\rangle + \beta\,|1\rangle \tag{2.1}$$

with complex numbers α and β. The probability of measuring the state $|\Psi\rangle$ in the state $|0\rangle$ is $|\alpha|^2$. The probability of measuring the state $|\Psi\rangle$ in the state $|1\rangle$ is $|\beta|^2$. Since these probabilities must sum to one, the complex numbers must fulfil the normalisation condition $|\alpha|^2 + |\beta|^2 = 1$.

There are a variety of physical systems in which qubits can be and have been encoded. For this thesis, two systems are used. One system is the energy level of the valence electron in the $^{40}\mathrm{Ca}^+$ ion: the states $|0\rangle$ and $|1\rangle$ are represented by a ground electronic state and an excited electronic state of the ion. The second system is the polarisation of a photon: $|0\rangle$ and $|1\rangle$ can be represented by the electric field oscillating in orthogonal directions.

When combining qubits, besides superposition, another fascinating and powerful property of quantum mechanics comes into play: the joint state of two or more qubits can be interconnected in such a way that the state of one system cannot be described independently of the state of the other(s). The consequence is that there are correlations between the two systems that are stronger than those allowed by classical physics, and when this is the case, the quantum systems are called *entangled*. Mathematically, a quantum state composed of two subsystems A and B with the state $|\Psi\rangle_{\mathrm{AB}}$ is called entangled when it cannot be written as a tensor product of the states of the individual subsystems A and B [35]:

$$|\Psi\rangle_{\mathrm{AB}} \neq |\Psi\rangle_{\mathrm{A}} \otimes |\Psi\rangle_{\mathrm{B}} \,. \tag{2.2}$$

Well-known examples of entangled two-qubit states are the four Bell states [35]:

$$\begin{aligned}
|\Phi^+\rangle &= \frac{1}{\sqrt{2}}\left(|00\rangle + |11\rangle\right) \\
|\Phi^-\rangle &= \frac{1}{\sqrt{2}}\left(|00\rangle - |11\rangle\right) \\
|\Psi^+\rangle &= \frac{1}{\sqrt{2}}\left(|01\rangle + |10\rangle\right) \\
|\Psi^-\rangle &= \frac{1}{\sqrt{2}}\left(|01\rangle - |10\rangle\right) .
\end{aligned} \tag{2.3}$$

The Bell states are orthogonal to each other and form a basis for two-qubit states. Furthermore, according to the entanglement measures in Ref. [36–38], each Bell state is a maximally entangled state.

A more general representation of a quantum state than the Dirac representation is the density matrix representation, which expresses the state as a sum of probabilities p_i of finding the system in different states $|\Psi_i\rangle$:

$$\rho = \sum_i p_i \, |\Psi_i\rangle \langle\Psi_i| \,. \tag{2.4}$$

The diagonal elements of the density matrix represent the probabilities of measuring the system in the basis states in which the matrix is expressed. The density matrix is a positive semi-definite operator with trace[2] equal to one: $\mathrm{tr}(\rho) = 1$. In the case where one of the probabilities is equal to one, i.e., $p_i = 1$, the system is thus described by a single wavefunction, e.g., as in Equation (2.1). Such cases with $p_i = 1$ are known as pure. In all other cases where $p_i < 1$, the system is described by a statistical mixture of states, and the state is referred to as mixed. The degree of purity of a state is quantified by the purity $\mathbb{P} = \mathrm{tr}(\rho^2)$.

One can write out the density matrix corresponding to the Bell state $|\Phi^+\rangle$ as a 4×4 matrix by defining the orthonormal basis vectors mathematically as

$$|0\rangle = \begin{pmatrix} 1 \\ 0 \end{pmatrix} \qquad \text{and} \qquad |1\rangle = \begin{pmatrix} 0 \\ 1 \end{pmatrix} . \tag{2.5}$$

Applying Equation (2.4) with $p_0 = 1$, the density matrix of the state $|\Phi^+\rangle$ is

$$\begin{aligned}
\rho_{|\Phi^+\rangle} &= |\Phi^+\rangle \langle\Phi^+| \\
&= \frac{1}{2}\begin{pmatrix} 1 & 0 & 0 & 1 \\ 0 & 0 & 0 & 0 \\ 0 & 0 & 0 & 0 \\ 1 & 0 & 0 & 1 \end{pmatrix} .
\end{aligned} \tag{2.6}$$

---

[2] The trace is defined as the sum of the diagonal elements of the matrix.

The density matrix of a single qubit can be written as a linear combination of the identity matrix

$$\sigma_0 = \begin{pmatrix} 1 & 0 \\ 0 & 1 \end{pmatrix} \tag{2.7}$$

and the Pauli matrices

$$\sigma_1 = \begin{pmatrix} 0 & 1 \\ 1 & 0 \end{pmatrix}, \quad \sigma_2 = \begin{pmatrix} 0 & -i \\ i & 0 \end{pmatrix}, \quad \sigma_3 = \begin{pmatrix} 1 & 0 \\ 0 & -1 \end{pmatrix}. \tag{2.8}$$

The density matrix of an arbitrary one-qubit state is then

$$\rho = \frac{1}{2} \left(\sigma_0 + \sum_{i=1}^{3} r_i \sigma_i \right) \tag{2.9}$$

with the real parameters r_i fulfilling the condition $\sum_{i=1}^{3} r_i^2 \leq 1$. The parameters r_i can be expressed in terms of the density matrix as $r_i = \mathrm{tr}(\sigma_i \rho)$, which corresponds to the definition of an expectation value for operator σ_i given in the upcoming Equation (2.18). The density matrix ρ of n qubits can be expanded in terms of the Pauli matrices σ_i as

$$\rho = \frac{1}{2^n} \sum_{\vec{v}} \mathrm{tr}\left(\sigma_{v_1} \otimes \sigma_{v_2} \otimes \cdots \otimes \sigma_{v_n} \rho\right) \sigma_{v_1} \otimes \sigma_{v_2} \otimes \cdots \otimes \sigma_{v_n}. \tag{2.10}$$

Here, in Equation (2.10), the vectors $\vec{v} = (v_1, \ldots, v_n)$ have components $v_i \in \{0,1,2,3\}$. The representation of the density matrix in Equation (2.10) is useful for characterising quantum states since it is possible to measure the expectation values $\mathrm{tr}\left(\sigma_{v_1} \otimes \sigma_{v_2} \otimes \cdots \otimes \sigma_{v_n} \rho\right)$ and therefore obtain an estimate for the density matrix of the system. In the density matrix ρ of Equation (2.10), there are 4^n expectation values. More information regarding quantum state tomography, and the closely related process tomography, can be found in Section 2.3.

2.1.2. Quantum dynamics

A quantum state can evolve, either by controlled interactions or due to uncontrolled interactions with the system's environment. Controlled interactions relevant for this thesis include idealised electromagnetic fields (lasers) shining onto the $^{40}\mathrm{Ca}^+$ ion, changing its electronic state, as well as birefringent optical elements, changing the polarisation of photons.

Controlled operations are ideally unitary. A unitary operation U has to fulfil the condition $U^\dagger U = \mathbb{1}$, where $U^\dagger$ is the adjoint[3] of U and $\mathbb{1}$ is the identity operator. The unitary operation U acting on a pure state $|\Psi\rangle$ gives the state

$$|\Psi'\rangle = U\,|\Psi\rangle\,. \tag{2.11}$$

---

[3] The adjoint of a matrix is defined as the transposition and complex conjugation of the matrix.

In the case of a time-independent interaction between the control mechanism and the quantum system, the unitary operation can be expressed as a function of time t and the time-independent Hamiltonian H of the system-control interaction as $U(t) = \mathrm{e}^{-iHt/\hbar}$. Therefore, the initial state $|\Psi(t_0)\rangle$ at an initial time t_0, subjected to the interaction for a time t, evolves to the state $|\Psi(t)\rangle = \mathrm{e}^{-iH(t-t_0)/\hbar}|\Psi(t_0)\rangle$. In the notation of density matrices, Equation (2.11) is written as

$$\rho' = U\rho U^\dagger. \tag{2.12}$$

The Pauli operators (corresponding to the Pauli matrices given in Equations (2.7) and (2.8)) are examples of unitary operators. The Pauli operators can also be used to generate arbitrary unitary rotations of a single qubit around three orthogonal axes, denoted as x, y and z, written as

$$\begin{aligned} U_x(\theta_x) &= \exp\left(-i\frac{\sigma_1\theta_x}{2}\right) \\ U_y(\theta_y) &= \exp\left(-i\frac{\sigma_2\theta_y}{2}\right) \\ U_z(\theta_z) &= \exp\left(-i\frac{\sigma_3\theta_z}{2}\right) \end{aligned} \tag{2.13}$$

with rotation angles $\theta_{x/y/z} \in [0, 2\pi]$. Even if an experimenter has access to only two out of the three unitary gates U_x, U_y, U_z, it is possible to decompose an arbitrary rotation into sequences containing any two of the rotations in Equation (2.13) (see Chapter 4 of Ref. [34]).

In contrast to controlled operations, interactions with the environment are typically uncontrolled and thus cause non-unitary evolution. A quantum system subjected to controlled operations or uncontrolled interactions with the environment can be modelled using the operator-sum representation (called a Kraus map). Here, the evolution of the density matrix is described by a map $\mathcal{E}$, where

$$\rho' = \mathcal{E}(\rho) = \sum_k K_k \rho K_k^\dagger \tag{2.14}$$

and K_k are Kraus operators. If the map $\mathcal{E}$ preserves the trace of ρ, i.e., $\mathrm{tr}(\rho) = \mathrm{tr}(\rho')$, then the Kraus operators fulfil the condition $\sum_k K_k^\dagger K_k = \mathbb{1}$ [34].

2.1.3. Quantum measurements

A special class of quantum measurements, which are relevant for this thesis, is formed by projective measurements. A projective measurement is described by the observable

$$M = \sum_m m P_m \tag{2.15}$$

where P_m is the projector onto the eigenspace of M with eigenvalue m, corresponding to the possible measurement outcomes. The projectors can be expressed by $P_m = |m\rangle\langle m|$

using the eigenstates $|m\rangle$ of the observable M. These projectors P_m have to fulfil the completeness relation $\sum_m P_m = \mathbb{1}$ and be orthogonal, i.e., they must be hermitian ($P_m^\dagger = P_m$) and fulfil the condition $P_m P_{m'} = \delta_{mm'} P_m$. The symbol $\delta_{mm'}$ represents the Kronecker delta. When measuring a qubit in the state ρ, the probability of obtaining the measurement outcome m is

$$p(m) = \mathrm{tr}(P_m \rho). \tag{2.16}$$

After the measurement in which the outcome m is obtained, the qubit is left in the state

$$\frac{P_m \rho P_m}{p(m)}. \tag{2.17}$$

The expectation value of the observable M is

$$\begin{aligned} \mathrm{tr}(M\rho) &= \mathrm{tr}\left(\sum_m m\, P_m\, \rho\right) \\ &= \sum_m m\, \mathrm{tr}(P_m\, \rho) \\ &= \sum_m m\, p(m). \end{aligned} \tag{2.18}$$

The last line in Equation (2.18) shows that the expectation value of an observable is directly related to the probabilities $p(m)$, which can be estimated in experiments. In the case of pure states, the probability in Equation (2.16) can be expressed as $p(m) = \langle\Psi| P_m |\Psi\rangle$, Equation (2.17) simplifies to $P_m |\Psi\rangle / \sqrt{p(m)}$, and the expectation value is $\langle M\rangle = \langle\Psi| M |\Psi\rangle$.

For example, assume that the goal is to estimate the expectation value of the observable $M = \sigma_3$. The observable has eigenvalues $m = +1$ and -1 with eigenstates $|0\rangle$ and $|1\rangle$, respectively. The projectors are

$$\begin{aligned} P_{+1} &= |0\rangle \langle 0| \\ P_{-1} &= |1\rangle \langle 1|. \end{aligned} \tag{2.19}$$

The observable σ_3 can be rewritten in terms of its eigenvalues and projectors as

$$\sigma_3 = |0\rangle \langle 0| - |1\rangle \langle 1|, \tag{2.20}$$

and the expectation value is

$$\langle\sigma_3\rangle = p(m = +1) - p(m = -1). \tag{2.21}$$

The probabilities of measuring m can be estimated by measuring copies[4] of a state ρ. Writing the number of occurrences where the measurement outcome is $m = +1$ ($m = -1$) as N_0 (N_1), the probability estimates are

$$\begin{aligned} p(m = +1) &= \frac{N_0}{N_0 + N_1} \\ \text{and} \quad p(m = -1) &= \frac{N_1}{N_0 + N_1}. \end{aligned} \tag{2.22}$$

---

[4] The term “copies” of a state refers to the repetition of the procedure of state preparation.

2.2. Encoding and manipulating photonic polarisation qubits

This section focuses on qubits encoded in the polarisation of photons, and on how operations and measurements can be implemented in an experimental setup for photon polarisation qubits.

2.2.1. Encoding quantum information into photon polarisation

The polarisation of a photon is one possible way to encode a qubit and is used in our experiments. The polarisation is defined as the direction in which the electric field of an electromagnetic wave oscillates. For example, photons travelling in free space have an electric field that is orthogonal to the direction of travel. In this case, the polarisation can be represented by a vector which is a superposition of any two orthogonal polarisation states, such as horizontal[5] (H) and vertical (V). Commonly used superpositions of the polarisation states, written in Dirac notation $|H\rangle$ and $|V\rangle$ (analogously to $|0\rangle$ and $|1\rangle$), are the eigenstates of the Pauli operators σ_1, σ_2, and σ_3. In the following, the commonly used photon states (left side) are listed alongside their analogous qubit states (right side):

$$\begin{aligned}
\text{Horizontal}\quad & |H\rangle & &\longleftrightarrow & & |0\rangle \\
\text{Vertical}\quad & |V\rangle & &\longleftrightarrow & & |1\rangle \\
\text{Diagonal}\quad & |D\rangle = \frac{1}{\sqrt{2}}(|H\rangle + |V\rangle) & &\longleftrightarrow & & |{+}\rangle = \frac{1}{\sqrt{2}}(|0\rangle + |1\rangle) \\
\text{Antidiagonal}\quad & |A\rangle = \frac{1}{\sqrt{2}}(|H\rangle - |V\rangle) & &\longleftrightarrow & & |{-}\rangle = \frac{1}{\sqrt{2}}(|0\rangle - |1\rangle) \\
\text{Right-handed circular}\quad & |R\rangle = \frac{1}{\sqrt{2}}(|H\rangle + i\,|V\rangle) & &\longleftrightarrow & & |{+i}\rangle = \frac{1}{\sqrt{2}}(|0\rangle + i\,|1\rangle) \\
\text{Left-handed circular}\quad & |L\rangle = \frac{1}{\sqrt{2}}(|H\rangle - i\,|V\rangle) & &\longleftrightarrow & & |{-i}\rangle = \frac{1}{\sqrt{2}}(|0\rangle - i\,|1\rangle).
\end{aligned} \tag{2.23}$$

The qubit states will be used later in this thesis to describe ion qubits. When written as 2 × 1 vectors with the basis vectors $|H\rangle = |0\rangle$ and $|V\rangle = |1\rangle$ given in Equation (2.5), the polarisation states in Equation (2.23) are known as *Jones vectors* [39–41]. Another convenient representation of polarisation is given by *Stokes vectors*. In contrast to Jones vectors, Stokes vectors can also describe partially polarised or unpolarised light, where the oscillation direction of the electric field fluctuates randomly. How to convert a Jones vector into a Stokes vector is described in Ref. [42]. The Stokes parameters can be written as a 4 × 1 vector

$$\vec{S} = \begin{pmatrix} S_0 \\ S_1 \\ S_2 \\ S_3 \end{pmatrix} \tag{2.24}$$

---

[5] In this thesis, horizontal polarisation is defined as the electric field oscillating parallel to the optical breadboard surface (perpendicular to the direction of gravity), and vertical polarisation is defined as the electric field oscillating parallel to the direction of gravity. The vertical and horizontal polarisations are perpendicular to each other.

with real components S_i. For single photons, the Stokes parameters S_i are the expectation values of the Stokes operators $\hat{S}_i$:

$$\begin{aligned} S_0 &= \left\langle \hat{S}_0 \right\rangle = \langle \sigma_0 \rangle \\ S_1 &= \left\langle \hat{S}_1 \right\rangle = \langle \sigma_3 \rangle \\ S_2 &= \left\langle \hat{S}_2 \right\rangle = \langle \sigma_1 \rangle \\ S_3 &= \left\langle \hat{S}_3 \right\rangle = \langle \sigma_2 \rangle . \end{aligned} \tag{2.25}$$

The Stokes operators $\hat{S}_1$, $\hat{S}_2$, and $\hat{S}_3$ do not commute [43]. Therefore, measuring the polarisation of a quantum state sequentially on the same photon can yield different results compared to performing measurements on multiple copies of the same quantum state.

The Stokes parameters can be normalised and written as 3×1 vectors. The normalised Stokes parameters are defined as

$$s_i = \frac{S_i}{S_0} \tag{2.26}$$

with $i \in \{1,2,3\}$. The Stokes parameter s_1 reflects the tendency of the polarisation to be H or V polarised. For example, $s_1 = 1$ corresponds to horizontal polarisation, and $s_1 = -1$ to vertical polarisation. Similarly, s_2 (s_3) reflects the tendency of the polarisation to be D (R) or A (L). Table 2.1 gives an overview of the six most important polarisation states, both as Jones vectors and as normalised Stokes vectors.

The density matrix can easily be expressed in terms of the Stokes parameters [44] as

$$\begin{aligned} \rho &= \frac{1}{2} \sum_{i=0}^{3} \frac{S_i}{S_0} \sigma_i \\ &= \frac{1}{2} \begin{pmatrix} 1 + s_3 & s_1 - i s_2 \\ s_1 + i s_2 & 1 - s_3 \end{pmatrix} . \end{aligned} \tag{2.27}$$

Conversely, when the density matrix is known, the normalised Stokes parameters can be computed as $s_i = \mathrm{tr}(\rho \sigma_i)$.

A convenient and often used graphical representation of the normalised Stokes parameters is given by the Poincaré sphere, shown in Figure 2.1. The Poincaré sphere is equivalent to the Bloch sphere used to represent quantum states and operations on the qubit encoded in the electronic state of an ion. The Cartesian axes of the Poincaré sphere correspond exactly to the normalised Stokes parameters in Equation (2.26). The sphere has a radius of 1 due to normalisation. The linear polarisation states lie on the equator of the Poincaré sphere, circular polarisations on the poles, and the rest of the sphere represents elliptical polarisations.

2.2.2. Photon polarisation control and measurement

One way to modify the polarisation of a photon is through the use of birefringent materials, where different polarisations experience different refractive indices. If a birefringent crystal

Table 2.1: Polarisation states with corresponding Jones and Stokes vectors.

	Polarisation State	**Jones Vector**	**Normalised Stokes Vector**
Linearly Polarised	Horizontal $\|H\rangle$	$\begin{pmatrix}1\\0\end{pmatrix}$	$\begin{pmatrix}1\\0\\0\end{pmatrix}$
	Vertical $\|V\rangle$	$\begin{pmatrix}0\\1\end{pmatrix}$	$\begin{pmatrix}-1\\0\\0\end{pmatrix}$
	Diagonal $\|D\rangle$	$\frac{1}{\sqrt{2}}\begin{pmatrix}1\\1\end{pmatrix}$	$\begin{pmatrix}0\\1\\0\end{pmatrix}$
	Anti-diagonal $\|A\rangle$	$\frac{1}{\sqrt{2}}\begin{pmatrix}1\\-1\end{pmatrix}$	$\begin{pmatrix}0\\-1\\0\end{pmatrix}$
Circularly Polarised	Right $\|R\rangle$	$\frac{1}{\sqrt{2}}\begin{pmatrix}1\\i\end{pmatrix}$	$\begin{pmatrix}0\\0\\1\end{pmatrix}$
	Left $\|L\rangle$	$\frac{1}{\sqrt{2}}\begin{pmatrix}1\\-i\end{pmatrix}$	$\begin{pmatrix}0\\0\\-1\end{pmatrix}$

is uniaxial, then the electric field component in an electromagnetic wave passing through the crystal that is parallel to the crystal-specific axis (called the optical axis) travels faster through the crystal than a component that is orthogonal to the crystal's optical axis [45]. The consequence of the different speeds of the two electric field components is that they develop a phase shift with respect to each other when passing through the crystal. The size of the phase shift is a function of the thickness of the birefringent material and the wavelength λ of the light (photons or laser light). The birefringent materials used in this thesis to change the polarisation of light are waveplates, specifically half-waveplate (HWP) and quarter-waveplate (QWP), inducing relative phase shifts of π and $\pi/2$, respectively, of the two orthogonal electric field components. The relative

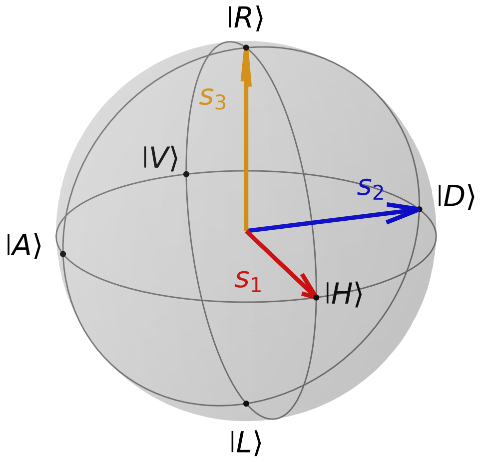

Figure 2.1: Poincaré sphere. Polarisation states can be represented on the Poincaré sphere using the normalised Stokes parameters s_1, s_2, and s_3. The different polarisation states of a qubit are given in Dirac notation.

phase shift of a waveplate is also called the retardance of the waveplate. The waveplates are mounted on rotation stages, such that the angle of the optical axis with respect to a horizontal or vertical reference can be changed. How the optical axis of a waveplate is determined for the experiments presented in this thesis is explained in the Appendix A.2.

The effect of waveplates on polarised light can be described by two different formalisms, depending on whether the Stokes vectors or the Jones vectors are used to represent the polarisation. The Jones formalism is used when the polarisation is described by Jones vectors; the Müller calculus [42] is used when the polarisation is described by Stokes vectors. The next paragraph focuses on the mathematical representation of the effect of waveplates in the Jones formalism.

According to Ref. [45], the Jones matrix for a waveplate with a retardance r, where the optical axis is aligned horizontally, is the following unitary matrix

$$U_{\text{ret}}(r) = \begin{pmatrix} \mathrm{e}^{i\frac{r}{2}} & 0 \\ 0 & \mathrm{e}^{-i\frac{r}{2}} \end{pmatrix} \tag{2.28}$$

up to a global phase. If the optical axis is now rotated by an angle α with respect to the horizontal plane, the reference frame has to be changed, which can be done by the rotation matrix [45]

$$R(\alpha) = \begin{pmatrix} \cos\alpha & \sin\alpha \\ -\sin\alpha & \cos\alpha \end{pmatrix}. \tag{2.29}$$

A matrix describing a waveplate with any retardance and rotation is obtained via [45]:

$$U_{\text{WP}}(r,\alpha) = R(-\alpha)U_{\text{ret}}(r)R(\alpha). \tag{2.30}$$

It is useful to remember that a QWP ($r = \pi$) can transform linearly polarised light into elliptically or circularly polarised light. A HWP ($r = \pi/2$) can convert one linear polarisation to another, which corresponds to rotations of the polarisation state on the equator of the Poincaré sphere (Figure 2.1).

A different way to modify the polarisation of light is the use of polarising elements such as a polarising beam splitter. In this thesis, polarising beam splitter (PBS) cubes are used. Each PBS cube has four facets on which light can be shone. The light entering the PBS cube through one of the facets can be either transmitted or reflected, depending on the polarisation of the light, as shown for example in Figure 2.2. The facet where the transmitted light leaves the PBS cube is called the transmission port; the facet where the reflected light leaves the PBS cube is called the reflection port. The polarisation axis of the PBS is defined as the direction of linear polarisation that is transmitted through the PBS. If the polarisation of the light shining onto the PBS is parallel to the polarisation axis, the transmission through the PBS is maximal. If the incoming polarisation is perpendicular to the polarisation axis, then the transmission is minimal, but the reflection is maximal. The extinction ratio (defined as the ratio of the maximal to the minimal transmission through the PBS cube) is one measure to quantify how close the PBS is to an ideal PBS.

A way to estimate a Stokes parameter describing the polarisation of a photon is described in this paragraph, for simplicity assuming that optical elements and detectors are ideal. To measure a polarised photon's Stokes parameter, it is possible to use a HWP, a QWP and a PBS cube, at whose output ports single-photon detectors are placed [45], as sketched in Figure 2.2. A measurement operator can be set by choosing the corresponding angles of the HWP and the QWP.

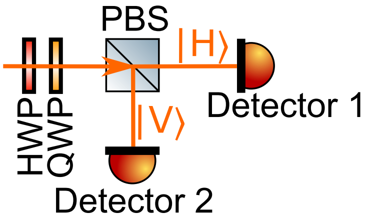

Figure 2.2: Photon polarisation detection setup. The sketch shows a simple setup to measure the polarisation of photons with two waveplates (a HWP and a QWP), a PBS and two photon detectors (Detector 1 and Detector 2).

To start with, consider the case where there are no waveplates in the setup to measure the polarisation of a photon. If the polarisation of the photon is aligned with the polarisation axis of the PBS, then the detector at the transmission port detects the photon. When a photon is detected, we say that the detector "clicks". Similarly, if the incoming photon is orthogonally polarised to the polarisation axis of the PBS, the detector at the reflection port clicks. This procedure measures the polarisation state in the basis set by the projective measurement with $|H\rangle$ and $|V\rangle$ eigenstates and, after many repeated instances, can give an estimate for the s_1 parameter using Equation (2.18). An estimate of s_2 can be obtained by adding a HWP in front of the PBS. Inserting $r = \pi$

into Equation (2.30), one obtains the matrix for an ideal HWP [45]

$$\begin{aligned} U_{\mathrm{HWP}}(\alpha) &= U_{\mathrm{WP}}(r=\pi,\alpha) \\ &= \mathrm{e}^{i\frac{\pi}{2}} \begin{pmatrix} \cos 2\alpha & \sin 2\alpha \\ \sin 2\alpha & -\cos 2\alpha \end{pmatrix}. \end{aligned} \tag{2.31}$$

If the waveplate is set at an angle of $\alpha = 22.5°$, then the input state $|D\rangle$ ($|A\rangle$) is mapped onto $|H\rangle$ ($|V\rangle$). Therefore, an incoming photon in the state $|D\rangle$ will now lead to the detector in the transmission output port clicking, and likewise an incoming photon in the state $|A\rangle$ will lead to the detector in the reflection port clicking. Such an operation corresponds to a basis rotation followed by a projective measurement. Adding now a QWP ($r = \pi/2$) between the HWP and the PBS cube, with the QWP set to 45° and the HWP set to 0°, allows one to distinguish R/L polarisations. So, to get an estimate of the normalised Stokes parameters, let N_{H} and N_{V} be the number of occurrences (detector clicks) where the photons are measured in the $|H\rangle$ and $|V\rangle$ basis. Similarly, let N_{D} (N_{R}) and N_{A} (N_{L}) be the number of occurrences where the photons are measured in the $|D\rangle$ ($|R\rangle$) and $|A\rangle$ ($|L\rangle$) basis. Estimates of the normalised Stokes parameters are then (as in Equations (2.21) and (2.22), using Equation (2.18)) ideally given by

$$\begin{aligned} s_1 &= \frac{N_{\mathrm{H}} - N_{\mathrm{V}}}{N_{\mathrm{H}} + N_{\mathrm{V}}} \\ s_2 &= \frac{N_{\mathrm{D}} - N_{\mathrm{A}}}{N_{\mathrm{D}} + N_{\mathrm{A}}} \\ s_3 &= \frac{N_{\mathrm{R}} - N_{\mathrm{L}}}{N_{\mathrm{R}} + N_{\mathrm{L}}}. \end{aligned} \tag{2.32}$$

The Stokes parameters in Equation (2.32) are an idealisation, since in reality two factors affect the estimates. Firstly, the number of trials in an experiment is finite, meaning that the estimates s_1, s_2 and s_3 have uncertainties. Under the circumstance that the photon counts can be counted individually, that they are independent from each other, and that the average counting rate is constant, the uncertainties of the number of counts N_i correspond to the square root $\sqrt{N_i}$, according to Poisson statistics. Secondly, the two detectors at the output of the reflection and transmission ports of the PBS cube may not have the same efficiency, or the different ports of the PBS may not have the same losses, which would distort the estimates. To make the estimates independent of the detector efficiencies, the waveplates can be set to first send horizontally polarised photons to Detector 1 in Figure 2.2 (measuring in the H/V basis), yielding $N_{\mathrm{H},1}$ clicks, and then switched to send horizontally polarised photons to Detector 2 in Figure 2.2 (measuring in the V/H basis), yielding $N_{\mathrm{H},2}$ clicks. The counts from the two measurements can then be summed to obtain the detector-efficiency independent number $N_{\mathrm{H}} = N_{\mathrm{H},1} + N_{\mathrm{H},2}$. Using the same procedure for the photon counts in the other polarisation states, detector-efficiency independent parameters s_i can be obtained.

When working with polarised photons, one has to keep in mind that any optical element can change the polarisation state in a potentially uncontrolled way. For example, mirrors and optical fibres might be used to send photons through several setups and induce an undesired change in polarisation of the photons. Optical fibres, which play a central role in this thesis, are birefringent. If the fibre is subjected to stress, strain or changing temperature, its birefringence changes.

Up to this point, the description of polarisation has been discussed mainly for single photons. However, laser light, being an electromagnetic wave with an electric field component, can also be polarised. The Stokes parameters can be measured on laser light by replacing the photon detectors with optical power metres and substituting the number of detector clicks N_i ($i \in \{\mathrm{H}, \mathrm{V}, \mathrm{D}, \mathrm{A}, \mathrm{R}, \mathrm{L}\}$) in Equation (2.32) with measured powers. The Stokes parameter S_0 corresponds to the total power of the light. The analogy extends further: not only is the description of polarisation of light analogous to the description of the polarisation of single photons, but the implementation of unitary operations using waveplates applies equally in both quantum and classical contexts.

2.2.3. Implementation of any unitary operation with waveplates

While a HWP and a QWP are sufficient to convert any linearly polarised input state to any other possible polarised state, two waveplates are not enough to perform an arbitrary unitary operation on the polarisation of light. A combination of three sequential waveplates is sufficient [46]: a QWP, a HWP and another QWP, which will be denoted as QHQ from now on. The three waveplates and the respective rotation angles are drawn in Figure 2.3. Any 2×2 unitary with a determinant equal to 1 (known as an SU(2) operator) can be decomposed as a product of waveplate operations in this QHQ configuration [47–49].

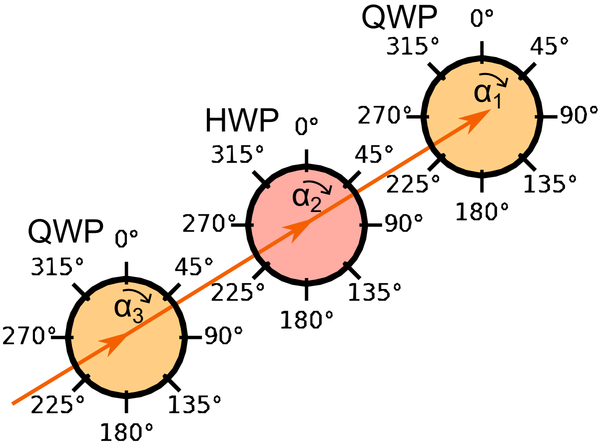

Figure 2.3: Waveplate combination to implement a unitary operation. This figure shows a possible way to implement an arbitrary single-qubit unitary encoded in the polarisation of a photon. The three waveplates shown (QWP, HWP and QWP) implement the operation U_{QHQ} defined in Equation (2.33). The orange arrow shows the propagation direction of the light, and the arrows above the angles α_i indicate the direction in which the waveplates are rotated, such that they correspond to the definitions in Equation (2.33).

If a target unitary U_{target} is given and should be implemented using the combination of QHQ, then the unitary must be decomposed into the unitary matrices of the three waveplates, with variable angles. The following paragraphs outline the algorithm for decomposing a given unitary into the unitaries of the QHQ waveplates combination that is used for the experiments described in this thesis. The Python code used to implement the steps described in the following paragraphs was written by graduated PhD student Vojtěch Krčmarský.

To find the appropriate waveplate angles, the first step is to write down the unitary implemented by the waveplates QHQ as a function of the angles α_1, α_2 and α_3 of the optical axes of the waveplates with respect to the vertical direction[6] (thus $+\pi/2$ is added to the waveplate angles α_i given in Equation (2.30) where the reference is the horizontal and not the vertical plane):

$$\begin{aligned} U_{\text{QHQ}}(\alpha_1,\alpha_2,\alpha_3) &= U_{\text{WP}}(\pi/2,\alpha_1+\pi/2)U_{\text{WP}}(\pi,\alpha_2+\pi/2)U_{\text{WP}}(\pi/2,\alpha_3+\pi/2) \\ &= \frac{1}{2}\begin{pmatrix} U_{11} & U_{12} \\ -\overline{U_{12}} & \overline{U_{11}} \end{pmatrix} \end{aligned} \tag{2.33}$$

with

$$\begin{aligned} U_{11} &= \cos(2(\alpha_1-\alpha_2)) + i\cos(2\alpha_2) + \cos(2(\alpha_2-\alpha_3)) - i\cos(2(\alpha_1-\alpha_2+\alpha_3)) \\ U_{12} &= -\sin(2(\alpha_1-\alpha_2)) + i\sin(2\alpha_2) - \sin(2(\alpha_2-\alpha_3)) - i\sin(2(\alpha_1-\alpha_2+\alpha_3)) \end{aligned} \tag{2.34}$$

and their complex conjugates (denoted by the overhead line).

The second step is to compute the element-wise difference between the matrix describing the combination of waveplates $U_{\text{QHQ}}(\alpha_1,\alpha_2,\alpha_3)$ and the target matrix U_{target}:

$$U_{\text{diff}} = U_{\text{QHQ}}(\alpha_1,\alpha_2,\alpha_3) - U_{\text{target}}. \tag{2.35}$$

The resulting difference matrix U_{diff} contains four complex-valued elements. To enable numerical optimisation using real-valued quantities, the absolute square of each element of U_{diff} is computed, producing four real-valued expressions $|U_{\text{diff}}|^2_{ij}$for $i,j\in\{1,2\}$. Each of these expressions corresponds to an equation that quantifies the mismatch between the two matrices at a particular element.

The third and final step involves using a numerical search that optimises the parameters $\alpha_1,\alpha_2,\alpha_3$ so that the elements $|U_{\text{diff}}|^2_{11}$, $|U_{\text{diff}}|^2_{12}$ and $|U_{\text{diff}}|^2_{22}$ are minimised, i.e., so that $U_{\text{QHQ}}(\alpha_1,\alpha_2,\alpha_3)$ approximates U_{target}. While there are four equations (one for each matrix element), only three of them are used to determine the three waveplate angles. In the experiments presented in this thesis, the programming language Python is used and the function *fsolve* from the *scipy* package *optimize* [50] is used for the

---

[6] The vertical direction is the direction of gravity. The reference is a choice that can be made. From an experimental point of view, the vertical or horizontal directions are useful references for setting up optical elements. In this thesis, the vertical direction is chosen as the reference since the motorised stages are labelled with angles starting from the top, as shown in Figure 2.3. Furthermore, the PBS cubes can be mounted more easily in a parallel or vertical position relative to the breadboard, rather than at an arbitrary angle.

optimisation. The initial guesses for $\alpha_1, \alpha_2, \alpha_3$ used in this thesis for this third and final step are $\alpha_1 = \pi/10\,\mathrm{rad}$, $\alpha_2 = \pi/12\,\mathrm{rad}$ and $\alpha_3 = \pi/8\,\mathrm{rad}$. These initial guesses were previously used in the code of Vojtěch Krčmarský and have been retained here. For some $U_{\mathrm{QHQ}}(\alpha_1, \alpha_2, \alpha_3)$, there may be multiple combinations of the angles $\alpha_1, \alpha_2, \alpha_3$ implementing the same unitary transformation. For example, the identity operation is implemented whenever all the angles are the same: $U_{\mathrm{QHQ}}(\alpha, \alpha, \alpha) = \mathbb{1}$.

2.3. Reconstruction of quantum states and processes

The content of this Section is now described. The reconstruction of a qubit's state from a set of measurements is necessary for comparing it to other states, either states expected from theory or other reconstructed states. The reconstruction of quantum states can be achieved by a technique called "quantum state tomography" [44], presented in Subsection 2.3.1 by means of the example of a two-qubit state. Similarly, a technique to reconstruct processes $\mathcal{E}$ (see Subsection 2.1.2) from a set of measurements is needed for this thesis. The technique is called quantum process tomography and is presented for processes acting on laser light in Subsection 2.3.2. A method to quantify polarisation-dependent loss (PDL), describing the different transmission of differently polarised light in a medium, is presented in Subsection 2.3.4. A measure called fidelity, used to compare states and processes, is presented in Subsection 2.3.3.

2.3.1. Quantum state tomography

To reconstruct a quantum state consisting of a qubit encoded in the energy level of an ion's valence electron and another qubit encoded in the polarisation of a photon, copies of the quantum state have to be measured in different bases. Using the notation $\sigma_{ij} = \sigma_i^{\mathrm{ion}} \otimes \sigma_j^{\mathrm{photon}}$, the ion-photon system can be measured in the nine bases set by the eigenstates of the two-qubit Pauli operators σ_{11}, σ_{12}, σ_{13}, σ_{21}, σ_{22}, σ_{23}, σ_{31}, σ_{32} and σ_{33}. The outcomes of these measurements can be used to obtain the expectation values $\mathrm{tr}(\sigma_{v_1} \otimes \sigma_{v_2}\rho)$, which give an estimate for the density matrix describing the ion-photon state according to Equation (2.10). It is sufficient to measure the ion-photon state in the nine bases listed above to reconstruct the two-qubit state ρ (as in Equation (2.10)), even though the summation in Equation (2.10) involves 16 expectation values. This is because seven of those values involve the identity operation on one qubit, σ_0, and can be extracted from the measurements in the nine bases.

Due to the finite number of experimental repetitions, the statistics are limited, and the density matrix reconstructed in this way may not be physical (discussed in Ref. [44]). To solve this problem, one parametrises a physical density matrix and searches for the parameters that are most likely to produce the measured values of $\mathrm{tr}(\sigma_{v_1} \otimes \sigma_{v_2}\rho)$. This technique is known as maximum likelihood estimation [51].

The procedure used in this thesis to find the most likely physical ion-photon state, an iterative tomographic reconstruction, is written out in Ref. [52, 53]. The code used to obtain the results shown in Chapter 7.2 was developed within the Quantum Optics and Spectroscopy group in Innsbruck. The code takes measurement files of the ion state and the photon state and performs process tomography. Specifically, Equations (1), (4) and (6) in Ref. [52] are implemented in the code and explained briefly in the following sentences. The measurements in this thesis are described by the projectors P_m corresponding to the eigenstates of the two-qubit Pauli operators σ_{ij}. For each σ_{ij}, there are four P_m, one associated with each of the four outcomes of a two-qubit projective measurement. The expectation values given a state ρ are then $p(m) = \mathrm{tr}(P_m\rho)$ according to Equation (2.16). Let $f(m)$ denote the probabilities of obtaining a measurement result m, determined through the measured values (in analogy to the expected probabilities $p(m)$ given a state ρ) for each P_m, and let N denote the number of measured quantum systems not including copies ($N = 2$ for the ion-photon system). A state-dependent operator

$$R(\rho) = \frac{1}{N}\sum_{m=1}^{36}\frac{f(m)}{p(m)}P_m \tag{2.36}$$

is introduced so that the following iterative steps to reconstruct the physical density matrix describing the system can be performed. Equation (2.36) includes the sum over m, which contains $4 \times 9 = 36$ summands (i.e., four P_m for one operator σ_{ij}, and in total there are nine operators σ_{ij}). The iterative steps are now listed.

1. Start with an initial guess $\rho^{(0)}$.

2. Perform one iterative step by updating the previous state $\rho^{(n)}$ to

$$\rho^{(n+1)} = \frac{R(\rho^{(n)})\rho^{(n)}R(\rho^{(n)})}{\mathrm{tr}(R(\rho^{(n)})\rho^{(n)}R(\rho^{(n)}))}. \tag{2.37}$$

3. Repeat the iteration step 2 (Equation (2.37)) and update $\rho^{(n)}$ to $\rho^{(n+1)}$ at each repetition. To get the final reconstructed state in this thesis, iteration step 2 was performed 5000 times, so the final state is $\rho^{(5000)}$.

The division by the trace is performed to maintain the trace of the density matrix ($\mathrm{tr}(\rho^{(n+1)}) = 1$).

2.3.2. Quantum process tomography

There are several ways to describe any kind of quantum processes (unitary as well as non-unitary operations), one of them is the operator-sum representation presented in Equation (2.14). Another way to describe quantum processes is the *Choi matrix representation*, also called Jamiolkowski formalism [54]. A process on a quantum state in the Choi-Jamiolkowski formalism is described in Ref. [54] by the Choi matrix

$$E = \sum_{j,k=0}^{d-1} |j\rangle\langle k| \otimes \mathcal{E}(|j\rangle\langle k|) \tag{2.38}$$

where $d = 2^n$, n is the number of qubits, $\{|j\rangle\}_{j=0}^{d-1}$ is an orthonormal basis for the Hilbert space $\mathcal{H}$ of the qubits, and $\mathcal{E}(\cdot)$ is the map of a matrix subjected to the process (see

Equation (2.14)). An initial quantum state ρ subjected to a process described by E leads to the final state

$$\mathcal{E}(\rho) = \mathrm{tr}_1 \left(E(\rho^{\mathrm{T}} \otimes \mathbb{1}) \right), \tag{2.39}$$

where tr_1 is the partial trace over a part of the Hilbert space of the Choi matrix E such that the final state $\mathcal{E}(\rho)$ is in the same Hilbert space as the initial state ρ.

Quantum process tomography has strong similarities to state tomography; therefore, the algorithm for performing quantum process tomography presented in the following lines has strong resemblances to the algorithm for quantum state tomography presented in Subsection 2.3.1. In Chapter 3.5.2 of Ref. [54], a procedure to obtain the Choi matrix E from experimental data is presented. This procedure is the one adopted in this thesis and is summarised below. To determine the Choi matrix E describing a process acting on a single qubit, different input states ρ_k are prepared and subjected to the process. It is assumed that the process is the same for all the input states. The measurements of the states at the output are described by the projectors P_{kl} describing the l^{th} measurement basis given an input state ρ_k. The probabilities estimated through a measurement are denoted as f_{kl}. The probability to obtain the outcome associated with the projector P_{kl}, for the input state ρ_k is given by (Equation (3.78) in Ref. [54])

$$\begin{aligned} p_{kl}(E) &= \mathrm{tr}(\mathcal{E}(\rho_k) P_{kl}) \\ &= \mathrm{tr}\left(E(\rho_k^{\mathrm{T}} \otimes P_{kl}) \right). \end{aligned} \tag{2.40}$$

Similar to the $R(\rho)$ operator in Equation (2.36) for state tomography, a process-dependent operator for process tomography is defined as

$$R(E) = \sum_{k,l} \frac{f_{kl}}{p_{kl}(E)} \rho_k^{\mathrm{T}} \otimes P_{kl}. \tag{2.41}$$

An iterative tomographic reconstruction is used to force the reconstructed process to be a trace-preserving (i.e., the trace of the state after the process equals the trace of the initial state) and completely positive map. The iterative tomographic reconstruction starts with an initial guess $E^{(0)}$. The n^{th} iteration step of the computation of E is written out as

$$E^{(n+1)} = \frac{R(E^{(n)}) E^{(n)} R(E^{(n)})}{\mathrm{tr}(R(E^{(n)}) E^{(n)} R(E^{(n)}))}. \tag{2.42}$$

A process on a single qubit can be fully determined by twelve real numbers (Chapter 8.4.2 of Ref. [34]). To estimate these twelve real numbers, it is sufficient to prepare four distinct input states, subject them to the quantum process, and measure copies of each resulting output state in the three Pauli bases $\sigma_1, \sigma_2, \sigma_3$.

In the experiments described in this thesis, laser light is used to obtain the process E describing the effect of a fibre on a density matrix ρ. The input states ρ_k are prepared with laser light using a polariser followed by a QWP and a HWP (the waveplates can be in either order), such that any polarisation state can be prepared. The six states

$|H\rangle$, $|V\rangle$, $|D\rangle$, $|A\rangle$, $|R\rangle$ and $|L\rangle$ (even if four of them would be enough) are chosen to be the input states sent through the fibre. For each input state ρ_k, the normalised Stokes parameters s_1, s_2, s_3 of the light at the output of the fibre are measured by a polarimeter. The measured Stokes parameters are converted into the probabilities f_{kl} of measuring the polarisation states $|H\rangle$, $|V\rangle$, $|D\rangle$, $|A\rangle$, $|R\rangle$ or $|L\rangle$ by re-normalisation

$$f_{kl} = \begin{cases} \frac{1}{2} + \frac{s_{i,k}}{2}, & \text{for } l \in \{|H\rangle, |D\rangle, |R\rangle\} \\ \frac{1}{2} - \frac{s_{i,k}}{2}, & \text{for } l \in \{|V\rangle, |A\rangle, |L\rangle\} \end{cases}. \tag{2.43}$$

The matrix $E^{(0)} = \mathbb{1}_4/2$ is used as the initial guess for the Choi matrix. The iteration is set to terminate when the Frobenius norm [55] of the difference between E^n and E^{n+1} falls below a threshold of 10^{-10}, or when a maximum of 3000 iterations is reached.

2.3.3. Fidelity as a distance measure

State fidelity is one way to quantify how close two states are. The fidelity between two density matrices ρ and σ can be calculated according to Ref. [56] by

$$\mathcal{F}(\sigma, \rho) = \left(\mathrm{tr}\sqrt{\sqrt{\sigma}\rho\sqrt{\sigma}} \right)^2 . \tag{2.44}$$

For the case where a state ρ should be compared to an ideal pure state $|\Psi\rangle$, Equation (2.44) reduces to [56]

$$\mathcal{F}(|\Psi\rangle, \rho) = \langle\Psi| \rho |\Psi\rangle . \tag{2.45}$$

When two states are identical, the fidelity is 1. If the fidelity between a two-qubit state and a Bell state is more than 0.5, it proves that the two-qubit state is entangled [57].

As described in Ref. [58], two process matrices can be compared using the fidelity definition of Equation (2.44), by substituting the quantum states with the Choi matrices E_1 and E_2 and calculating $\mathcal{F}(E_1, E_2)$. A fidelity of 1 means that the two processes are identical. Note that this fidelity calculation is only one way of comparing processes, and that in the literature different definitions might be used (e.g., the diamond norm presented in Ref. [59, 60]).

2.3.4. Polarisation-dependent loss

Polarisation-dependent loss (PDL) describes the loss in a medium depending on the polarisation of the light passing through it. PDL is a non-trace-preserving process that cannot be reversed. Due to this non-trace-preserving property, PDL is not described by the reconstructed process presented in the previous Subsection 2.3.2. For example, if the state $|H\rangle$ experiences higher optical loss than $|V\rangle$, sending the diagonal state $|D\rangle$ through the fibre results in an output state biased towards $|V\rangle$. Although PDL cannot be corrected using waveplates, we want to measure it and ensure that it is not the dominant limit in the experiments of Chapter 7 involving photonic polarisation qubits.

PDL can be quantified by performing an experiment in which polarised light is sent through the medium of interest, for example, a fibre, and the power of the light at the output of the fibre is measured. The polarisation of the light is varied over a random set of polarisations. Following Ref. [31], the PDL can be quantified from the results of this experiment by

$$\mathcal{L} = 10\log_{10}\left(\frac{T_{\text{max}}}{T_{\text{min}}}\right) \tag{2.46}$$

where T_{max} is the maximum transmission (ratio of the power of the light at the output to the power at the input of the medium) and T_{min} is the minimum transmission over the random set of input polarisations.

3. Pre-existing quantum network node based on $^{40}\mathrm{Ca}^+$

The results about polarised photons and ion-photon entanglement presented in Chapter 7 make use of three distinct experimental setups. These setups are a cavity-integrated ion trap for $^{40}\mathrm{Ca}^+$ ions, a quantum frequency conversion (QFC) setup, and a photon detection station. Section 3.1 presents key components of the cavity-integrated ion trap setup and discusses established techniques relevant to this thesis, with an emphasis on the generation of single photons from the ion. Section 3.2 describes two QFC setups used to convert the frequency of photons emitted by the $^{40}\mathrm{Ca}^+$ ion to the telecom wavelength.

The ion node and one of the QFC setups (Setup 1) were already available before the start of this master's project, and the other, newer QFC setup (Setup 2) was built by Armin Winkler while I carried out my master's project. Members of the Distributed Quantum Systems group at the University of Innsbruck (DQS) [61] carried out all of the work related to the setups described in this chapter. Details on the ion trap and vacuum chamber assembly can be found in the PhD thesis of Vojtěch Krčmarský [62]. Details on the cavity, the lasers, and the generation of single photons can be found in the PhD thesis of Josef Schupp [63]. Details on the QFC Setup 1 can be found in the PhD thesis of Martin Meraner [64].

3.1. Cavity-integrated ion trap for $^{40}\mathrm{Ca}^+$ and established techniques

The ion trap with an integrated cavity described in the following pages has been used in a number of experiments. For example, the results reported in Ref. [16] show that this cavity-integrated ion trap can serve as a quantum network node. This section begins by presenting the experimental setup, followed by key techniques used in the context of this thesis, with a detailed focus on photon generation via a bichromatic cavity-mediated Raman transition (BCMRT).

3.1.1. Experimental setup

The cavity-integrated ion trap used to take data in this thesis is referred to by our group as *Distributed Quantum Systems 1* (DQS1). The number differentiates it from a second, similar setup (DQS2), the construction of which is currently ongoing.

Vacuum chamber. At the centre of a mu-metal shield, which is an enclosure that suppresses low-frequency magnetic field fluctuations of the environment, there is a vacuum chamber with several flanges and viewports for optical access. A photo of the vacuum chamber is shown in Figure 3.1. The vacuum chamber is made of stainless steel and the pressure inside is below 10^{-9} mbar[62]. The pressure is maintained by a combined ion pump[7], which also contains a non-evaporable getter (NEG) pump, attached to the lower right side of the vacuum chamber (not visible in Figure 3.1). Another NEG pump[8] is

---

[7] NEXTorr D500

[8] CapaciTorr Z400

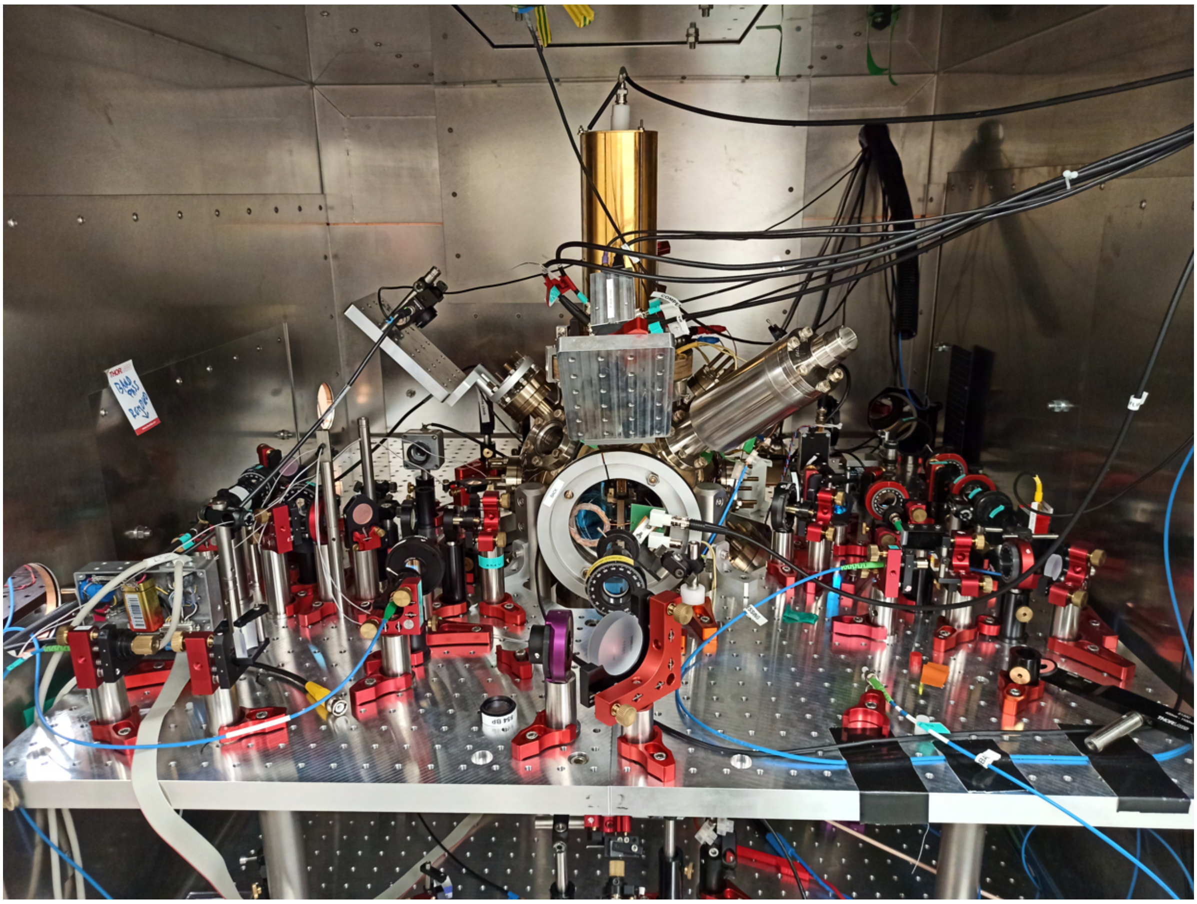

Figure 3.1: A look inside the mu-metal shield. The vacuum chamber is at the centre of the image, with the resonator and the pumps attached. The DQS1 ion trap and the Fabry-Pérot cavity are inside the vacuum chamber. The optical elements on the breadboard around the vacuum chamber allow light to be sent in and out of the chamber. Picture taken on 17.03.2025 in the UIBK laboratory (Viktor-Franz-Hess building, first floor, room 1/33).

attached to the vacuum chamber, but it is currently not in use. A resistively heatable metal tube containing calcium and barium, known as the *atomic oven*, is mounted on the bottom flange of the chamber. The golden cylinder at the top of the vacuum chamber contains a helical resonator, which applies radio-frequency (RF) voltages to the ion trap at a frequency of 23 MHz [62].

Ion trap. The gold-plated electrodes of the ion trap attached to the top flange of the vacuum chamber can be just about seen through the front viewport of the vacuum chamber in Figure 3.1. The trap design is based on previous ion traps in Innsbruck and was manufactured by Stefan Haslwanter at the Institute for Quantum Optics and Quantum Information (IQOQI). The ion trap is a three-dimensional linear Paul trap with four blade electrodes and two endcaps made of gold-coated titanium. The end-cap electrodes are separated by 5.0 mm [62] and have a direct current voltage[9] applied. The four blades are arranged symmetrically around the trap centre, and the distance between two opposing blades is 1.6 mm [62]. The electrodes are mounted on sapphire holders. Additionally, there are three pairs of electrodes, known as compensation electrodes, used to compensate stray electric fields and centre the ions in the trap [63]. Outside the vacuum chamber are rings of permanent magnets, which create a magnetic field of 4.22 Gauss at the centre of the trap [62]. Figure 3.2 shows the direction of the magnetic field at the position of the trapped ions. The magnetic field splits the atomic energy levels into Zeeman sublevels. If several ions are trapped with appropriate trap frequencies, the ions form a string. The ion string axis is defined by the axis of the endcap electrodes, which is vertical.

Fabry-Pérot cavity. Two mirrors are placed on the right and left sides of the ion trap (as shown in Figure 3.2a). These mirrors form a macroscopic, near-concentric Fabry-Pérot cavity. A lens is placed on each side of the cavity to collimate the cavity output mode and mode-match incoming laser light. The cavity was built by graduated PhD student Josef Schupp, and the characterisation results are shown in his PhD thesis [63], from which the following cavity parameters (characterised with 854 nm light) are taken. When they were first put in vacuum, the transmissions of the two mirrors were 2.9(4) ppm for the highly reflective mirror and 90(4) ppm for the other mirror (called the *output mirror*), respectively. The distance between the mirrors is 19.9057(5) mm, the free spectral range is 7.5303(2) GHz, and the radius of curvature of the mirrors is 9.9841(7) mm. The waist of the TEM$_{00}$ mode of 854 nm light at the centre of the cavity is $\omega_o = 12.31(8)\,\mu\text{m}$. The maximum ion-cavity coupling strength is $g_0/(2\pi) = 1.53(1)\,\text{MHz}$ and the cavity decay rate is $\kappa/(2\pi) = 70(2)\,\text{kHz}$. The cavity finesse was determined to be $54(1) \times 10^3$. However, following a laboratory accident in 2022, the finesse was reduced to $30(1) \times 10^3$ and the cavity decay rate increased to $\kappa/(2\pi) = 126(2)\,\text{kHz}$ [65]. The probability of a photon inside the Fabry-Pérot cavity exiting into the desired free-space output mode is now given by 0.43(3) [65].

Optics, lasers and detectors. Multiple laser paths are directed toward the centre of the ion trap, facilitated by the positioning of the vacuum chamber centred on one breadboard and elevated above a second breadboard, as shown in Figure 3.1. Various optical components (such as mirrors, waveplates, and fibre collimators) are mounted on these breadboards to direct laser beams through different viewports into the vacuum chamber. The lasers employed in the setup are listed in Table 3.1. Most of these lasers drive atomic transitions (discussed in Sections 3.1.2 and 3.1.3), and their propagation directions are illustrated in Figure 3.2. The 375 nm and 422 nm lasers ionise neutral ^{40}Ca atoms originating from the atomic oven located beneath the ion trap. An 806 nm laser is used for cavity length stabilisation. The lasers at 393 nm and 806 nm are frequency stabilised by locking to an external reference cavity positioned on the same optical table as the mu-metal shield [66, 67]. An objective with a numerical aperture of 0.289 [63] is positioned near an inverted viewport at the rear of the vacuum chamber to image the ions and read out their electronic state. The objective enables 397 nm

---

[9] ISEG box: EHS 82 20x-F

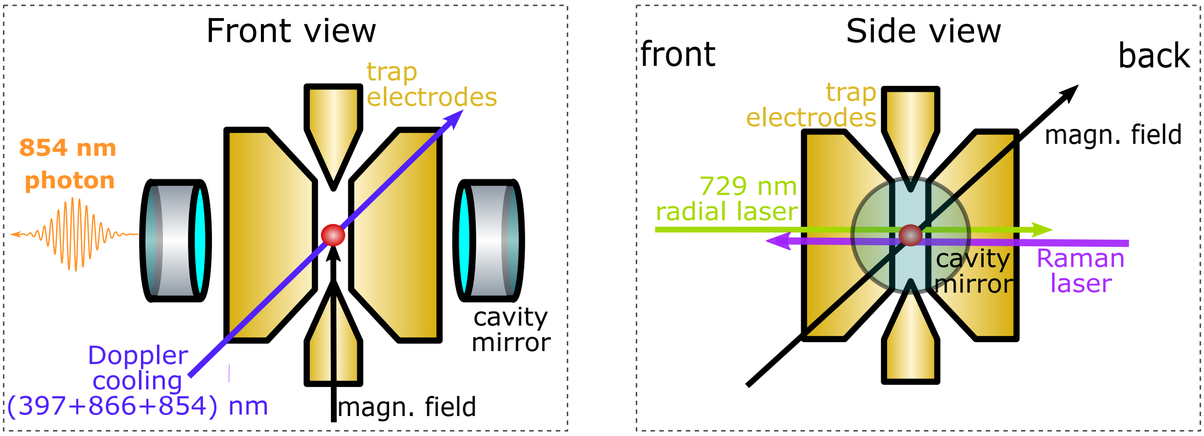

(a) Front view (same view as Figure 3.1). **(b)** View from the right side of Figure 3.2a.

Figure 3.2: Cavity-integrated ion trap and relevant laser geometry. The two drawings (a) and (b) show the ion trap system from two different perspectives, illustrating the directions of the lasers with respect to the cavity axis (i.e., the line connecting the two cavity mirrors) and the magnetic field vector. The drawings of the ion trap and the cavity are adapted from Figure 3.3 in Martin Meraner's PhD thesis [64], with additional elements added by the author. The laser directions relevant for the experiments presented in this thesis are overlaid on the schematic.

fluorescence detection while simultaneously focusing the 393 nm Raman laser beam onto the ions. The collected fluorescence is directed to an electron-multiplying charge-coupled device (EMCCD) camera[10] and a photo-multiplier tube (PMT). The photons that exit the Fabry-Pérot cavity are coupled into a single-mode fibre[11]. The fibre's output can be connected either to a fibre that sends photons to a superconducting nanowire single photon detector (SNSPD)[12], or to a fibre that goes to a QFC setup. A device called time-tagger[13] is used to record the time of electrical signals (for example, signals from the SNSPDs).

Electronics for experimental control. Electronic devices are used to control the ion trap system and the lasers [63]. These devices interface with three PCs, which are connected via Ethernet within the same local area network (LAN). One PC controls the trap voltages and the EMCCD camera; a second PC monitors the laser wavelengths through a wavemeter; and a third PC is connected to an electronic control system that

---

[10] Andor iXon Ultra 897

[11] Thorlabs 780HP-Custom-Muc, 5.0 µm, 0.13 NA, M00488488, 20 m length.

[12] Scontel FCOPRS-CCR-2TW75+2SW85. Photons at 854 nm or 1550 nm can be detected. The SNSPD efficiency of low-noise detectors at 1550 nm is about 75 % and the bandwidth at full width at half maximum (FWHM) is 20 nm according to Ref. [68]. The SNSPD efficiency at 850 nm is about 85 % and the bandwidth at FWHM is 50 nm according to Ref. [68]. For the two 854 nm detectors used to obtain some of the results of Chapter 7.2, maximum efficiencies of 86 % (at 24 µA bias current) for detector channel 1 and 88 % (at 25 µA bias current) for detector channel 2 were given on the specification sheet provided by the company.

[13] Swabian Time Tagger 20

Table 3.1: Lasers used for various wavelengths with corresponding model information. Which laser can drive which atomic transition is shown in Figure 3.3.

Wavelength (nm)	Laser Model	Purpose
375	Toptica iBeam smart	Photo-ionisation
422	Toptica DL-Pro	Photo-ionisation
806	Toptica DL-Pro	Cavity stabilisation
393	M^2 SolsTiS 1600 PSX-R Ti:Sa with ECD-X frequency doubling module	Raman transition
397	Toptica TA-SHG Pro	Doppler cooling, optical pumping, atomic fluorescence
729	Toptica DL-Pro[14]	Optical qubit transition
854	Toptica DL-Pro	Repumping from $3^2D_{5/2}$
866	Toptica DL-Pro	Repumping from $3^2D_{3/2}$

enables the execution of experimental sequences and the control of the generation of laser pulses (each controlled by an acousto-optic modulator (AOM)). The electronic control system is a field-programmable gate array (FPGA)-based pulse sequencer referred to as the *pulse box* [69], which was developed in-house within the Quantum Optics and Spectroscopy group over many years. The FPGA-based pulse box controls transistor-transistor logic (TTL) outputs and also triggers radio-frequency (RF) pulses used to drive AOMs in the 729 nm and 393 nm laser paths, as well as an acousto-optic deflector (AOD) used to steer the 393 nm beam. The TTL signals from the pulse box control RF switches that gate RF signals generated by external direct digital synthesisers, which provide drive signals for other AOMs. The frequencies and powers of these external synthesisers are configured via software from the third PC.

3.1.2. Key established techniques

The cavity-integrated ion trap is used to take the data in Chapter 7; however, I did not operate the cavity-integrated ion trap myself. Therefore, the following descriptions are only summaries of the established techniques used in the lab. No quantitative analysis is presented, and only the techniques relevant to this thesis are introduced. Details about the established techniques can be found, for example, in Chapter 5 of Ref. [63].

To encode a qubit in the electronic state of a ^{40}Ca$^+$ ion, two electronic energy levels can be selected. The fine-structure manifold of the ion is denoted by the notation $n^{2s+1}L_J$, where n is the principal quantum number, s is the spin, L is the orbital angular momentum, and J is the total angular momentum quantum number. An external

---

[14] The 729 nm laser used on 20.12.2024 is placed in the laboratory of the *2D Crystals* group [70] on the first floor of the Viktor-Franz-Hess Haus at Technikerstraße 25, Innsbruck.

magnetic field further splits the fine-structure levels into Zeeman sublevels, labelled by the quantum number m_j. We define the qubit states as $|0\rangle = |4^2\mathrm{S}_{1/2}, m_j = -1/2\rangle$ and $|1\rangle = |3^2\mathrm{D}_{5/2}, m_j = -3/2\rangle$. Figure 3.3 shows relevant energy levels and transition wavelengths of $^{40}\mathrm{Ca}^{+}$. The energy levels in the fine-structure corresponding to the two states $|0\rangle$ and $|1\rangle$ are shown in Figure 3.3, together with neighbouring energy levels that are relevant for this thesis. The metastable $3^2\mathrm{D}_{5/2}$ manifold of states has a lifetime of 1.17 seconds [71], which is much longer than the timescales needed for the experiments presented in this thesis.

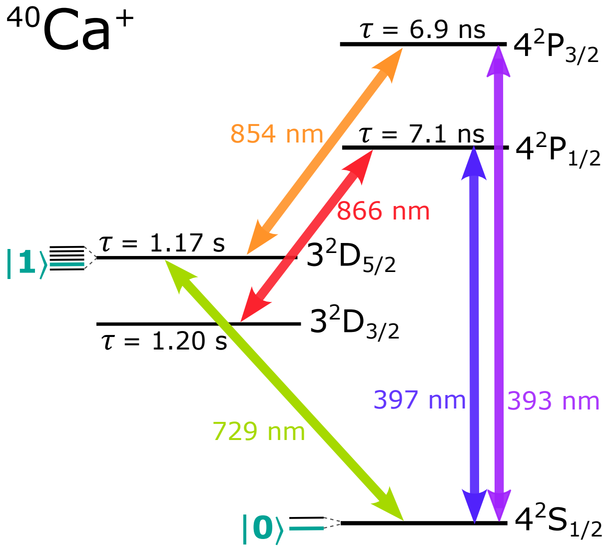

Figure 3.3: Reduced energy level scheme of the $^{40}\mathrm{Ca}^{+}$ ion and laser wavelengths. The lifetimes of the energy levels of the excited state manifolds, written as τ, are shown next to the respective levels. On the left side of the $4^2\mathrm{S}_{1/2}$ and $3^2\mathrm{D}_{5/2}$ energy levels, the Zeeman structure is shown, and the chosen energy levels used to encode the qubit ($|0\rangle$ and $|1\rangle$) are highlighted in turquoise. Laser light at the shown wavelengths is available in the Lanyon lab. The transition wavelengths are taken from Ref. [72], the lifetimes τ of the P states are from Ref. [73], and the lifetimes τ of the D states are from Ref. [71].

The following paragraphs briefly summarise key techniques, developed over the past decades, for working with $^{40}\mathrm{Ca}^{+}$ ions and employed in the experiments presented in this thesis.

Trap. Several preparation steps are performed in order to successfully load and trap an ion. First of all, voltages are applied to the trap blades and endcaps to create a dynamic quadrupole electric field, which enables ions to be trapped in all three spatial directions. Direct current voltages are applied to the endcaps of the trap and to two opposing blades. The other two opposing blades are subjected to an alternating current voltage that oscillates at RF. Secondly, the atomic oven is resistively heated, releasing neutral calcium atoms that escape through an opening at the top of the metal tube. The atomic beam is then collimated and directed through two apertures (one in the oven shield and another in the trap's sapphire cap) before reaching the centre of the trap. The neutral calcium atoms can be ionised by laser beams (with wavelengths of 422 nm and 375 nm) at the centre of the trap. The calcium ions can then be trapped [16, 63].

Initialise. Once the ion has been trapped, its motional and electronic states are prepared to initialise the qubit in the state $4^2\mathrm{S}_{1/2}, m_j = -1/2$. Specifically, the ion's motion is Doppler cooled [74] by lasers at 397 nm (π polarised, approximately -10 MHz detuned from the $4^2\mathrm{S}_{1/2} \rightarrow 4^2\mathrm{P}_{1/2}$ transition) and 866 nm. Additionally, an 854 nm laser is used to repump the $3^2\mathrm{D}_{5/2}$ manifold while Doppler cooling. The lasers are directed at the ion as shown in Figure 3.2b. The Doppler cooling beams are aligned at a 45° angle relative to the axis along the endcap electrodes of the Paul trap, such that the beams overlap with all three motional directions of the trapped ion. The electronic state is then prepared via optical pumping with a 397 nm, σ^- polarised beam[15]. The 397 nm σ^- polarised beam transfers the ion's electronic state from the $4^2\mathrm{S}_{1/2}, m_j = +1/2$ state to the $4^2\mathrm{S}_{1/2}, m_j = -1/2$ state. While the 397 nm σ^- is illuminating the ion, the 854 nm and 866 nm lasers are also switched on to depopulate the $3^2\mathrm{D}_{5/2}$ and $3^2\mathrm{D}_{3/2}$ manifolds.

Manipulate. Once the qubit has been initialised in the $|0\rangle = |4^2\mathrm{S}_{1/2}, m_j = -1/2\rangle$ state, operations on the optical quadrupole transition to the $3^2\mathrm{D}_{5/2}$ manifold of states can be driven by the 729 nm laser. The operations used in the experiments presented in this thesis are implemented using π and $\pi/2$ pulses of the 729 nm laser (see supplemental material of Ref. [16]). A π pulse implements a logical qubit flip, bringing the state $|0\rangle$ to $|1\rangle$ and vice versa. A $\pi/2$ pulse can bring the state $|0\rangle$ into the superposition state $(|0\rangle + \mathrm{e}^{i\theta}|1\rangle)/\sqrt{2}$, with a phase θ controlled by the phase of the laser field at the point of the ion. Whether a laser pulse is a π or $\pi/2$ pulse is determined by its duration and intensity. In addition to operations on the quadrupole transition, 393 nm laser pulses can be applied to the ion to generate single photons. Details of the method used to generate photons are provided in Subsection 3.1.3.

Readout. The logical state of the qubit encoded in the electronic state of the ^{40}Ca^{+} ion is read out via a fluorescence measurement (see Chapters 3.4.2 and 5.3 of Ref. [63] for more details). Laser beams at 397 nm and 866 nm are directed onto the ion. If the ion is in the $4^2\mathrm{S}_{1/2}$ manifold, it is excited to the $4^2\mathrm{P}_{1/2}$ manifold and most likely decays back to the $4^2\mathrm{S}_{1/2}$ manifold by emitting a 397 nm photon in a random direction. If the electron decays to the $3^2\mathrm{D}_{3/2}$ manifold, it is re-excited into the $4^2\mathrm{P}_{1/2}$ manifold by the 866 nm laser, such that the process driven by the 397 nm laser can be repeated and multiple photons are emitted. Some of the emitted 397 nm photons (called fluorescence photons) are collected by the objective and detected by the PMT[16]. If fluorescence photons are detected by the PMT, the ion is considered "bright". If instead the ion is in the $3^2\mathrm{D}_{5/2}$ manifold, it is not excited by the 397 nm beam and no fluorescence photons are detected

---

[15] A $\sigma^{\pm}$ polarised beam is a circularly polarised beam travelling along the quantisation axis defined by the external magnetic field vector and can drive transitions with $\Delta m_j = \pm 1$. For example, if the beam is left-hand circularly polarised and parallel to the quantisation axis, then it is σ^- polarised. If the beam is π polarised and does not propagate parallel to the magnetic field vector, then a transition with $\Delta m_j = 0$ is driven. These statements refer to the case in which an electric dipole transition is driven.

[16] In the experiments of this thesis, only the PMT is used to detect the ion state (the camera is not used for this purpose).

by the PMT. In this case, the ion is considered “dark”. The bright and dark states are differentiated by setting a threshold for the photon counts recorded in a fixed amount of time on the PMT. The effective measurement basis of such a projective measurement can be altered by performing operations on the qubit with the 729 nm laser before the measurement. The role of the 729 nm laser pulses is similar to the role of the waveplates in front of the PBS for photon measurements, as described in Subsection 2.2.2.

3.1.3. Photon generation via a cavity-mediated Raman transition

The deterministic generation of a single photon from an atom in a cavity using a monochromatic cavity-mediated Raman transition (CMRT) was theoretically proposed in 1997 [75]. An early experimental realisation of the bichromatic cavity-mediated Raman transition for tunable ion-photon entanglement was reported in 2012 [76]. In this thesis, the monochromatic CMRT is used to obtain the results presented in Section 7.1, while the bichromatic cavity-mediated Raman transition is used to obtain the results presented in Section 7.2.

The BCMRT enables the production of a single photon whose polarisation is entangled with the electronic state of the ion. In the following, a step-by-step description of the process used to perform the BCMRT in the experiments presented in this thesis is given, based on Ref. [76].

1. The ion is prepared in the electronic state $|0\rangle = |4^2\mathrm{S}_{1/2}, m_j = -1/2\rangle$ using optical pumping, and its motional state is prepared by Doppler cooling. Using methods described in Ref. [63], the ion is positioned at an antinode of the vacuum standing-wave cavity field at the centre of the Fabry-Pérot cavity. At this stage, there are no 854 nm photons in the cavity.

2. A 393 nm laser (σ^- polarised) is used to drive a $\Delta m_j = -1$ transition from the state $|0\rangle = |4^2\mathrm{S}_{1/2}, m_j = -1/2\rangle$ to $|4^2\mathrm{P}_{3/2}, m_j = -3/2\rangle$. The laser is bichromatic, meaning that there are two tones with frequencies f_1 and f_2, with a frequency difference of $\delta_\mathrm{Z} = f_2 - f_1$, as shown in Figure 3.4. The typical detunings of the two 393 nm tones from the $4^2\mathrm{S}_{1/2}$ to $4^2\mathrm{P}_{3/2}$ transition are $\Delta_1 = 377(5)$ MHz (supplementary material of Ref. [24]) and $\Delta_2 = \Delta_1 + \delta_\mathrm{Z} = 384(5)$ MHz, with $\delta_\mathrm{Z} = 6.957$ MHz set in the experiment presented in Section 7.2. The difference δ_Z should correspond to the Zeeman splitting of the two states $|e_1\rangle = |3^2\mathrm{D}_{5/2}, m_j = -5/2\rangle$ and $|e_2\rangle = |3^2\mathrm{D}_{5/2}, m_j = -3/2\rangle = |1\rangle$ caused by the static magnetic field. The Zeeman splitting δ_Z of $|e_1\rangle$ and $|e_2\rangle$ is $2\pi \times 6.97$ MHz [77] for a magnetic field of 4 Gauss. The Raman resonance condition means that the frequency difference between each individual tone in the 393 nm laser field and the cavity resonance frequency matches the frequency of the relevant $|0\rangle \leftrightarrow |e_{1,2}\rangle$ transition. If the Raman resonance condition is fulfilled, then ideally the state $|0\rangle = |4^2\mathrm{S}_{1/2}, m_j = -1/2\rangle$ is coherently transferred to either $|e_1\rangle$ or $|e_2\rangle$ of the $3^2\mathrm{D}_{5/2}$ manifold, and a single photon that is polarisation-entangled with the electronic state of the ion is emitted into the cavity. The two Raman processes lead to a single photon but with different polarisations. If the electron ends up in the state $|e_1\rangle$, then the photon is σ^- polarised with

respect to the quantisation axis. If the electron ends up in the state $|e_2\rangle$, then the photon is π polarised with respect to the quantisation axis. The polarisation of the photon depends on the direction of collection (cavity axis) with respect to the magnetic field.

3. The photon leaves the cavity through the output mirror into free space.

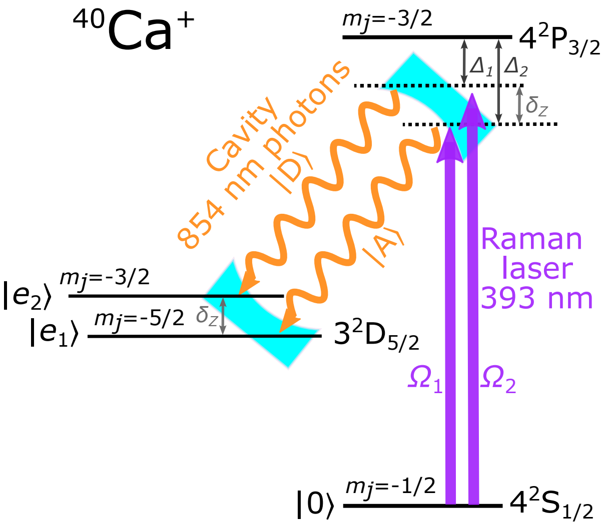

Figure 3.4: Relevant energy levels of the ^{40}Ca^{+} ion for the bichromatic cavity-mediated Raman process. The polarisation of the photon denoted as $|D\rangle$ ($|A\rangle$) is parallel (perpendicular) to the magnetic field direction (see Figure 3.2). $|e_1\rangle$ and $|e_2\rangle$ are the electronic states of the ion.

The DQS1 setup features a 45° angle between the 393 nm Raman laser and the magnetic field (see Figure 3.2b). The 393 nm Raman laser beam is horizontally polarised, with its electric field oscillating perpendicular to the direction of the magnetic field to avoid driving a $\Delta m_j = 0$ transition. In the specific configuration of the DQS1 setup, when photons are collected along the cavity axis, the σ^- and π polarisations are projected onto the antidiagonal (denoted by $|A\rangle$) and diagonal (denoted by $|D\rangle$) polarisations, respectively (see Ref. [78]). The power of the 393 nm Raman laser and the relative phase of the two tones f_i are set to ideally produce the Bell state

$$|\Psi\rangle_{\text{ion,photon}} = \frac{1}{\sqrt{2}} \left(|e_1\rangle \, |\text{A}\rangle + |e_2\rangle \, |\text{D}\rangle \right). \tag{3.1}$$

Furthermore, the photons leaving the cavity and the vacuum chamber are coupled into a single-mode fibre, which can be used to guide the photons to other setups such as a QFC setup or a polarisation analysis setup.

The generation of single photons via the monochromatic CMRT is analogous to the generation of ion-entangled photons via the BCMRT, except that only one tone of the 393 nm Raman laser is used. The consequence of using only one tone is that the generated photon has a certain polarisation ($|D\rangle$ or $|A\rangle$, depending on which Raman transition is driven) and is not entangled with the ion.

3.2. Quantum frequency conversion

As described in Chapter 1 of this thesis, QFC is employed to convert photons emitted by the ion, which are at a wavelength of 854 nm, to the telecom wavelength at 1550 nm (telecom C band). The transmission loss of the telecom wavelength in a SMF-28 Ultra optical fibre can reach as low as 0.173 dB/km[17], while the transmission loss of photons at 854 nm is as low as 3 dB/km [79]. Therefore, the distance over which 1550 nm photons can be transmitted through optical fibre with the same efficiency as 854 nm photons is significantly increased.

This thesis reports experiments done with two different QFC setups. The results presented in Chapter 7.1 are obtained using Setup 1, which is the "old" conversion setup described in Ref. [64]. The experiments presented in Chapter 7.2 are obtained using Setup 2, which is the "new" conversion setup, built in early 2024. Before describing the two QFC setups, a summary of the physical principle behind QFC is given in the following paragraph.

The method used to convert the frequency of photons in the two QFC setups presented in this section is difference frequency generation (DFG). To perform DFG, a photon with a frequency of ω_{in} and an additional laser, called the *pump laser*, with a frequency ω_{pump} are sent through a crystal with a second-order nonlinearity. The crystal, characterised by its second-order nonlinear susceptibility [80], can convert the frequency of a photon because it has a nonlinear response to an external electric field, which enables the mixing of frequencies (sum/difference frequency generation). Ideally, the photon coming out from the crystal has a frequency of $\omega_{\text{out}} = \omega_{\text{in}} - \omega_{\text{pump}}$.

To convert an 854 nm photon emitted by the $^{40}\text{Ca}^{+}$ ion to 1550 nm via DFG, a pump laser with a wavelength of 1902 nm is used [64]. The DFG process must satisfy energy and momentum conservation. To satisfy momentum conservation, the phase velocity difference between the 1902 nm, 854 nm and 1550 nm light should be compensated, which is achieved by periodically poling the crystal. The second-order nonlinear crystals used for QFC in the experiments presented in this thesis are periodically poled lithium niobate (PPLN) ridged waveguides made by an external company.

DFG is not the only process occurring in the crystal: there are also noise processes such as anti-Stokes Raman scattering, where photons from the pump are converted to the telecom wavelength (through interactions with phonons in the crystal, which provide the energy). Filters are used to remove the pump light and partially suppress the noise photons after the nonlinear crystal. Details about the used filters follow in the sections dedicated to the individual setups.

3.2.1. Setup 1

Setup 1 existed before the start of my master's project and was built by Martin Meraner and Viktor Krutianskii. Details of the setup, including make and model numbers as well as its characterisation, can be found in Ref. [64].

---

[17] The value of 0.173 dB/km is specified on a 50 km fibre spool available in the Lanyon lab.

The single-mode fibre guiding 854 nm photons emitted by the ion is joined[18] to a fibre leading to a first fibre collimator in QFC Setup 1. The photon path is then combined with the 1902 nm pump light path via a dichroic mirror. The two wavelengths are focused with an aspheric lens[19] and sent through a temperature-stabilised PPLN crystal[20], which converts the vertical component of the polarisation. The polarisation of the 1902 nm and 854 nm wavelengths is then rotated by 90° in real space using a half-waveplate (HWP)[21], such that the 854 nm polarisation component $|H\rangle$, which is not converted by the first crystal, is mapped to $|V\rangle$ and converted by a second PPLN crystal. Another aspheric lens[22] is placed at the output of the second PPLN crystal. Finally, several filters are used to remove almost all wavelengths deviating from the 1550 nm wavelength of the photons: a 1600 nm short-pass filter[23], a volume Bragg grating[24], and an air-spaced Fabry-Pérot cavity (called etalon, not temperature stabilised)[25]. The narrowest filter stage has a bandwidth of 0.002 nm (250 MHz).

As described in Ref. [79], QFC Setup 1 achieved a total photon-in to fibre-coupled photon-out efficiency of 0.30 with a fibre-coupled photon noise rate of 58(4) s^{-1}. The noise photons include all telecom photons introduced by the anti-Stokes scattering of the pump laser field. A fidelity of 0.93(1) relative to the identity process was obtained for the reconstructed process performed on the converted photon's polarisation.

3.2.2. Setup 2

Setup 2 was built by Armin Winkler with support from Žiga Pušavec in early 2024 and will be described in detail in Armin Winkler's upcoming PhD thesis. While the goal of polarisation-preserving QFC remains the same, Setup 2 differs from Setup 1 in several key aspects. Firstly, Setup 2 uses only one PPLN crystal instead of two. To efficiently convert both polarisation components while preserving the photon polarisation, Setup 2 employs a Sagnac interferometer configuration. A schematic of a QFC setup in Sagnac configuration is shown in Fig. 4 of Ref. [81]. Unlike Setup 1, Setup 2 includes a dichroic mirror in the output path from the Sagnac loop. Since this dichroic mirror reflects only wavelengths around 1550 nm, the short-pass filter used in Setup 1 to separate the 1902 nm pump light from the converted photons is no longer necessary. Additionally, the etalon[26] in Setup 2 is actively temperature stabilised using a digital temperature

---

[18] The use of a fibre joiner allows for switching between the two QFC setups without disturbing the alignment of the setups.

[19] Thorlabs A220TM. The focal length is 11 mm.

[20] Manufactured by NTT Electronics. The PPLN ridged waveguides, to which the light is coupled, are fabricated on a lithium tantalate substrate.

[21] The Fresnel Rhomb mentioned in Ref. [64] was replaced by a HWP at the end of 2023/beginning of 2024 by Armin Winkler.

[22] Thorlabs C220TMD. The focal length is 11 mm. The surface is anti-reflection coated.

[23] Edmund Optics 84-656, OD5 at 1902 nm

[24] OptiGrate. The reflection of 1550 nm light is 95 % and the bandwidth is 0.2 nm (25 GHz) [64].

[25] SLS Optics. The linewidth is 250 MHz (corresponding to 0.002 nm), the free spectral range is 12.5 GHz, and the peak transmission at 1550 nm is 95 % [64].

[26] LightMachinery OP-7423-3371-4. Fused Silica, 1450 nm to 1700 nm, finesse >30, FSR $= 1\,\mathrm{cm}^{-1} \approx 30\,\mathrm{GHz}$, thickness 3.371 mm, 0.6 GHz bandwidth (calculated using [82]).

controller developed at the University of Innsbruck.

In March and April 2024, Armin Winkler measured a fibre-coupled photon noise rate of $32(3)\,\mathrm{s}^{-1}$ in the output of Setup 2, using an input pump power of 900 mW. For lower pump powers, such as the 500 mW used in the experiments described in Chapter 7.2, the fibre-coupled noise photon rate is expected to decrease linearly. The efficiency of the setup, measured on the day of the experiment, is given in Section 7.2.

4. Off-campus fibre network, photon detection station and polarisation drift compensation setup

This chapter introduces the final setup used to obtain the results presented in Chapter 7. The previously introduced $^{40}\mathrm{Ca}^{+}$ quantum network node and the quantum frequency conversion (QFC) setups (see Chapter 3) are components of this setup. Parts of the setup are also used to obtain the results in Chapter 6 and parts of Chapter 5. Section 4.1 presents an overview of the setup used to obtain the results presented in Chapter 7. Section 4.2 presents the details about the 17 km-long optical fibres deployed across Innsbruck. Section 4.3 presents the Mutters photon detection station. Section 4.4 presents the polarisation drift compensation setup.

4.1. Overview

The setup used to obtain the results presented in Chapter 7 is split into two parts: one part is in the Lanyon lab on the Technik campus (Technikerstraße 25, first floor), and the other part is at the photon detection station in Mutters (Gewerbepark Mutters-Gärberbach 7, first floor). The $^{40}\mathrm{Ca}^{+}$ ion node and the QFC setups are located in the Lanyon lab. The Mutters photon detection station comprises a polarisation analysis board and superconducting nanowire single photon detector (SNSPD)s, which are housed in separate racks. The photon detection station is explained in detail in Section 4.3. The two locations are connected by two 17 km-long single-mode fibre paths (Section 4.2): one dedicated to sending photons (off-campus fibre path 2) and the other for classical communication (off-campus fibre path 1). Figure 4.1 shows an overview of the entire setup used to implement the most advanced experiments in this thesis that are reported in Chapter 7.2: entanglement between an ion and a remotely-detected photon. The parts of Figure 4.1 that have a pink background belong to the setup used to characterise and compensate for changes in polarisation of light induced by off-campus fibre path 2. These components form the polarisation drift compensation setup, which is the focus of my master's thesis and is explained in detail in Section 4.4.

The setup in Figure 4.1 is used in Chapter 7 of this thesis as follows. The 854 nm photons emitted by the ion and leaving the Fabry-Pérot cavity are coupled into a single-mode fibre, which guides them to a different optical table where the QFC setups (Section 3.2) are located. The fibre can be connected with a fibre joiner to the input fibre of either QFC setup. After the QFC, the 1550 nm photons are coupled with a fibre collimator once again into a single-mode fibre and sent through off-campus fibre path 2 to Mutters. At the Mutters photon detection station, an optical bandpass filter (specifically, a fibre Bragg grating (FBG)) reduces the amount of noise and background photons present at the end of the off-campus fibre path 2. The photons are then out-coupled with a fibre collimator into free space. Polarisation analysis of the photons emitted by the ion is performed using a half-waveplate (HWP), a quarter-waveplate (QWP), and a polarising beam splitter (PBS) cube, as described in Subsection 2.2.2. Each output path of the PBS cube passes through another bandpass filter and is coupled into a

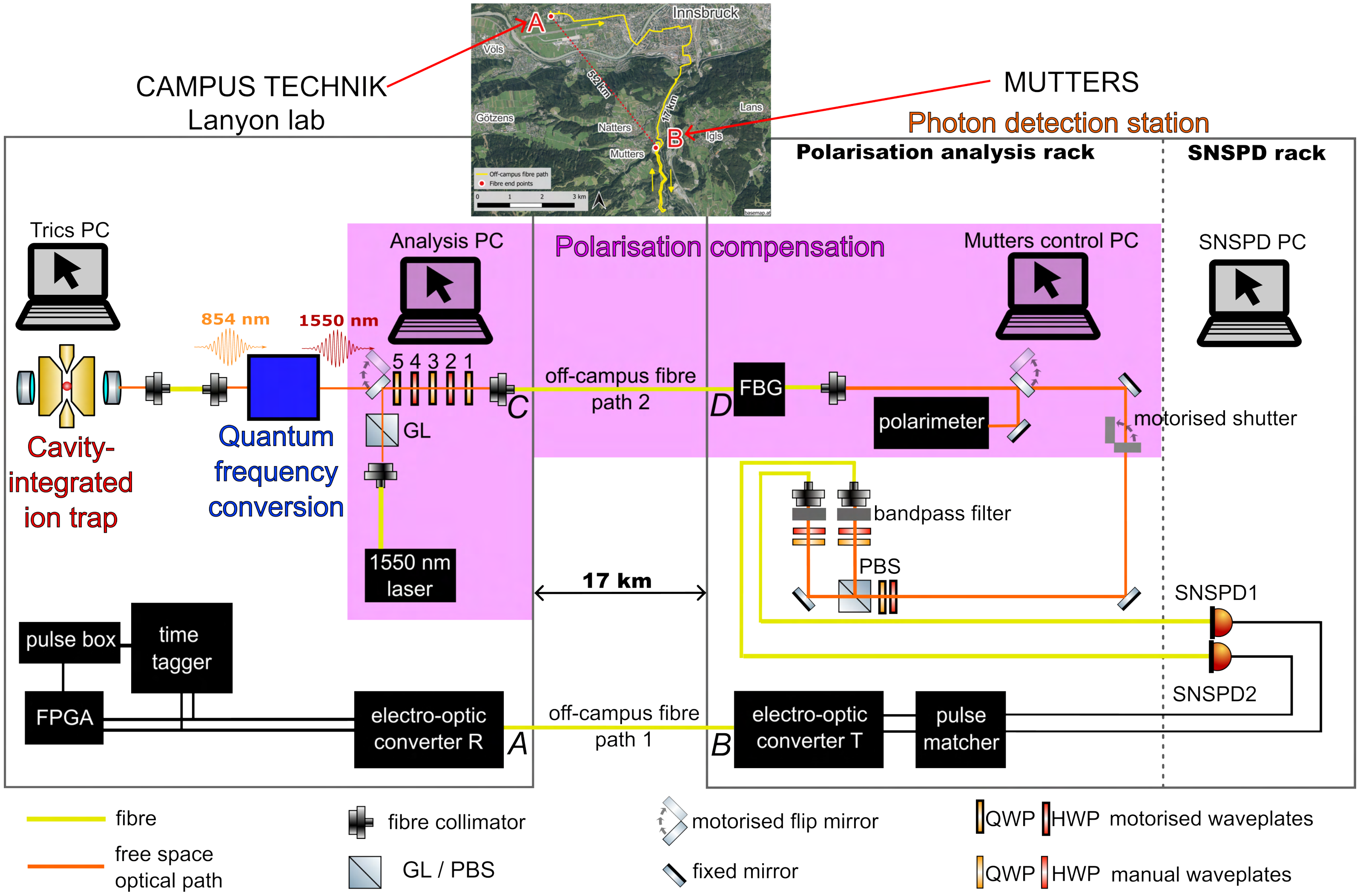

Figure 4.1: Experimental setup for the experiments with single photons reported in Chapter 7. The photon detection station is divided by a dotted line into two parts, representing the two racks: the polarisation analysis rack and the SNSPD rack. The cavity-integrated ion trap and the QFC setup (Setup 1 for the experiment in Section 7.1 and Setup 2 for the experiment in Section 7.2), both located in the Lanyon lab on the Technik campus (Technikerstraße 25, first floor), are explained in Chapter 3. More details on the polarisation drift compensation setup, including all associated electronics, are shown in Figure 4.2. The make and model numbers of the devices are provided in the footnotes of the main text. FBG – fibre Bragg grating; FPGA – field-programmable gate array; PBS – polarising beam splitter; T – transmitter; R – receiver.

fibre, which directs the photons to a SNSPD channel (one for each output path). The signals from the detectors are sent back to the Lanyon lab via electro-optic converters: real-time electronic transistor-transistor logic (TTL) outputs of the SNSPDs in Mutters are encoded into optical signals which are converted back to electronic signals in the Lanyon lab. In the Lanyon lab, the signals are time-tagged. The motorised flip mirror of the polarisation drift compensation setup in the Lanyon lab is used to direct 1550 nm laser light through off-campus fibre path 2 instead of the photons emitted by the ion. A Glan-laser polariser (GL) and waveplates in the Lanyon lab are used to prepare the laser light in different polarisation states. The other motorised flip mirror in Mutters enables sending the light to a polarimeter instead of the SNSPDs. The outcomes of the measurements with laser light are used to compensate for the polarisation changes induced by the off-campus fibre path 2. Alternating between sending photons to Mutters and performing polarisation drift compensation runs allows the polarisation drift to be monitored and compensated at regular intervals.

4.2. Fibre network

The path taken by the off-campus fibres can be divided into three sections. All fibres involved are single-mode, non-polarisation-maintaining and for telecom wavelength (1550 nm).

1. **Lanyon lab to Zentraler Informatik Dienst at the University of Innsbruck (ZID)**. Starting from the Lanyon lab, the fibre path goes from the Viktor-Franz-Hess-Haus to a room belonging to the ZID (the room is on the ground floor of Technikerstraße 23) by passing through the semi-underground car park[27]. There are twelve fibres in this section, forming a fibre bundle. The individual fibres in the Lanyon lab are bundled through a fibre fan-out box. For the experiments presented in this thesis, the fibres with the labels 1 and 3 are used. The fibres in this section were characterised in August 2023 by the company Obrist. The characterisation was performed with a method called optical time domain reflectometer (OTDR)[28]. The OTDR measurements[29] show that the fibres in this section are 261.8 m long and that fibre 1 has a loss of 0.419 dB at 1550 nm while fibre 3 has a loss of 0.423 dB.

2. **ZID to Mutters basement**. From the ZID room onwards, the path follows the yellow line shown in Figure 1.1. The fibres run underground through the city of Innsbruck, continuing south (still underground) along the main road toward the town of Brenner. Finally, the fibre path reaches the basement of the building at Gewerbepark Mutters-Gärberbach 7. There are two fibre paths on this section,

---

[27] The fibre is attached to the underside of the concrete roof of the car park which has low walls that do not reach the roof.

[28] An OTDR measurement uses laser pulses and measures the reflected light over time, such that the positions of splices can be determined and fibre loss can be measured [83]. The OTDR measurements can be performed with light at different wavelengths. Only the measurements at 1550 nm are relevant for this thesis.

[29] The OTDR reports of all twelve fibres are provided by the company Obrist.

which are rented from the company Innsbrucker Kommunalbetriebe (IKB). Each fibre consists of multiple connected parts; in total, there are 29 connection stations[30]. We expect that these two long fibres are part of a fibre bundle between the connection stations. The two rented fibre paths are dark, which means that no one else is using them. The two fibre paths in this section were characterised by OTDR measurements by IKB in September 2023. The OTDR measurements[31] show that both fibre paths from ZID to Mutters basement have a length of 16.389 km. The first fibre path, which is connected to fibre 1 of section 1 at the ZID room, has a loss of 6.316 dB at 1550 nm (corresponding to an average of 0.385 dB/km). The second fibre path, which is connected to fibre 3 of the first section at the ZID room, has a loss of 5.749 dB (corresponding to an average of 0.351 dB/km). The loss per kilometre in both fibres is higher than the loss of light at 1550 nm in an SMF-28 Ultra optical fibre (as low as 0.173 dB/km) due to the presence of splices and connectors.

3. **Mutters basement to Mutters photon detection station**. A fibre bundle connects the basement and the office on the first floor of the building at Gewerbepark Mutters-Gärberbach 7, where the photon detection station is set up. The connection passes through shafts and enters the photon detection station room through the ceiling, as can be seen in Appendix Figure A.1. There are six fibres in this section, forming a fibre bundle. For the experiments presented in this thesis, the fibres with the labels 1 and 2 are used: fibre 1 is connected to the first fibre path of section 2, and fibre 2 is connected to the second fibre path of section 2. The fibres in this section were characterised by OTDR measurements in October 2023 by Obrist. The OTDR measurements[32] show that the fibres in this section are 80.5 m long and that fibre 1 has a loss of 0.037 dB at 1550 nm while fibre 2 has a loss of 0.246 dB.

Fibres from the three sections are connected to form two continuous off-campus fibre paths that span the entire distance between the Lanyon lab and the Mutters photon detection station. Off-campus fibre path 1 consists of fibre 1 in section 1, the first fibre path in section 2 and fibre 1 in section 3. Off-campus fibre path 2 consists of fibre 3 in section 1, the second fibre path in section 2 and fibre 2 in section 3.

Summing up the results of the OTDR measurements show that off-campus fibre path 1 has a total length of 16.7313 km and a total loss of 6.981 dB at 1550 nm, whereas off-campus fibre path 2 has the same length but a loss of 6.209 dB. Off-campus fibre path 2 is chosen for sending single photons since it shows lower loss than off-campus fibre path 1 on the parts characterised by the OTDR measurements.

---

[30] The document specifying the locations of the 29 connection stations, which are the same for both fibre paths, is provided by IKB.

[31] The OTDR report of the two fibre paths of the second section is provided by IKB.

[32] The OTDR reports of all six fibres are provided by the company Obrist.

4.3. Photon detection station in Mutters

The remote photon detection station was designed and built by Dr. Fabitha Kodakkat during the time of my master's project. The photon detection station consists of two 19-inch racks: a polarisation analysis rack and a SNSPD rack[33]. A picture of the two racks is shown in Appendix Figure A.2. The polarisation analysis rack contains all the necessary optics and electronics for analysing the polarisation of photons and laser light. The SNSPD rack is dedicated solely to the SNSPDs[34].

The analysis rack has several shelves, organised as follows: The uppermost shelf contains a laptop[35] (referred to as Mutters control PC in Figure 4.1), to which all devices in the rack requiring a PC connection are connected. The second shelf from the top holds the optical breadboard, where the polarisation analysis of the incoming photons is performed. The third shelf provides the space for the electronic devices to control the motorised devices on the optical breadboard and for a Universal Serial Bus (USB) hub. The fourth shelf provides the space for a FBG[36], which is used to filter out noise photons at wavelengths differing from 1550 nm, a pulse matcher[37] and an electro-optic converter[38] for sending detector "clicks" back to the Lanyon lab via the off-campus fibre path 1. The pulse matcher adjusts the pulse from the SNSPDs, which are in the range of 0.66 V to 0.84 V in amplitude and 24.9 ns to 26.6 ns length, to be compatible with the working range of the electro-optic converter, which is in a range of +/-4.8 V and $\geq$ 67 ns length. The transmitter (T, Figure 4.1) of the electro-optic converter converts electrical pulses into optical signals at 1550 nm, which can be converted back to electrical signals by the receiver (R, Figure 4.1) after they have travelled through optical fibre. At the bottom of the rack, any excess fibre is coiled up, and the fibre bundle of section 3 is split up into individual fibres in a fibre fan-out box. Vertical connections between the shelves

---

[33] Both 19-inch racks are on wheels. The height of the polarisation analysis racks is about 1.6 m and the height of the SNSPD rack is about 1.9 m.

[34] Single Quantum, Eos 2400 CS. The technical specifications for the Single Quantum SSPD-1550-75-LDCR detectors are: 75 %-80 % system detection efficiency, $\leq$ 1 counts per second (cps) dark count rate, $\geq$ 5 MHz maximum count rate, $\leq$ 40 ps timing jitter at full width at half maximum (FWHM), no after-pulsing. In 2024, the system of the Distributed Quantum Systems group at the University of Innsbruck (DQS) has four 1550 nm detectors and two 854 nm detectors. For the two 1550 nm detectors (driver channel 3 and 4) used in the experiments presented in this thesis, the system's characterisation carried out by the company Single Quantum has shown that the two 1550 nm detectors used for the experiments presented in this thesis have a detection efficiency of 81(3) % and 83(3) % for a wavelength of 1546 nm, a dark count rate of < 1 cps, a timing jitter of 28 ps and 29 ps, an operating current of 17.2 µA and an output pulse amplitude of 840 mV and 660 mV.

[35] Lenovo ThinkPad

[36] AOS Tunable filter at 1551.370 nm in vacuum (Ultra narrow band filter standard, 0.012-0.016 nm bandwidth at FWHM (corresponds to 1.5-2 GHz), <2.0 dB insertion loss, 35 dB SNR, active temperature stabilisation, polarisation-dependent wavelength shift ~0.004 nm, <500 mW power handing, FC/APC connectors. The transmission of the FBG measured by Dr. Fabitha Kodakkat on 17.09.2024 using laser light converted to 1550 nm by the QFC Setup 1 is 0.54(2).

[37] The pulse matcher with signal amplification (of about 4.5x) was provided by Kilian Prokop from the electronics workshop of the Experimental Physics department at the University of Innsbruck.

[38] A.A. Lab-Systems AFL-4800 fibre optic link. SM 1550nm, DC-15MHz. +/-4.8V analog in/out, 2 LVTTL inputs/outputs, optical budget up to 16 dB.

are made by fibres and electronic cables passing between the shelves and the rack's walls and doors. There are feedthroughs on each side of the rack to enable cables and fibres to go into and out of the rack.

The SNSPD rack contains a cryostat with detectors located at the top, to which fibres carrying photons for detection can be connected. The electronic driver, which processes the detector outputs and emits a pulse upon the measurement of a photon, is located at the centre of the rack, and a vacuum pump is located at the bottom. A laptop (referred to as SNSPD PC in Figure 4.1) is placed in the rack below the cryostat and above the electronic driver. The helium compressor, which is also part of the SNSPDs, is placed next to the SNSPD rack.

The sequence of events involved in routing and processing an incoming photon at the Mutters photon detection station is described below. Off-campus fibre path 2 is connected via a fibre joiner[39] to a patch fibre that leads the incoming photon to the FBG, then it is sent via a single-mode optical fibre[40] to the optical breadboard, where it is coupled out into free space. After two mirrors[41], the photon passes through a HWP[42] and a QWP[43] mounted on motorised stages[44]. The two waveplates are followed by a PBS cube[45] such that the configuration shown in Figure 2.2 is achieved and the photon can be measured in any basis. Before the light is coupled at the output ports of the PBS cube into two fibre paths connecting the two racks[46], it passes through a HWP and a QWP on manual rotation mounts to adjust the polarisation, since the SNSPDs are polarisation sensitive. Furthermore, there is a bandpass filter[47] before each one of the two fibre collimators. The signal emitted by the SNSPDs upon a photon detection is adjusted using the pulse matcher, converted into an optical signal by the electro-optic converter and then sent back to the Lanyon lab through the off-campus fibre path 1.

My contributions to the photon detection station were the following:

- I built the polarisation drift compensation setup (described in Section 4.4), which is the key part of this thesis, and includes the shutter, the flip mirror and the polarimeter at the Mutters photon detection station. The polarisation drift compensation setup was designed based on the setup used for polarisation drift compensation in Ref. [16]. Prof. Ben Lanyon, Dr. Viktor Krutianskii, and Dr. Fabitha Kodakkat contributed to the design of the polarisation drift compensation setup. I also modified existing scripts to allow the operation of the entire setup in an automated way.

---

[39] Thorlabs ADAFCPM2 FC/APC to FC/APC Mating Sleeve, Narrow Precision Key (2.0 mm)

[40] Thorlabs SMF-28 fibre

[41] Thorlabs BB1-EO4 broadband dielectric mirrors (1280-1600 nm)

[42] Cening half-waveplate, Quartz, Zero order, optically contacted, Diameter 25.4mm, un-mounted, AR coated for 1550 nm.

[43] Cening quarter-waveplate, Quartz, Zero order, optically contacted, Diameter 25.4mm, un-mounted, AR coated for 1550 nm.

[44] Standa 8MPR16-1 motorized polarizer rotator with 8SMC5-USB-B9-2 controller

[45] Thorlabs PBS124 polarising beamsplitter cube

[46] The fibre paths connecting the two racks consist of two joined shielded single-mode fibres.

[47] Thorlabs FBH1550-12 - Hard-Coated Bandpass Filter, Ø25 mm, central wavelength = 1550 nm, FWHM = 12 nm (corresponding to 1.5 THz)

- I wrote a Python code for characterising the waveplates (optical axis and retardance). I used a Python code written by graduated PhD student Vojtěch Krčmarský to control the waveplate stages, and I got help from Dr. Fabitha Kodakkat to read out the powermeter using Python.
- I monitored the room temperature in the Mutters office and ensured that the air conditioning was serviced. The room temperature is relevant for the operation of the SNSPDs, since the compressor adds heat to the room air and needs a room temperature below 28°C for optimal operation. The air conditioning was set to hold the room temperature below 24°C. The temperature in the room, when the air conditioning is active, fluctuates by up to six degrees between 18°C and 24°C. The frequency of the fluctuation depends on the outdoor air temperature (influencing how fast the room temperature rises). Within the closed analysis rack, the temperature variations are smaller. A second sensor is used to monitor the temperature of the electro-optic converter, which heats up above 30°C.
- I was involved in measuring the central wavelength passing through the FBG in Mutters.
- I created the first digital version of the schematics of the setup used to obtain the results in Chapter 7.
- I helped to unpack and shift some deliveries for the Mutters photon detection station. I also made sure that the packaging materials (pallets and crates) were disposed of properly.
- I occasionally helped out at the Lanyon lab when two people were needed for experiments that required one person in the Lanyon lab and another at the Mutters photon detection station. For example, I assisted when checking the signals sent and received from the electro-optic converter.

4.4. Polarisation drift compensation setup

The polarisation drift compensation setup (shown in pink in Figure 4.1) is designed to compensate for changes to the polarisation of photons caused by off-campus fibre path 2 (alternatively, off-campus fibre path 1 may also be used). The compensation can be performed at intervals and includes a characterisation of the process (process tomography, Subsection 2.3.2), which describes how the fibre affects the polarisation of transmitted light. Polarisation drift compensation forms the key part of this thesis. While Figure 4.1 shows only the main components of the setup, Figure 4.2 presents the complete polarisation drift compensation system, including controllers, physical connections, and power plugs.

The polarisation drift compensation setup is split between the Lanyon lab on Technik campus and the Mutters photon detection station. In the Lanyon lab, there is a 1550 nm laser that serves as a light source for characterising the fibre. In the early experiments of my project, which did not involve single photons and no FBG at the end of the off-campus fibre (results of Chapters 5 and 6), a Thorlabs laser[48] is used. The laser

---

[48] Thorlabs S3FC1550 - DFB Benchtop Laser Source, 1550 nm, 1.5 mW, FC/PC

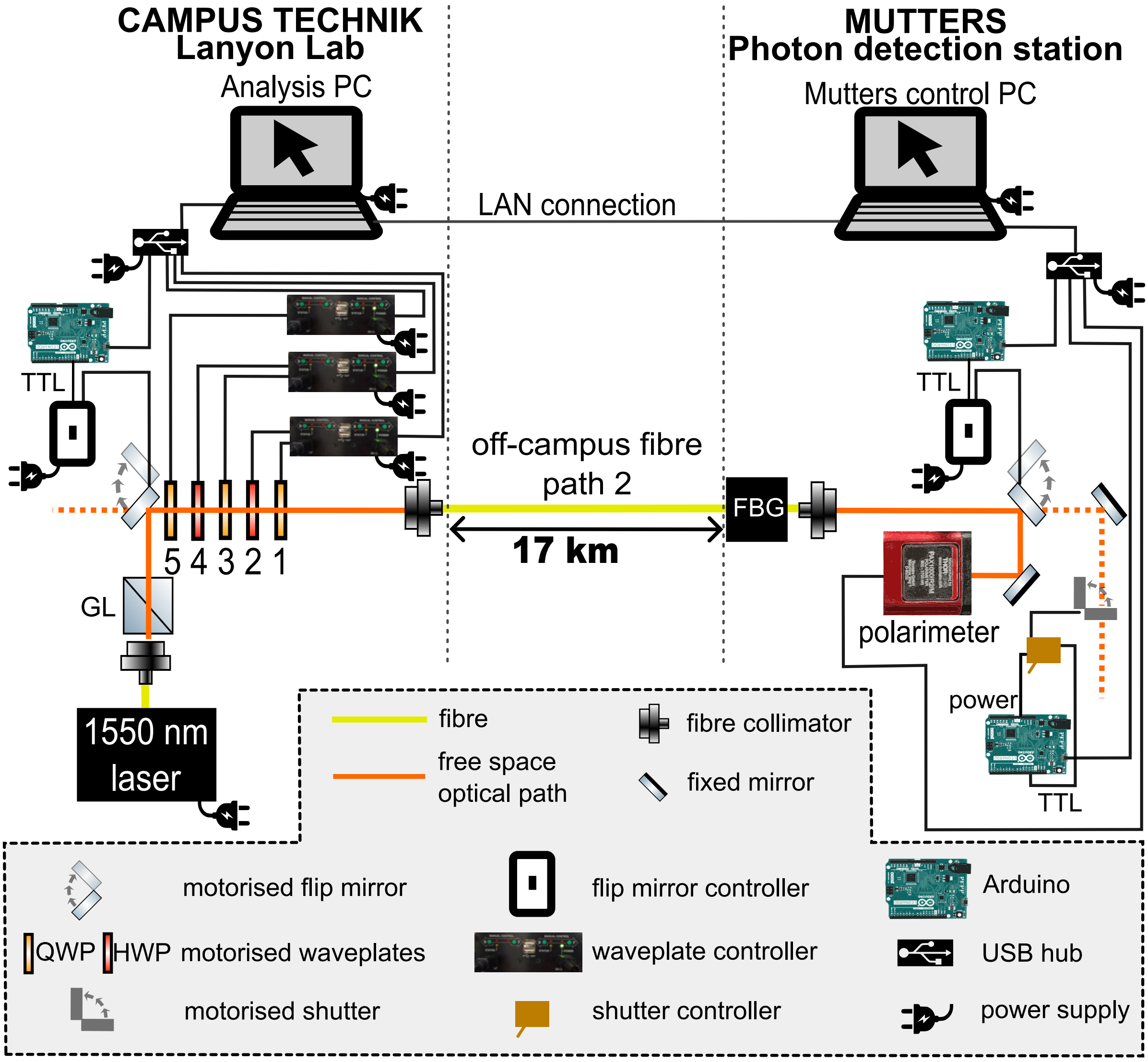

Figure 4.2: Polarisation drift compensation setup. The setup is distributed across two spatially separated locations, connected by off-campus fibre path 2. All electronic connections and controllers for the motorised components are shown. The make and model numbers of the devices are provided in the footnotes of the main text. GL – Glan-laser polariser, FBG – fibre Bragg grating.

has a two-meter-long single-mode fibre at the output which can be connected to a fibre collimator[49] on a breadboard. Introducing the FBG into the setup (done in October 2024) required replacing the Thorlabs 1550 nm laser, as its tuning range was insufficient to reach the FBG resonance. A Toptica 1550 nm laser[50] was chosen as a replacement, offering a broader tuning range that could be matched to the FBG. The Toptica 1550 nm

---

[49] Schäfter+Kirchhoff 60FC-SF-4-A11-45

[50] Toptica DL pro - Grating stabilised tunable diode laser with digital control DLC pro, Laser class 3B, Wavelength = 1380-1690 nm

laser is placed on a table dedicated to lasers, and its light is delivered to the polarisation drift compensation setup via a polarisation-maintaining fibre[51]. The Toptica 1550 nm laser is used for the polarisation drift compensation presented in Chapter 7.

As shown in Figure 4.2, the 1550 nm laser light, which is outcoupled from the fibre collimator, is polarised via a GL[52] and then flipped into the path, where otherwise photons are sent, using a mirror on a motorised mount[53]. The position of the flip mirror is controlled using a TTL signal, which is generated via an Arduino[54] upon a command from a PC. The PC[55] in the control room of the Lanyon lab that sends commands to the Arduino is called the *Analysis PC*. The TTL signal goes to the mirror controller, which is connected to the mirror mount. Then, the polarised light passes through a combination of QWPs and HWPs[56], numbered 1 to 5 in Figure 4.2, which can change the polarisation state of the light. The waveplates are mounted on motorised stages connected to controllers[57], to which the Analysis PC can send commands via an USB connection. As the Analysis PC is not located in the lab itself, but in a neighbouring control room, all USB cables are bundled into a USB hub. After the waveplates, the light is coupled into off-campus fibre path 2.

In Mutters, in the polarisation analysis rack, laser light is coupled out of the fibre and reflected by another motorised flip mirror, which directs the laser light onto a polarimeter. The polarimeter[58] is used to measure the polarisation of the laser light. The motorised mirror[59] is not fully reflective, so it is covered on the back, otherwise the SNSPDs will measure an increased number of counts when laser light is sent to the polarimeter. To further protect the SNSPDs, a motorised shutter[60] is installed between the motorised flip mirror and the motorised waveplates on the polarisation analysis breadboard. The shutter prevents laser light from falling onto the SNSPDs in the case that the motorised flip mirror fails to flip. The shutter is controlled via a separate electrical board, which accepts TTL signals for controlling the shutter's position. The electrical board also allows the range of rotation of the shutter blade to be adjusted. The polarimeter, the flip mirror and the shutter receive TTL signals from the Mutters control PC (Figure 4.2). The Mutters control PC can communicate with the Analysis PC in the Lanyon lab thanks to a metropolitan area network of the University of Innsbruck [86].

---

[51] Thorlabs P3-1550PM-FC-10, PM, FC/APC, 1440-1625nm, length 10 m, diameter 125 µm, 0.125, Panda, Patch cable

[52] Thorlabs Mounted Glan-Laser Polariser GL10. Extinction ratio 100000:1 in transmission [84]. A GL is designed to be used as a polariser and transmit highly pure polarised light, in contrast to a PBS cube used to split light based on its polarisation.

[53] Newport 8892-M-K Motorised flipper mount

[54] Arduino Leonardo AOOOO57 Core AT Mega32

[55] Thermaltake

[56] Cening half and quarter-waveplate, Zero order, optically contacted, Diameter 25.4mm, un-mounted, AR coated for 1550 nm.

[57] Standa 8MPR16-1 motorised polariser rotator with 8SMC5-USB-B9-2 controller.

[58] Thorlabs PAX1000IR2(/M). The polarimeter consists of a rotating QWP and a polariser, followed by a photodiode. More details on the operating principle of the polarimeter can be found on the Thorlabs web-page [85].

[59] Thorlabs BB1-EO4 broadband dielectric mirrors (1280-1600 nm)

[60] Jamara Servo High End Micro, Tower Pro S G-50 with home-built control board.

5. Off-campus fibre characterisation

To perform two out of four characterisations on the off-campus fibres, without travelling to Mutters for each experiment, the fibre ends are joined together in Mutters. Specifically, the end of off-campus fibre path 1 at the Mutters photon detection station is connected to the end of off-campus fibre path 2 using a fibre joiner. The resulting fibre loop is referred to as the *off-campus fibre loop*. The input of the off-campus fibre loop is labelled A and the output is labelled C in Figure 4.1. No filters are involved in these measurements, beyond the bandwidths of the detectors used.

Section 5.1 characterises the fibre loop in terms of background photons, measured at its output when no light is injected. Section 5.2 addresses polarisation drifts, describing how the polarisation of light changes as it propagates through the fibre loop. Section 5.3 focuses on the transmission efficiencies of the two off-campus fibres, considered separately. Finally, Section 5.4 characterises fibre path 2 in terms of polarisation-dependent loss (PDL).

If not stated otherwise, the uncertainties of the values given in this and the following chapters correspond to one standard deviation and represent the statistical error. The uncertainties are given in brackets after the respective values and apply to the last digit(s) of the written value. Gaussian error propagation is used to propagate the uncertainties. Asymmetric error bars are written explicitly, with the upper and lower uncertainties shown as superscripts and subscripts, respectively.

5.1. Background photons

Even when no light is sent into the fibre at the input, photons may still leak in from neighbouring fibres or the environment. When conducting experiments with single photons, these background photons can affect the outcome of the experiment. For instance, the presence of background photons can reduce the fidelity of the ion–photon entangled state to a Bell state because the background photons dilute the signal of the photons that are actually entangled with the ion. Measuring the background photons indicates whether additional filters are required for the experiments involving single photons (Chapter 7) and whether there are fluctuations due to the day–night cycle.

The off-campus fibre loop is used to take the following data. The fibre end labelled A in Figure 4.1 is covered with two fibre dust caps (one T-shaped and one black dust cap for the fibre bulkhead), ensuring that no light is coupled into the fibre. The fibre end labelled C in Figure 4.1 is connected via a fibre joiner to a fibre leading to the superconducting nanowire single photon detector (SNSPD) for 1550 nm in the Lanyon lab. According to Ref. [68], the SNSPD has a bandwidth of approximately 20 nm. More information on the SNSPDs in the Lanyon lab can be found in Subsection 3.1.1. No additional optical filters are used. The lights in the Lanyon lab are on. The lights at the Mutters photon detection station are off. The effect of the lights in the Lanyon lab is considered later. The photon counts registered on the SNSPD are recorded for almost three days, as shown in Figure 5.1. The minimum and maximum background photon counts registered are $117\,\mathrm{s}^{-1}$ and $604\,\mathrm{s}^{-1}$, respectively. There are fluctuations in the number of background photons registered. The fluctuations are not clearly correlated with day or night. The

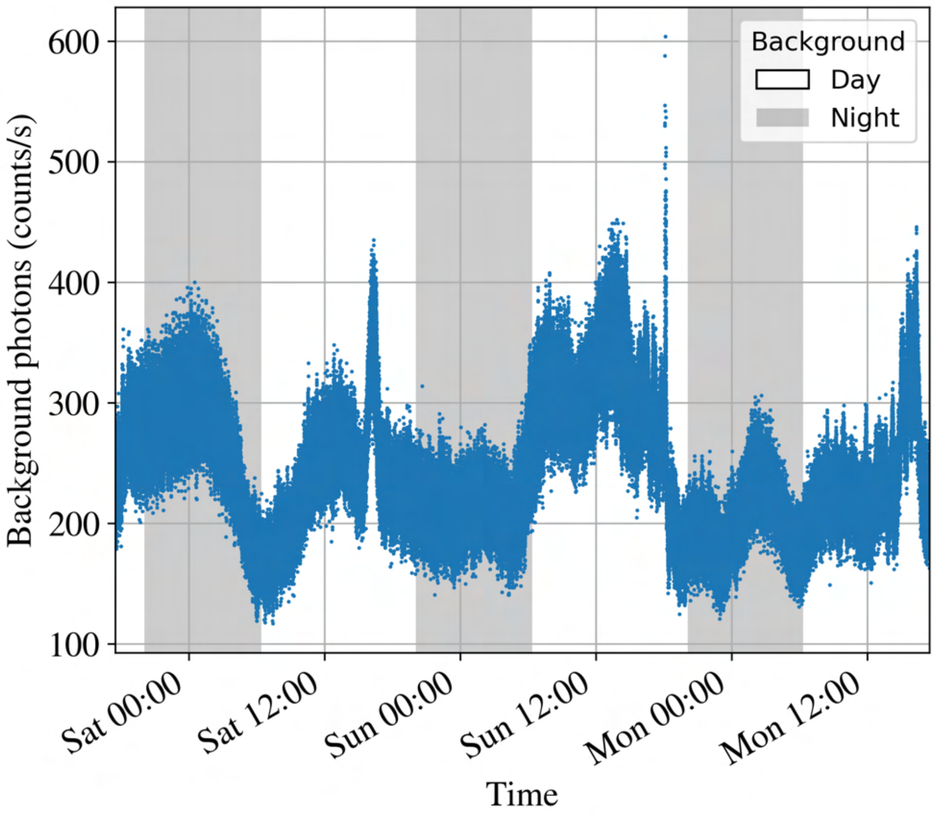

Figure 5.1: Background photon counts in the 34 km-long off-campus fibre loop. The background photon counts are measured by a 1550 ± 10 nm detector. The dark background of the plot shows the nighttime between sunset and sunrise. The sunrise and sunset times in Innsbruck are obtained using the Python package *suntimes* [87] and the coordinates of Innsbruck (longitude: 11.384234° E, latitude: 47.259850° N, altitude: 579.2 m) [88]. Measurements are taken from 12.04.2024 to 15.04.2024.

origin of the photons may be external light or data traffic in nearby fibres. The data are collected over the weekend. The state of the room lights in the Lanyon lab and the Mutters photon detection station should have remained unchanged throughout the duration of the measurements, which is important because the room lights would affect the measured background counts. The Lanyon lab has no windows, and the off-campus fibre paths are underground except for the parts where the fibres enter or exit buildings. Possible causes for the fluctuations are sunlight shining through the windows of the room of the Mutters photon detection station or on the off-campus fibre path in the underground car park at Technikerstraße 25. The weather conditions in Innsbruck during the measurement are shown in Appendix A.3.1. Another possible cause for varying background counts is varying data traffic in nearby fibres.

Additional measurements are taken to investigate the effect of the room lights in the Lanyon lab and in the room of the Zentraler Informatik Dienst at the University of Innsbruck (ZID) on the background photons in the off-campus fibre loop. These measurements are shown and discussed in Appendix A.3.2 and summarised in the following. Measurements of background photons in the off-campus fibre loop were taken over a time period of five minutes, during which the Lanyon lab lights were switched on and off repeatedly for one minute at a time. With the lights on, the count rate measured by the SNSPD in the Lanyon lab is $212.3(11)\,\mathrm{s}^{-1}$, and with the lights off, it decreases to $157.4(13)\,\mathrm{s}^{-1}$. The quoted uncertainties correspond to the square root of the average counts over the measurement time for each lighting condition, assuming Poissonian statistics. Repeating the same measurement a week later over a time period of ten minutes, but with the lab lights constantly off and switching the lights in the ZID room on and off for two minutes at a time, shows that the effect of the lights in the ZID room is less pronounced. The background photon rate increases from $261(4)\,\mathrm{s}^{-1}$ to $288(2)\,\mathrm{s}^{-1}$ when the lights in the ZID room are switched on. Therefore, as one might expect, the farther the room lights are from the photon detector, the less pronounced is the effect of the lights on the measured background photon rate. Measurements of background photon rates with the lights on and off in both the Lanyon lab and the ZID room indicate that it is preferable to keep the lights off during experiments involving photons emitted by the ion. Doing so reduces background counts, thereby maximising the signal-to-background ratio and improving the detection fidelity of ion-generated photons, as implemented in Chapter 7.

The off-campus fibre loop is not utilised for experiments with single ion-emitted photons. Instead, only off-campus fibre path 2 is used to send photons. The room lights in the Lanyon lab significantly affect the background counts in the fibre loop configuration, as they couple into both the beginning and the end of the fibre loop. In contrast, the background photons coupled into off-campus fibre path 2 in the Lanyon lab will be attenuated along the path to the Mutters photon detection station.

For comparison, the number of background photons detected with an SNSPD[61] in the deployed fibre link presented in the Saarbrücken network of Ref. [31] also fluctuates, reaching almost $10^5\,\mathrm{s}^{-1}$. The authors use a broadband-suppression optical filter with a 250 MHz transmission window to reduce the background photon counts to an average of $19.7\,\mathrm{s}^{-1}$ [31].

Following the installation of the SNSPDs at the Mutters photon detection station (July 2025) and the use of the analysis board with the bandpass filters[62], Dr. Fabitha Kodakkat measured the background photons at the output of off-campus fibre path 2 in Mutters (D in Figure 4.1). It was observed that sending light from the electro-optic converter in Mutters through off-campus fibre path 1 (from B to A in Figure 4.1) introduces tens of additional photon counts per second to the background measured at the output of off-campus fibre path 2. We expect that the laser light generated by the electro-optic converter and sent through fibre path 1 leaked across into the co-propagating fibre path 2, through which photons are sent. Therefore, the fibre Bragg grating (FBG)[63]

---

[61] Quantum Opus One. The efficiency at 1550 nm is > 80 % [31]. The full width at half maximum (FWHM) bandwidth is about 250 nm (32 THz), estimated from the nanowire datasheet in Ref. [89].

[62] The filters have a bandwidth of 12 nm to 16 nm at FWHM, more information on the filters can be found in Subsection 3.1.1.

[63] The FBG has a bandwidth of 0.012–0.016 nm, more information can be found in Section 4.3.

was subsequently installed at the output of off-campus fibre path 2 in Mutters (D in Figure 4.1). The output of the FBG is connected to the photon analysis board, whose two outputs are connected to two channels of the SNSPD. The input of fibre path 2 in the Lanyon lab (C in Figure 4.1) is capped in order to measure the background photons at the output of off-campus fibre path 2. In this configuration, with the electro-optic converter operational, an average of $1.209(4)\,\mathrm{s}^{-1}$ background photons (sum of the two used SNSPD channels) is measured over 23 hours[64]. The error bar on the reported average is calculated by assuming a Poissonian distribution for the total number of counts over the entire measurement duration, followed by Gaussian error propagation when dividing by the measurement time to obtain the average counts per second (cps). For comparison, the detector's dark count rate is $\leq 1\,\mathrm{s}^{-1}$ for each channel (as given by the specification sheet of the detectors).

5.2. Polarisation drifts

In the experiments involving single photons presented in this thesis, quantum information is encoded in the polarisation of the photons. Fibre birefringence depends on strain, stress, and temperature, all of which can vary with time. Consequently, a fibre is expected to alter the polarisation of light transmitted through it over time[65]. From now on, changes in polarisation of the light are referred to as polarisation drifts. Characterisation of the polarisation drift reveals how far the state has deviated over time and, consequently, how frequently compensation for the drift must be applied. This section reports on a characterisation of the polarisation drifts in the off-campus fibre loop.

The data in this section are acquired using a setup differing from that shown in Figure 4.2 in the following aspects: the setup has a fixed mirror instead of the flip mirror in the Lanyon lab, the off-campus fibre loop whose output in the Lanyon lab (C in Figure 4.1) is connected to the fibre-coupled optical input of a polarimeter (Thorlabs PAX1000IR2(/M), the one presented in Section 4.4), and the setup contains only two waveplates (after the Glan-laser polariser (GL), there comes a quarter-waveplate (QWP) and then a half-waveplate (HWP)). Both the polarimeter and the waveplates are connected to the same PC, namely the Mutters control PC, which was kept in the Lanyon lab before the Mutters photon detection station was built. The Thorlabs laser operating at 1550 nm is used and no single photons are involved.

To characterise the Choi matrix (Subsection 2.3.2) describing the process implemented by the fibre on polarised light, the following six input states are used: $|R\rangle$, $|V\rangle$, $|A\rangle$, $|H\rangle$, $|D\rangle$, and $|L\rangle$[66]. Each input state is prepared by appropriately adjusting the waveplate

---

[64] The measurement was performed on 18.–19.09.2024.

[65] There exist polarisation-maintaining fibres, but these fibres would not work for our application. The reason is that to maintain polarisation, the light coupled into the fibre must be linearly polarised and aligned with respect to the fibre's axis. However, photons that are entangled with an ion in our experiment in Chapter 7.2 do not have a fixed polarisation and therefore, they cannot be aligned to the fibre's axis. Furthermore, telecom fibres in standard networks (as for exchange of classical data) are usually not polarisation-maintaining.

[66] The sequence of input states is chosen to minimise the time needed to rotate waveplates between the preparation of one state and the following state.

angles. For each input state, the light is transmitted through the off-campus fibre loop, and the state of the light at the output of the off-campus fibre loop is measured using the polarimeter. About twelve seconds are needed to prepare and measure all six states. For each prepared state, after the waveplates stopped rotating, about 0.1 s are used to let the light travel through the fibre loop and read out the polarimeter. The polarimeter operates at a sample rate of 30 Hz and for each input state, one sample is measured. Therefore, the majority of the time is spent rotating the waveplates. A complete set of data for process tomography is obtained once all six input states have been prepared and their corresponding output states measured. The Choi matrix can then be reconstructed from the data by process tomography (see Subsection 2.3.2).

To monitor the temporal evolution of the polarisation, the complete six-state preparation and measurement cycle is repeated at regular intervals. A fixed time interval, denoted by Δt, of ten minutes is introduced between the end of one preparation and measurement cycle and the beginning of the next. The time required to perform the preparation and measurement cycle (each twelve seconds) is therefore not included in this ten-minute interval.

The Stokes parameters for the six input states measured over four and a half days are shown in Figure 5.2a. The fidelity of the Choi matrix at time t with the first Choi matrix at time t_0, according to Equation (2.44), is shown in Figure 5.2b. One large jump is visible in the fidelity, indicating that the polarisation changed drastically compared to other times. The changes in fidelity seem to be partially correlated to the outdoor air temperature in Innsbruck: both values rise and fall in about the same timescales and show in some time intervals similar shapes in parts of the graph (Figure 5.2b). However, there is a temporal delay between changes in the outdoor air temperature and changes in the fidelity, and the fidelity does not always have the same features as the temperature. The fidelity between Choi matrices separated by ten and thirty minutes is shown in Figure 5.2c. Over the four and a half days of data, during which a total of 647 Choi matrices are obtained, the fidelity for a ten-minute interval $\mathcal{F}(E(t), E(t-\Delta t = 10\,\text{min}))$ is greater than 0.999 in 96.1 % of the cases. For a 30-minute interval, the fidelity is greater than 0.99 in 97.8 % of the cases. There are no error bars for the fidelities in Figures 5.2b and 5.2c. However, the errors for the fidelities are estimated in a separate experiment[67] to be on the order of 10^{-4} for each data point.

The dependence of the fidelity $\mathcal{F}(E(t), E(t-\Delta t))$ on the time interval Δt is shown in Figure 5.3. The coloured lines show different thresholds. For example, 99 % of the measured Choi matrices lie above the red line. One can thus see that, in Figure 5.3a for example, Choi matrices compared 60 minutes apart have a fidelity of 0.9 in 99 % of the cases. A comparison between Figure 5.3a and Figure 5.3b shows that while the 90 % percentile remains almost unchanged, the 99 % percentile is significantly affected by

---

[67] The experiment for estimating the error bars was done using off-campus fibre path 2, with the setup described in Section 4.4. The measurement procedure involved taking 100 data points for each input state before moving to the next one. From these data, 100 Choi matrices were reconstructed for each cycle, and the corresponding fidelities $\mathcal{F}(E(t), E(t_0))$ and $\mathcal{F}(E(t), E(t-\Delta t))$ were computed. The standard deviations of the ensemble of fidelities are used to estimate the order of magnitude of the error bars.

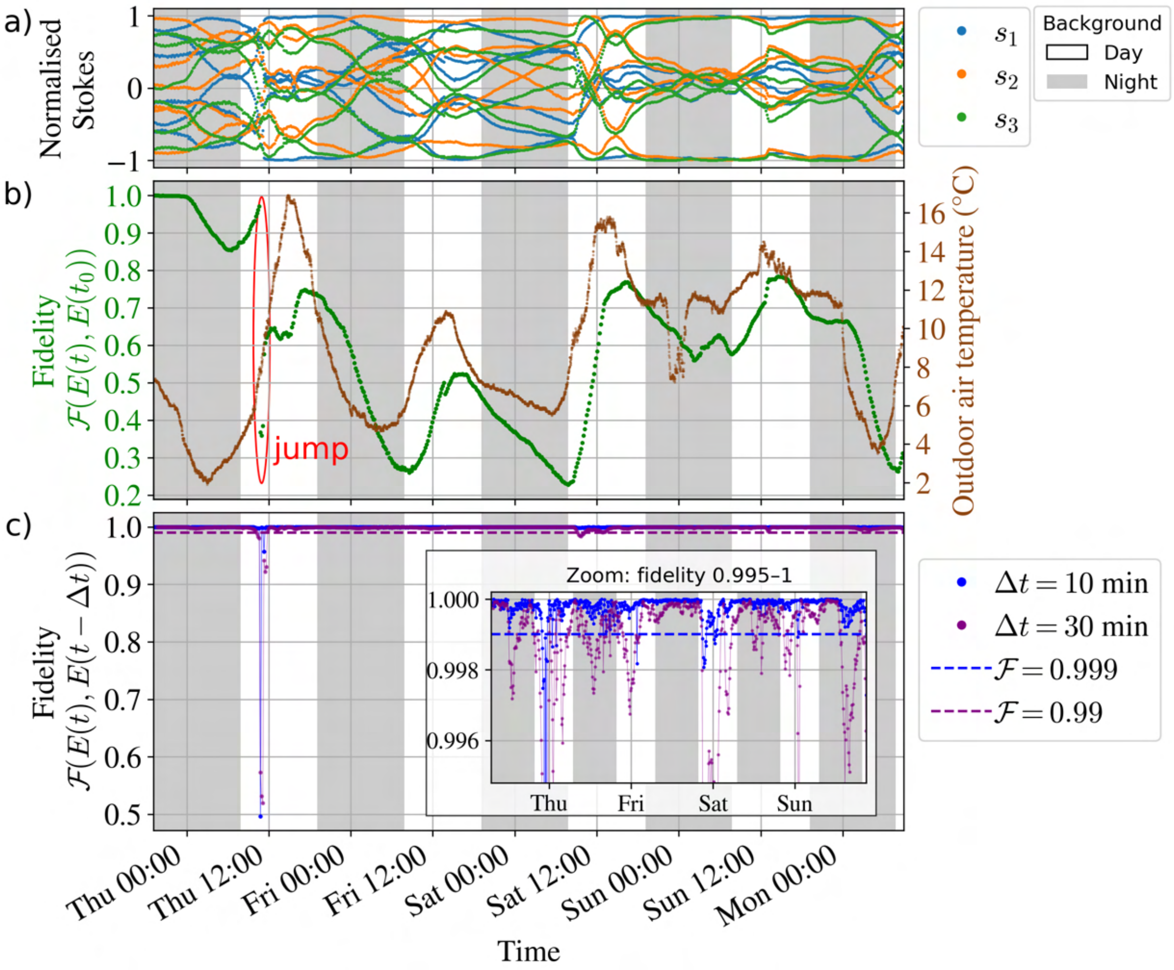

Figure 5.2: Polarisation drift in the 34 km-long off-campus fibre loop. The grey background colour shows nighttime (sunset to sunrise), while the white background shows daytime (between sunrise and sunset). a) Stokes parameters over time for all six prepared states. b) Fidelity between the Choi matrices describing the process implemented by the fibre loop on polarised light at time t (Choi matrix $E(t)$) and at the start time on Wednesday evening (Choi matrix $E(t_0)$), and the outdoor air temperature measured in Schöpfstraße 45, Innsbruck, by Zentralanstalt für Meteorologie und Geodynamik in cooperation with the Department of Atmospheric and Cryospheric Sciences of the University of Innsbruck [90]. c) Fidelity between the Choi matrices $E(t)$ and $E(t-\Delta t)$ for a ten-minute and thirty-minute time difference. Measurements taken from 28.02.2024 to 04.03.2024.

the jump shown in Figure 5.2b. Especially for shorter time intervals Δt, the fidelities are affected and the percentiles are distorted in Figure 5.3a compared to Figure 5.3b. Figure 5.3 can be used to estimate how often polarisation drift compensation of the off-campus fibre is required in an experiment, given a chosen percentile and fidelity threshold, assuming that the polarisation drift is comparable to that observed during the

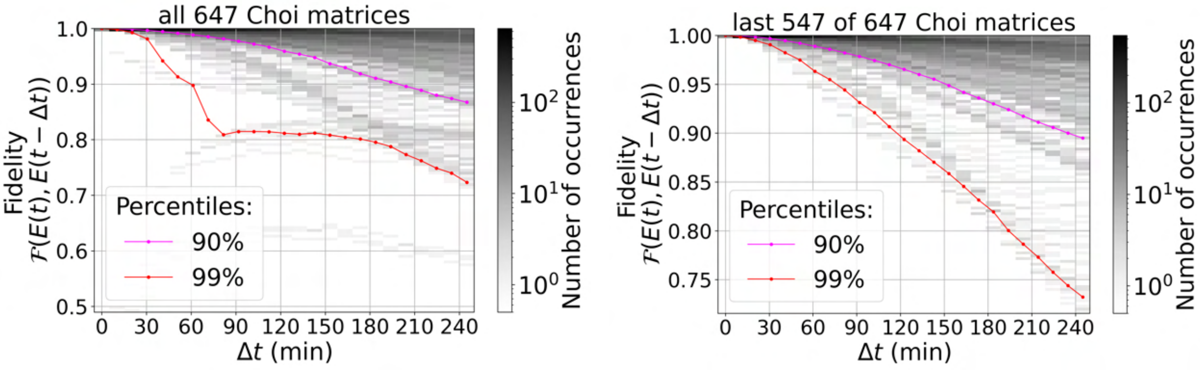

(a) All data. **(b)** Data after jump.

Figure 5.3: Process fidelity as a function of the time interval. The same data used in Figure 5.2 is used to make plot (a). Plot (b) shows only the data collected after the jump identified in Figure 5.2b. For each Choi matrix, fidelities between the quantum process at time t and at earlier times $t - \Delta t$ are computed. These fidelities are grouped into 100 bins between the minimal and maximal fidelity, and the absolute number of occurrences of the fidelity values in these bins is visualised using a grey-scale heatmap. Overlaid on the heatmap are the 90 % (magenta) and 99 % (red) percentiles, which indicate the fidelity thresholds above which 90 % and 99 % of the measurements lie, respectively. Dots mark the calculated percentiles and are connected to visually guide the eye. The concept and visual style of this plot are inspired by Figure 5 of Ref. [31].

4.5-day measurement period.

The polarisation of light sent through the 14 km-long urban fibre[68] of Ref. [31] changes on average faster than in the deployed fibre presented in this thesis. For example, Figure 5c of Ref. [31] shows that the 99 % percentile after ten minutes is at a threshold fidelity of approximately 0.7. The authors attribute many of the observed polarisation drifts to the 1.3 km-long section of the urban fibre that runs above ground. In contrast, the changes measured in this thesis for the 34 km-long underground off-campus fibre loop are significantly slower: the 99 % percentile remains above a threshold fidelity of 0.7 even after four hours.

5.3. Transmission efficiency

The ratio between the power of light sent into a fibre and the power measured at the output of the fibre is referred to as the fibre transmission efficiency. The transmission efficiency of the off-campus fibre paths at 1550 nm is one of the key factors in estimating the photon detection efficiency at the Mutters photon detection station.

The Thorlabs laser emitting at 1550 nm with fibre-coupled output is used to perform

---

[68] The polarisation drift is characterised using only two polarisations of light sent into the fibre, and therefore, the methods used to obtain the process fidelity differ from those employed in this thesis.

the measurements. Powermeters[69] with fibre adapter caps[70] are used to measure the optical power at both the input and output of the fibres. For each off-campus fibre, the power P_{in} is first measured in the Lanyon lab at the output of the fibre from the laser (by Dr. Fabitha Kodakkat). After the fibre from the laser is joined with a fibre joiner to the input of the off-campus fibre (A or C in Figure 4.1, depending on which off-campus fibre path is to be measured), the power P_{out} at the output of the off-campus fibre (B or D in Figure 4.1, depending on the fibre path measured) is measured at the Mutters photon detection station by me. The input and output power measurements are performed up to five minutes apart, allowing time to connect and disconnect fibres[71], and time to clean the output of the fibre from the laser. The described measurement procedure was repeated three times for each off-campus fibre. The measurements were taken on 18.06.2024.

The ratio $T = P_{\text{out}}/P_{\text{in}}$ between the measured output power P_{out} and input power P_{in} is calculated. The average of the three measurements is used to determine the transmission efficiencies. The given error is the standard error in the mean[72]. The results are:

- $T = 0.205(8)$ for off-campus fibre path 1, and
- $T = 0.192(3)$ for off-campus fibre path 2.

The transmission efficiency T is converted into optical transmission loss L in decibels (dB) using the relation $L = -10\log_{10}(T)$. The corresponding losses are 6.89(18) dB for fibre path 1 and 7.17(7) dB for fibre path 2. The loss measured for off-campus fibre path 1 agrees, within the standard deviation, with the value of 6.981 dB of the optical time domain reflectometer (OTDR) measurements reported at the end of Section 4.2. In contrast, the loss measured for off-campus fibre path 2 deviates by 0.96(7) dB from the previously reported value of 6.209 dB given at the end of Section 4.2. Possible causes for the difference include contamination (dirt, dust) on the fibre end faces, and the fact that the measured power P_{in} is not directly the power of the light going into the fibre but just the power of the light coming out of the laser (which is then sent into the fibre loop using a fibre joiner).

For an ideal fibre with a loss of 0.2 dB/km at 1550 km and the same length of the off-campus fibre path (16.7313 km), the transmission efficiency would be 0.46. Therefore, the measured transmission efficiency of the off-campus fibre paths is about half of the expected transmission for an ideal fibre without any splices, connectors and fibre fan-out boxes.

---

[69] Thorlabs S148C — Integrating Sphere Photodiode Power Sensor, Extended InGaAs, 1200–2500 nm, 1 µW – 1 W. S/N: 16022502 in the Lanyon lab, S/N: 16060411 in Mutters.

[70] Thorlabs S120-APC

[71] At the Mutters photon detection station, additional measurements using a patch fibre and the polarimeter instead of the powermeter are performed in the five-minute interval. These additional measurements are not taken into account in this thesis.

[72] The standard error in the mean is calculated by dividing the standard deviation (defined in Equation 2.3 in Ref. [91]) by the square root of the number of measurements.

5.4. Polarisation-dependent loss

PDL is a non-trace-preserving process and cannot be compensated using waveplates. To ensure that PDL is not the dominant limit in the experiments of Chapter 7 involving photonic polarisation qubits, it is measured separately.

The setup shown in Figure 4.2, which uses the Thorlabs 1550 nm laser, is modified to measure the PDL of off-campus fibre path 2. In the Lanyon lab, a microscope slide is inserted between the GL and the flip mirror at an angle of 45° to the incoming beam. The purpose of the microscope slide is to reflect a portion (approximately 17 %) of the light transmitted through the GL, enabling its power to be monitored. A powermeter[73] is used to measure the light reflected from the microscope slide. A second powermeter of the same type measures the light transmitted through the microscope slide, the subsequent waveplates, and a medium under test for PDL. The media under test for PDL are a 2 m-long single-mode fibre (light is coupled into it using a fibre collimator), and the same 2 m-long fibre joined with off-campus fibre path 2.

Waveplates 3, 4, and 5 (Figure 4.2) are fixed with their optical axes aligned at 0° with respect to the vertical direction (direction of gravity), while waveplates 1 and 2 (Figure 4.2) are adjusted to prepare a set of polarisations distributed over the Bloch sphere. Specifically, the QWP angle is set to ten discrete values between 0° and 90°. For each fixed QWP angle, the HWP is continuously rotated through 90°, during which the reflected and transmitted powers are simultaneously recorded.

Each PDL measurement takes approximately two minutes. The power measured by the second powermeter is normalised by the power of the light reflected by the microscope slide, such that possible power fluctuations caused by the change in polarisation in the fibre between the laser and the GL are taken into account. The ratio corresponds to the transmission T up to a scaling factor. The scaling factor cancels out when calculating the ratio between two transmissions. The single points of maximum transmission and minimum transmission (up to the scaling factor) over the measurement set are identified as T_{max} and T_{min}, respectively, and inserted into Equation (2.46) to obtain the PDL.

The measured PDL is 0.274(16) dB, calculated using the maximum and minimum transmission out of 1533 measurement points (shown in Appendix A.4) and Equation (2.46). The uncertainty in the PDL is obtained by estimating the statistical error (standard deviation) on the measured powers using a separate five-minutes-long measurement of the powers[74] during which the waveplates are not rotated. Linearity errors of the used powermeters [92] are not taken into account. The PDL of the 2 m fibre alone, measured 1.5 hours later on the same day using the same powermeters, is 0.284(16) dB. Therefore, the PDL of the 17 km-long off-campus fibre path 2 alone is calculated to be -0.01(2) dB. Consequently, there is no PDL caused by the fibre resolvable within 0.02 dB.

One possible cause for the observed PDL is beam displacement caused by the rotating waveplates. If, for certain waveplate angles (corresponding to specific prepared polari-

---

[73] Thorlabs S148C - Integrating Sphere Photodiode Power Sensor, Extended InGaAs, 1200-2500 nm, 1 µW to 1 W.

[74] The five-minute-long measurement has a total of 3170 measurement points for the power reflected by the microscope slide and 3184 measurement points for the power after the off-campus fibre path 2.

sations), only a portion of the beam reaches the powermeter, these polarisations may appear to experience a higher loss than others. Similarly, contamination (e.g., dust or dirt) on the surfaces of the waveplates can lead to variations in the detected optical power as the waveplates are rotated. This may affect the measured minimum transmission $T_{\min}$ and, consequently, influence the PDL measurements.

For comparison, the PDL reported in Ref. [31] for a 14 km-long fibre is 0.08(9) dB. The PDL is derived from a six-day-long measurement involving a fibre loop of 28 km and subtracting the PDL of the measurement setup.

5.5. Conclusion

In this chapter, the off-campus fibre was characterised with respect to background photons, polarisation drifts, transmission efficiency, and PDL. A summary and the main conclusions of each characterisation are now presented.

On the order of hundreds of background photons per second were detected at the output of the off-campus fibre loop. The measurement was conducted over almost three days, using a detector with a bandwidth of 20 nm at FWHM centred around 1550 nm. This background was found to be partially due to the room lights in the Lanyon lab. Probably, other external light sources along the fibre path also contributed to the background photon counts. The number of background photons fluctuated over time, from approximately one hundred to a maximum of six hundred. These fluctuations may result from changes in the external light sources or from varying data traffic in nearby fibres. By adding a filter with a specified bandwidth of 0.012–0.016 nm at FWHM, the background counts in the off-campus fibre path 2 could be reduced to 1.209(4) s^{-1} when measured over a period of 23 hours, corresponding to the detectors' dark count rate.

The polarisation of light sent through the off-campus fibre loop was found to vary over time due to the fibre's influence. Significant changes typically did not occur within ten minutes, but rather over several tens of minutes to hours. For example, the infidelity over a half-hour period was on the order of 1 %, based on measurements taken over 4.5 days. For experiments lasting several hours and involving polarised or ion-entangled photons transmitted through the off-campus fibre, characterising and correcting for polarisation drifts every half hour should be sufficient to monitor and compensate for significant changes in the polarisation of light sent through the off-campus fibre.

The transmission efficiencies at 1550 nm of off-campus fibre paths 1 and 2 were measured to be 0.205(8) and 0.192(3), respectively. For an ideal fibre with a loss of 0.2 dB/km at 1550 km and the same length as the off-campus fibre path, the expected transmission efficiency of 0.46 would be twice as high. The reduced efficiency can be attributed to splices, connectors, and fibre fan-out boxes, as confirmed by OTDR measurements carried out by external companies.

No PDL of the off-campus fibre path 2 could be measured, at the level of 0.02 dB statistical precision in my measurements. However, for other parts of the setup used, the measured PDL is not negligible. In particular, we conclude that the rotation of the waveplates can cause beam steering, which alters the measured powers coupled into optical fibre and can therefore appear as PDL.

6. Polarisation drift compensation of laser light over the off-campus fibre

The measurements presented in Section 5.2 show that the birefringence of the off-campus fibre changes over time and affects the polarisation of light sent through the fibre. Therefore, when experiments with single polarised photons are performed over several hours, the polarisation drift in the fibre should be compensated at regular intervals. This chapter presents the procedure used for periodic polarisation drift compensation in the off-campus fibre path 1 (Section 6.1) and its results (Section 6.2).

6.1. Procedure for the periodic polarisation drift compensation

The setup used to take the measurements presented in this section is shown in Figure 4.2, but with a few modifications.

- A fixed mirror is used instead of a flip mirror in the Lanyon lab.
- Off-campus fibre path 1 is used instead of off-campus fibre path 2.
- At the Mutters photon detection station, off-campus fibre path 1 is joined with a patch fibre that is plugged directly into the polarimeter. Therefore, no fibre Bragg grating (FBG), fibre collimator or mirrors are used at the Mutters photon detection station.
- The Thorlabs 1550 nm laser is used as a light source.

Unlike the results shown in Section 5.2, where both off-campus fibre paths 1 and 2 are used as part of the off-campus fibre loop, the data presented in this section are obtained using only the 17 km-long off-campus fibre path 1. While experiments with the off-campus fibre loop allow both the waveplates and the polarimeter to be connected to the same PC, those devices are now located in separate physical locations: the laser and waveplates are located in the Lanyon lab, while the polarimeter is located at the Mutters photon detection station. Consequently, the waveplates are controlled by the analysis PC in the Lanyon lab, and the polarimeter is controlled via the Mutters control PC. To synchronise the state preparation with the waveplates and the polarisation measurements with the polarimeter, the two PCs have to communicate with each other. This communication between the two PCs is achieved by setting up a so-called "client–server connection" [93] within the university's metropolitan area network [86]. The client–server connection enables a Python script to be run on each PC and condition the execution of a command upon a message from the other PC. The Mutters control PC is configured as the client, and the analysis PC is configured as the server.

The experiments in Ref. [16] involve a 230 m-long fibre on campus. The polarisation changes caused by that fibre were characterised by Vojtěch Krčmarský by sending single polarised photons through the fibre and were compensated for by using motorised waveplates, as briefly explained in Section II of the Supplementary Material of Ref. [16]. I took and adapted the Python code used for polarisation drift compensation in Ref. [16] to perform polarisation drift compensation of off-campus fibre path 1. Adaptations include the use of a laser light source instead of single photons for characterising the polarisation

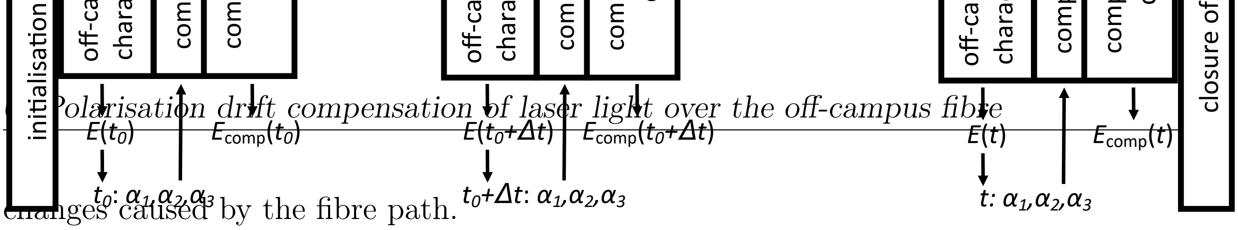

changes caused by the fibre path.

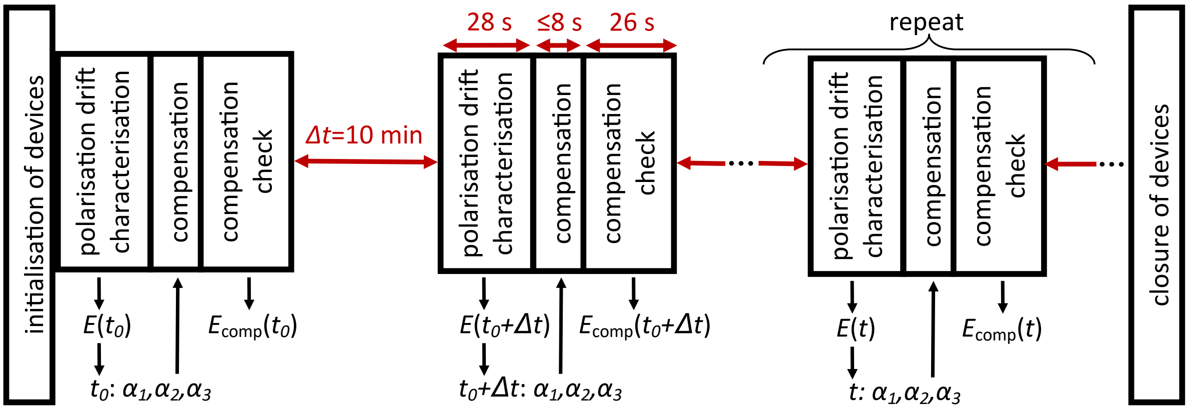

Figure 6.1: Temporal sequence for fibre polarisation drift compensation and checking the compensation. At the start, the devices (waveplates 1–5 and the polarimeter in the setup of Figure 4.2) are initialised and the client–server connection between the analysis PC in the Lanyon lab and the Mutters control PC is established. The devices and the connection are closed at the end of the sequence. Characterising the off-campus fibre path with respect to the change in polarisation induced by the fibre (labelled as polarisation drift characterisation) yields a Choi matrix, $E(t)$. The compensation angles $\alpha_1, \alpha_2, \alpha_3$ are determined from this Choi matrix and applied to waveplates 1–3 to compensate for the polarisation changes caused by the fibre. After the compensation, the combined system of the fibre and compensating waveplates (referred to as the compensated fibre) is characterised using waveplates 4 and 5. This check yields the Choi matrix $E_{\mathrm{comp}}(t)$ of the compensated fibre. The compensation check is not done in the experiment with ion-photon entangled states presented in Section 7.2. The first round of characterisation, compensation, and compensation check is labelled with the time t_0. The subsequent rounds follow with time intervals Δt of 10 minutes between each other.

The experimental sequence for polarisation drift compensation and checking the compensated fibre is shown in Figure 6.1 and is now described. Polarisation drift compensation starts with a polarisation drift characterisation, similar to the one described in Section 5.2, to obtain the Choi matrix that describes the process implemented by the fibre on the polarisation of light travelling through it. The fibre characterisation with respect to the change in polarisation of light sent through the fibre is called polarisation drift characterisation from now on. The polarisation drift characterisation starts with the preparation of the input states $|H\rangle$, $|V\rangle$, $|D\rangle$, $|A\rangle$, $|R\rangle$ and $|L\rangle$[75] using waveplates 1 and 2 (Figure 4.2). After the waveplates have finished rotating to prepare each input state, there is a one-second wait time, after which the polarimeter is read out. Overall,

---

[75] The sequence of input states is different from the sequence in Section 5.2 because the focus lies on the compensation rather than on the maximal speed of state preparation. The sequence of input states can be changed deliberately.

the characterisation of the Choi matrix $E(t)$ takes 28 seconds, which is dominated by the time needed to rotate the waveplates. The time needed for the determination of $E(t)$ is higher than the time presented earlier in Section 5.2, because a different sequence of input states is chosen to match the code used for process tomography and avoid data reshuffling. Therefore, the change in the waveplate angles between consecutive input states is larger. For example, it takes longer to rotate from $|H\rangle$ to $|V\rangle$ than to rotate from $|H\rangle$ to $|D\rangle$.

The data are used to perform process tomography as described in Subsection 2.3.2. The eigenvector corresponding to the largest eigenvalue of the resulting 4×4 Choi matrix $E(t)$ is used to obtain a 2×2 matrix A. More details on the computation of A are given in Appendix A.5. The inverse of this matrix, A^{-1}, corresponds to the target matrix U_{target} that should be implemented by waveplates 1–3 of Figure 4.2 to compensate for the changes in polarisation caused by the fibre. Therefore, the process describing the waveplates 1-3 and the off-campus fibre path 1 should correspond to the identity such that the polarisation of light remains unchanged after passing through these optical elements. The target matrix is decomposed into the waveplate angles $\alpha_1(t)$, $\alpha_2(t)$ and $\alpha_3(t)$, as described in Subsection 2.2.3. Waveplates 1, 2 and 3 are then set to the angles α_1, α_2, α_3 found at time t, physically implementing the compensation with the unitary $U_{\text{QHQ}}(\alpha_1(t), \alpha_2(t), \alpha_3(t))$. Depending on how far the required waveplate angles are from the angles used for the last prepared input state $|L\rangle$, the compensation can take up to eight seconds.

Next, how well the fibre has been compensated is characterised using the two additional waveplates 4 and 5 (Figure 4.2). These waveplates are used to prepare the states $|H\rangle$, $|V\rangle$, $|D\rangle$, $|A\rangle$, $|R\rangle$ and $|L\rangle$ once more, while waveplates 1–3 (Figure 4.2) remain at the angles α_1, α_2, α_3 set in the last step. The characterisation of the compensation of the fibre is called the compensation check in Figure 6.1. A Choi matrix $E_{\text{comp}}(t)$, which describes the compensated fibre (i.e., the off-campus fibre and the waveplates used for the compensation), is obtained from the data. The compensation check takes 26 seconds[76].

After the compensation check, a ten-minute wait time is set, during which photons could be sent through the fibre. The polarisation drift characterisation, the compensation and the compensation check take less than one minute in total and are repeated 505 times with ten-minute intervals over almost four days.

6.2. Results of the periodic polarisation drift compensation

The polarisation drift compensation is performed as described in Section 6.1. The results of applying the polarisation drift compensation are now presented.

The data from the polarisation drift characterisation and compensation is shown in Figure 6.2. Overall, the observed polarisation drifts are similar to the drifts presented in Figure 5.2. However, in the data of Figure 6.2b, there is no clear jump visible in the fidelity

---

[76] The polarisation drift characterisation and the compensation check take slightly different times because there is a half-waveplate (HWP) followed by a quarter-waveplate (QWP) in the first case and a QWP followed by a HWP in the second case. The sequence of the waveplates determines the angles of the waveplate that have to be set, and therefore the time needed to rotate them.

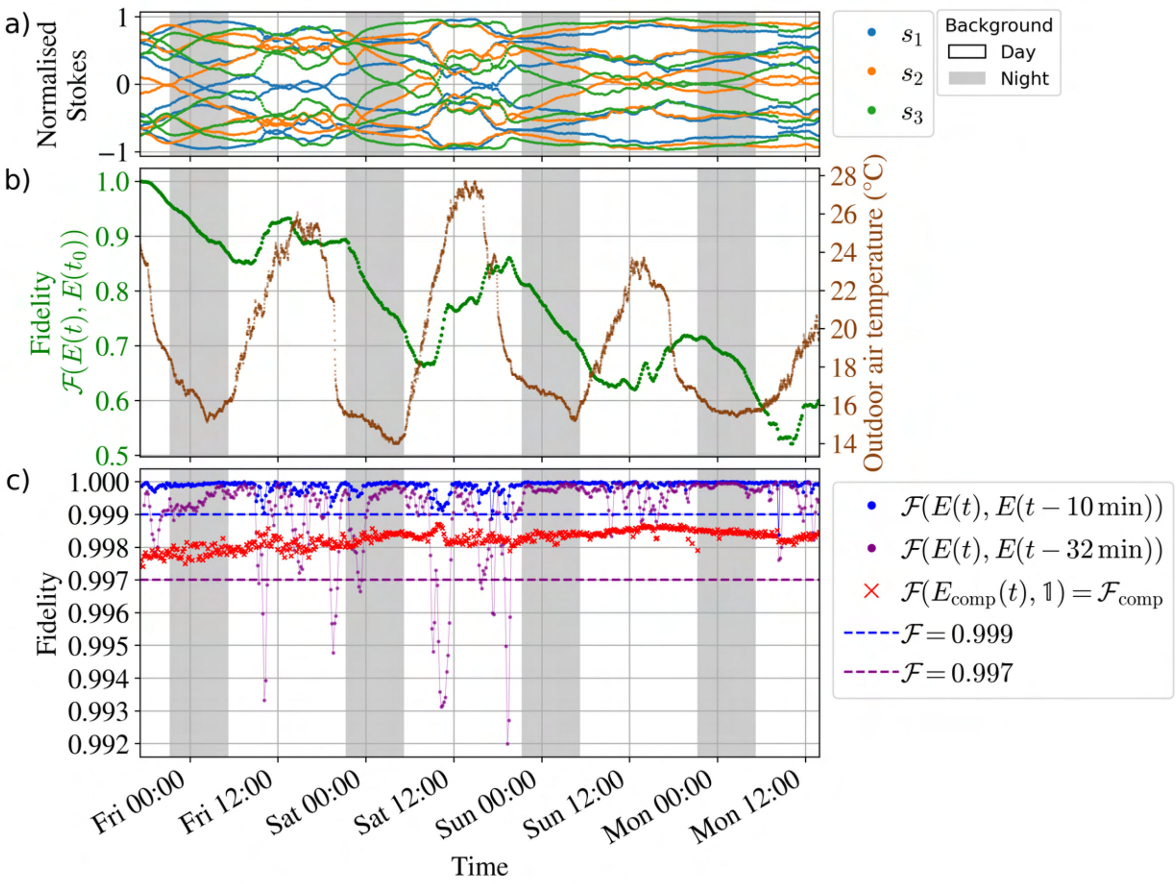

Figure 6.2: Polarisation drift and compensation in the off-campus fibre path 1. a) Stokes parameters over time for all six input states. b) Fidelity between the Choi matrices $E(t)$ and $E(t_0)$, and the outdoor air temperature measured in Schöpfstraße 45, Innsbruck, by Zentralanstalt für Meteorologie und Geodynamik in cooperation with the Department of Atmospheric and Cryospheric Sciences of the University of Innsbruck [90]. The fidelity shows how the process implemented by the fibre on polarised light would change over time if no polarisation drift compensation is performed. c) Fidelity between the Choi matrices $E(t)$ and $E(t-\Delta t)$ for a time difference Δt of ten and 32 minutes, and the fidelity with respect to the identity operation after compensation, $\mathcal{F}_{\mathrm{comp}} = \mathcal{F}(E_{\mathrm{comp}}(t), \mathbb{1})$, shown in red. Measurements taken from 06.06.2024 to 10.06.2024.

$\mathcal{F}(E(t), E(t_0))$, while there was a jump in the fidelity of Figure 5.2b. Figure 6.2c shows, alongside to the fidelities $\mathcal{F}(E(t), E(t-\Delta t))$, also the fidelity $\mathcal{F}_{\mathrm{comp}}$ of the compensated fibre with respect to the identity operation $\mathbb{1}$. The fidelity $\mathcal{F}_{\mathrm{comp}}$ is calculated using the Choi matrix obtained from the compensation check and was not presented in Figure 5.2. The fidelity $\mathcal{F}_{\mathrm{comp}}$ exhibits slight fluctuations over time but shows no significant drops compared to the fidelities $\mathcal{F}(E(t), E(t-\Delta t))$. The compensation of the off-campus fibre path 1 had a fidelity $\mathcal{F}_{\mathrm{comp}}$ with the identity operation above 0.997 over the entire measurement period of almost four days.

Ideally, $\mathcal{F}_{\mathrm{comp}}$ would be one, which is not the case. Converting the 2 × 2 matrix

$$B = AU_{\mathrm{QHQ}}(\alpha_1(t), \alpha_2(t), \alpha_3(t)), \tag{6.1}$$

which consists of the matrix A obtained from the Choi matrix $E(t)$ and the matrix determined by the set waveplate angles, into a Choi matrix[77] allows calculation of the fidelity of B with the identity operation using Equation (2.44). The resulting expected compensation fidelity is above 0.9999, which is higher than the measured compensation fidelity between 0.9974 and 0.9987 obtained through the compensation check. The discrepancy could be due to imperfections in the retardances and measured optical axes of the waveplates. Different retardances, either due to manufacturing error or the waveplate surfaces not being aligned perpendicular to the incoming beam, and limited knowledge of the optical axes (determined via a separate characterisation of the waveplates, see Appendix A.2) lead to imperfectly prepared states. The imperfectly prepared states influence the Choi matrices $E(t)$ and $E_{\mathrm{comp}}(t)$. Furthermore, imperfections in the retardance and the limited knowledge of the optical axes of the waveplates introduce errors in the implementation of $U_{\mathrm{QHQ}}(\alpha_1(t), \alpha_2(t), \alpha_3(t))$. Simulations show that an error of 1° in the knowledge of the optical axis of both a HWP and a QWP used to prepare the input states can result in a fidelity of the prepared state with respect to the target state as low as 0.988.

6.3. Conclusion

Polarisation drift compensation over the off-campus fibre 1 was performed, and checked, every ten minutes over a period of nearly four days. The checks performed immediately after the compensation each reveal a process fidelity of the compensated fibre between 0.9974 and 0.9987 with respect to the ideal process corresponding to the identity. This imperfection in our ability to compensate for changes in polarisation induced by the fibre may be due to inaccuracies in the waveplates' retardances or misalignment of their optical axes. Therefore, to improve the compensation, more accurate characterisations of the used waveplates are required. Polarisation drift compensation took approximately half a minute. Altogether, the polarisation drift compensation and checking of how well the compensation worked took approximately a minute. The majority of the time is used to rotate waveplates. Therefore, the speed of the polarisation drift compensation and check is limited by the rotation speed of the motorised waveplate stages. The time used for the polarisation drift compensation and the compensation check is one tenth of the ten-minute intervals, which could be used to perform experiments with single photons. Within each ten-minute interval, polarisation drifts were always smaller than the compensation error. Polarisation drifts over half an hour, extracted from the same data set, were below the process fidelity of the compensated fibre in 7 % of the cases. Therefore, applying compensation more often than every half hour is generally not expected to provide a significant advantage compared to not applying any compensation.

---

[77] The conversion of a Kraus matrix into a Choi matrix is performed in Python using the function *kraus2choi* from the project *Forest Benchmarking - operator tools - superoperator transformations* [94].

Nevertheless, monitoring the polarisation drift over these time intervals provides insight into how much drift occurred in the off-campus fibre, and reveals the rare events in which there was a significant polarisation drift. For example, if the polarisation drift over such a time interval is significant, then discarding measurements involving ion-entangled photons taken during the time interval might be considered. The compensation becomes relevant for longer-duration experiments using the off-campus fibre.

7. Polarised photons and ion-photon entanglement over the off-campus fibre

So far, polarisation drifts in the off-campus fibre path and their compensation using laser light have been discussed. Here, the discussion focuses on sending single photons emitted by an ion through the off-campus fibre. One of the goals of this chapter is to determine whether the polarisation state of photons remains stable over time when polarisation drift compensation is performed at roughly periodic intervals on the fibre (Section 7.1). Another goal of this chapter is to establish ion-photon entanglement over the 17 km-long off-campus fibre path (Section 7.2).

Dr. Viktor Krutianskii took the lead on running the ion trap and overall coordination of the data-taking. PhD student Armin Winkler was responsible for operating the quantum frequency conversion (QFC) setups. Dr. Fabitha Kodakkat was responsible for the Mutters photon detection station. I was responsible for the polarisation drift compensation.

7.1. Distribution of polarised single photons

This section presents an experiment in which polarised photons, emitted from the ion, are converted to 1550 nm, transmitted through the off-campus fibre path, and analysed in polarisation at the Mutters photon detection station. The used off-campus fibre path is the off-campus fibre path 2 (shown in Figure 4.1), while for the measurements presented in Chapter 6, off-campus fibre path 1 was used. The experimental results presented in this section were obtained on November 29th 2024, including polarisation drift compensation (with compensation checks) performed at approximately regular intervals.

Setup. The setup used for acquiring the data in this section is shown in Figure 4.1. A single ion is trapped. On the endcaps of the ion trap, voltages of 1011 V and 1000 V are applied. QFC Setup 1 (see Subsection 3.2.1) is used to convert the 854 nm photons to 1550 nm, but only one of the two periodically poled lithium niobate (PPLN) crystals is temperature stabilised[78], which means that only one polarisation is converted. Waveplates are used to approximately match the polarisation of the photons to the polarisation that can be converted. The Toptica 1550 nm laser is used for the polarisation drift compensation setup.

Calibrations. The calibrations and adjustments made before generating and measuring single photons are described in the following paragraph. The QFC Setup 1 was optimised and characterised using $P_{854} = 8(1)\,\mathrm{mW}$ of input laser light at a wavelength of $\lambda_{\mathrm{in}} = 854\,\mathrm{nm}$ (measured before the input of the fibre connected to the beginning of the QFC setup) instead of single photons. The 1902 nm pump laser for the QFC is set to a power of $P_{1902} = 500(5)\,\mathrm{mW}$ and tuned in frequency such that the fraction of light converted from 854 nm to 1550 nm is maximal. A power of $P_{1550} = 510(5)\,\mu\mathrm{W}$ of converted light at a wavelength of $\lambda_{\mathrm{out}} = 1550\,\mathrm{nm}$ is fibre-coupled at the output of the

---

[78] The Peltier element regulating the temperature of the second PPLN crystal was broken at the time and could not be used.

QFC setup. The given uncertainties are based on the precision of the values written in the lab book and the observed fluctuations. The fibre-coupled photon conversion efficiency is

$$\frac{P_{1550}}{P_{854}}\frac{\lambda_{\mathrm{out}}}{\lambda_{\mathrm{in}}} = 0.116(15). \tag{7.1}$$

To monitor the frequency of the 1902 nm pump laser, the fraction of the frequency-doubled pump light coming out of the second PPLN crystal is measured with a wavemeter. Furthermore, before running the experiment, the temperature of the fibre Bragg grating (FBG) at the Mutters photon detection station is tuned such that the transmission of 854 nm laser light converted to 1550 nm is maximal.

Pulse sequence. The laser pulse sequence for the state preparation of the trapped ion and the generation of single photons is described in this paragraph and shown graphically in Figure 7.1. First, Doppler cooling is implemented with the 397 nm laser, while the 866 nm and 854 nm lasers are also applied to the ion. Then, a 393 nm initialisation pulse is used for intensity stabilisation of the 393 nm Raman laser. This is followed by another Doppler cooling pulse to prepare the ion's motional state, and optical pumping to prepare its electronic state (Subsection 3.1.2). A loop with 20 iterations is then started to attempt to generate single photons. Each iteration begins with laser pulses at 854 nm and 866 nm to empty the $3^2\mathrm{D}_{5/2}$ and $3^2\mathrm{D}_{3/2}$ manifolds following previous iterations, along with additional optical pumping using the 397 nm laser. Next, a monochromatic 50 µs-long 393 nm Raman laser pulse attempts to generate a photon from the ion via the monochromatic cavity-mediated Raman transition (CMRT) (see Subsection 3.1.3). The iterations are repeated 20 times, resulting in 20 photon generation attempts. The loop is followed by a fluorescence measurement of the ion using the photo-multiplier tube (PMT). The entire laser pulse sequence described in this paragraph is repeated at least 51×100 times (in two cases, it was repeated 102×100 times) for a given setting of the waveplate angles at the Mutters photon detection station. For the data analysis, the first $51 \times 100 = 5100$ repetitions of the pulse sequence, each containing 20 attempts to generate a photon, are considered. The measurement of the ion state is not relevant in this section. Photon detection events at the Mutters photon detection station are sent back, via off-campus fibre path 1, to the timetagger in the Lanyon lab. The timetagger also records markers generated by the pulse box (Subsection 3.1.1) signalling the time at which a Raman laser pulse was triggered and then, after the 20 µs delay for the acousto-optic deflector (AOD), sent onto the ion.

The measurements of the photons with the two photon detectors at Mutters are described by observables with the eigenstates H/V, V/H, D/A, A/D, R/L, L/R. The normalised Stokes vector can be reconstructed from these measurements. This reconstruction is unaffected by differences in detector efficiency, as each polarisation basis is measured symmetrically in both orders (e.g., H/V and V/H). For each observable, there are 102000 attempts to generate a photon. This ensemble of measurements enables the reconstruction of the normalised Stokes vector of the photons, and is referred to as a measurement run.

Several measurement runs, each taking approximately seven minutes, are alternated with polarisation drift compensation runs. A polarisation drift compensation run,

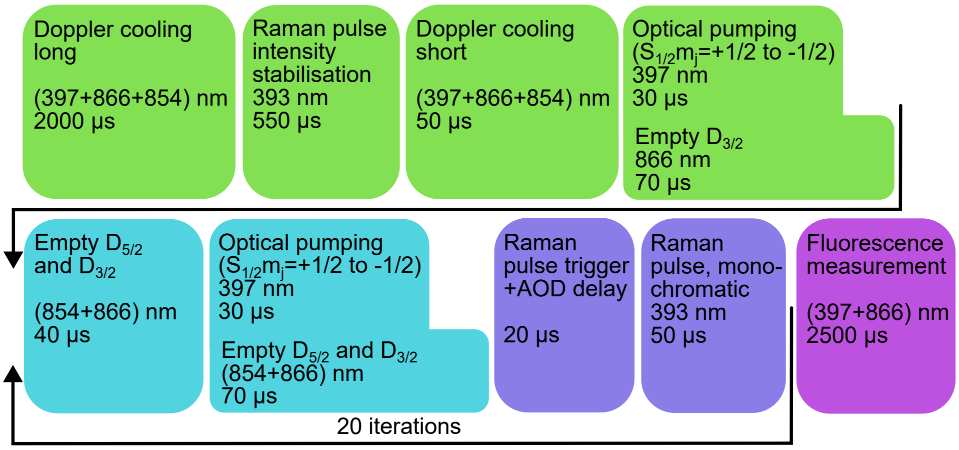

Figure 7.1: Pulse sequence for the polarised photon distribution experiment. The pulse sequence begins with a Doppler cooling pulse (green), followed by a Raman pulse to stabilise the intensity of the 393 nm Raman laser, a short Doppler cooling pulse, and optical pumping from the $4^2S_{1/2}, m_j = 1/2$ state to the $4^2S_{1/2}, m_j = -1/2$ state, applied in parallel with an 866 nm pulse to empty the $3^2D_{3/2}$ manifold. The sequence continues with a loop. Each iteration of the loop starts with further optical pumping and 866 nm and 854 nm pulses to empty the $3^2D_{3/2}$ and $3^2D_{5/2}$ manifolds (light blue). Next, a trigger initialises a Raman pulse (dark blue), which includes a delay of 20 µs for the acoustic wave in an AOD to reach the spot on which the 393 nm Raman laser beam passes, such that the laser beam is deflected. Then, a 50 µs-long monochromatic Raman pulse (also shown in dark blue) is applied to the ion in an attempt to generate a single photon. The iteration is then repeated. In total, the iteration of the loop is executed 20 times. The sequence concludes with the detection of the ion (purple). The entire pulse sequence is repeated 51 × 100 times. The widths of the boxes representing the pulses and detection times are not to scale with the actual durations.

including the compensation check, takes approximately one minute. A list of instructions and recommendations for running polarisation drift compensation, as configured in this chapter, can be found in the Appendix A.6. In total, eight measurement runs are performed over approximately 80 minutes, allowing the Stokes vector of the single photons to be determined eight times. In addition to measurement runs and polarisation drift compensation, other checks and adjustments are carried out during the 80 minutes. An overview of the actions taken and their timing is shown in Appendix Figure A.10.

The polarisation drift compensation results, including the polarisation drift characterisation and the compensation check, are shown in Figure 7.2. The procedure for polarisation drift compensation (and the compensation check) is similar to the procedure presented in Section 6.1, with only two minor differences. The first difference is that here, for each state of polarised light sent into the fibre, the output state is measured consecutively ten times (within 0.6 seconds) and then averaged, while in Sections 5.2 and 6.1 the output state was measured only once. The second difference is that the sequence of input states prepared is $|H\rangle$, $|A\rangle$, $|R\rangle$, $|V\rangle$, $|L\rangle$ and $|D\rangle$, reducing the time

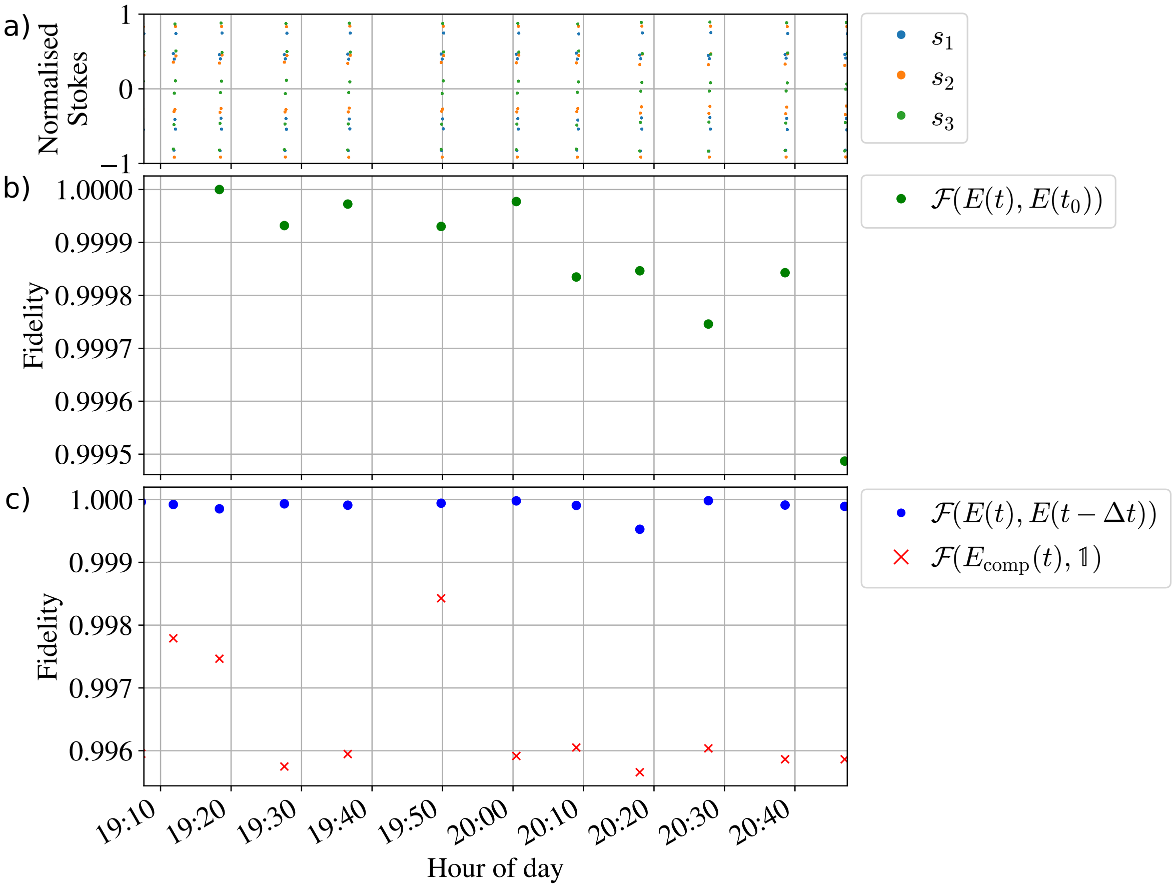

Figure 7.2: Polarisation drift compensation measurements on the day of the experiment involving polarised photons. a) Stokes parameters from the polarisation drift characterisation, obtained by performing measurements with laser light. b) Fidelities (Equation (2.44)) between Choi matrices E, determined through the polarisation drift characterisation, at times t and an initial time t_0. The initial time t_0 is chosen to be the last polarisation drift compensation measurement before the first measurement run with 1550 nm photons at the Mutters photon detection station at 19:20. c) Fidelity of the Choi matrices describing the process implemented by the fibre $E(t)$ with respect to the previous one $E(t-\Delta t)$ (blue) and fidelity between the Choi matrix describing the compensated fibre $E_{\text{comp}}(t)$ and the identity operation (red). The time difference Δt is the time elapsed from the previous polarisation drift compensation. The Choi matrices $E_{\text{comp}}(t)$ are obtained from the compensation checks and describe the process on polarised light implemented by the compensated off-campus fibre path.

needed to rotate the waveplates for state preparation compared to Section 6.1. The polarisation drift of the light sent through the off-campus fibre path was insignificant over the data-taking period. Specifically, the fidelity between the Choi matrices describing the process of the fibre was never less than 0.9995 (Figure 7.2b). This fidelity is higher than the fidelities between 0.995 and 0.999 of the compensation checks (Figure 7.2c).

Therefore, the polarisation of photons transmitted through the off-campus fibre path is expected to remain stable over the 80-minute measurement period even in the absence of polarisation drift compensation.

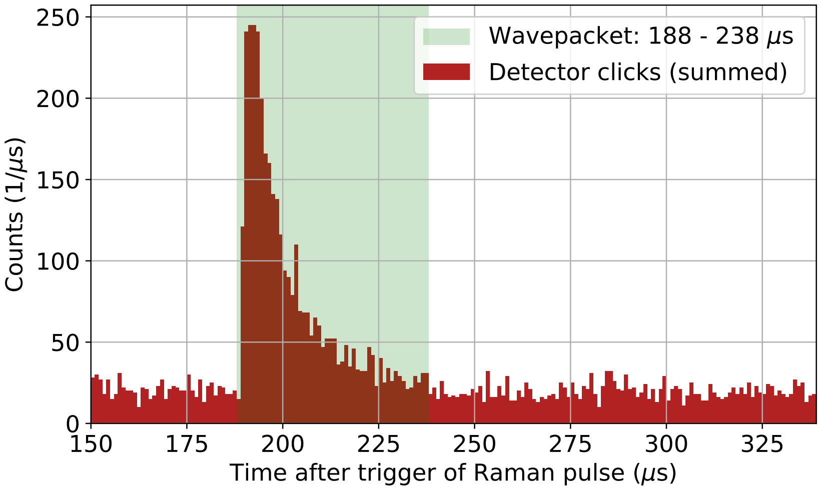

Figure 7.3: Polarised photons detected at the Mutters photon detection station. The shown histogram is the sum over all eight measurement runs of the polarised 1550 nm photons. The photon wavepacket is highlighted with a green background, corresponding in length to the 50 µs Raman pulse.

The code used to evaluate the photon detection events is a modified version of a code written by PhD student Marco Canteri. The analysed data consists of a file in which, amongst others, the times of the Raman pulse trigger and the photon detection events registered by the time-tagger are listed. Summing the photon detection events from 150 µs to 339 µs after the triggers signalling the start of the Raman pulses, for all eight measurement runs, results in the histogram shown in Figure 7.3. The histogram shows the detected photon wavepacket with a duration of $T_{\text{wp}} = 50\,\mu\text{s}$ that starts at 188 µs after the Raman pulse trigger. This delay between the Raman trigger and the start of the wavepacket is dominated by the time the photon takes to travel through the off-campus fibre path 2 (82 µs, assuming the refractive index of the fibre path to be 1.4620 [95]), as well as the time required for the detector signal at the Mutters photon detection station to reach the time-tagger in the Lanyon lab via the off-campus fibre path 1 (this time is the same as the photon travel time in off-campus fibre path 2, as both fibre paths have the same length). Furthermore, there is the AOD delay of 20 µs. So, the start of the wavepacket would be expected 184 µs after the Raman trigger. The expected start of the wavepacket is 4 µs earlier than the wavepacket highlighted in Figure 7.3. The light travel time through the additional fibres within the Lanyon lab and the Mutters photon detection station, and the processing and transmission of electrical signals, can explain only a fraction of the deviation. The origin of the rest of the deviation is not known. The wavepacket contains a total of $N_{\text{wp}} = 3772$ counts. Taking the mean of the counts registered in the plotted range excluding the wavepacket, the average background is $N_{\mathrm{bg}} = 19.9(4)$ counts per microsecond time bin (this value is for the summation of all the attempts to generate a photon), where the uncertainty given is the standard error in the mean. The average number of background photons taking into account the 4896000 attempts is 4.07(9) counts per second (cps). This value is significantly higher than the average background of 1.209(4) cps measured at the end of the off-campus fibre path 1 when the input of the fibre path is capped (as reported at the end of Section 5.1). The increase in background counts is likely due to noise photons coupled into the fibre path in the Lanyon lab.

The signal-to-noise ratio is estimated from the ratio of the expected number of photon counts in the wavepacket, when excluding background counts, to the number of background counts [96]. The signal-to-noise ratio is therefore

$$\frac{N_{\mathrm{wp}}/T_{\mathrm{wp}} - N_{\mathrm{bg}}}{N_{\mathrm{bg}}} = 2.79(10). \tag{7.2}$$

The efficiency is calculated as the ratio of the expected number of photon counts in the wavepacket when excluding background counts to the number of attempts. The total efficiency of the eight measurement runs is $5.67(13) \cdot 10^{-4}$ ($7.70(13) \cdot 10^{-4}$ without background subtraction). The error is estimated by assuming Poisson statistics on the photon counts. The background subtracted efficiencies of each of the eight measurement runs range from $0.38(3) \cdot 10^{-3}$ to $0.70(4) \cdot 10^{-3}$ and are shown together with the probability of detecting a photon (including background photons) in Figure 7.4a. After the measurement run with the lowest efficiency (fifth measurement run for 1550 nm photons at the Mutters photon detection station), the frequency of the 1902 nm QFC laser was optimised to maximise the efficiency of the QFC (see Appendix Figure A.10). The maximisation is done indirectly by maximising the photon rate at the Mutters photon detection station when attenuated 854 nm laser light is sent into the same path followed by the 854 nm photons emerging from the vacuum chamber. The measurement runs taken after optimising the 1902 nm QFC laser frequency have efficiencies above $0.6 \cdot 10^{-3}$. A more detailed discussion of the expected efficiencies is given in Section 7.2.

The normalised Stokes parameters s_1, s_2, s_3 of the photons are calculated using Equation (2.32), where N_{H} and N_{V} are obtained by summing the opposite detectors' clicks for the measurements in the H/V and V/H setting (corresponding to the eigenstates of the observables describing the measurements). Summing over these two measurement bases in this way makes the resulting Stokes parameter independent of differences in the efficiencies of the two superconducting nanowire single photon detector (SNSPD)s. Similarly, N_{D} and N_{A} (N_{R} and N_{L}) are obtained by summing the measurements in the D/A and A/D (R/L and L/R) setting. The detector clicks due to background are not subtracted from the total detector clicks. The normalised Stokes parameters of the photons for the eight measurement runs are shown in Figure 7.4b.

From the normalised Stokes parameters, the density matrices $\rho(t)$ are calculated using state tomography as described in Subsection 2.3.1 for a single qubit encoded into the polarisation of the photon. The fidelities of the obtained density matrices with respect to the density matrix of the first measurement run are calculated using Equation (2.44), denoted as $\mathcal{F}(\rho(t),\rho_0)$ and shown in Figure 7.4c. The error bars are obtained using a

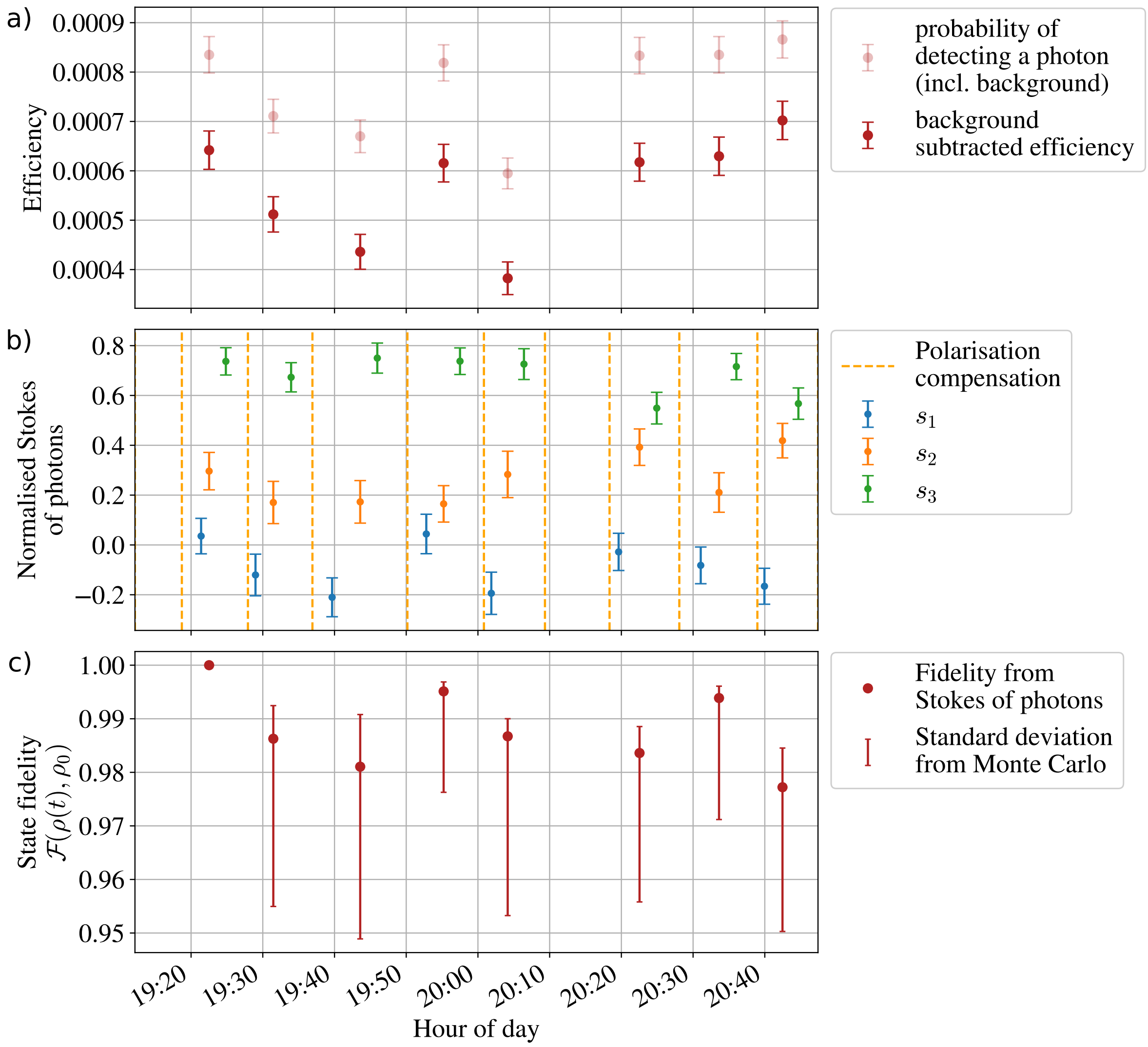

Figure 7.4: Efficiency, Stokes parameters, and polarisation state fidelities of the polarised 1550 nm photons measured at the Mutters photon detection station. a) Efficiency of the photons, calculated as the ratio of the number of photon detection events in the wavepacket (total number of counts minus the number of background counts) of each of the eight measurement runs to the number of attempts. For comparison, the probability of detecting any photon (either a photon emitted from the ion or a background photon) is plotted in light red. b) Stokes parameters of the photons. Each measurement run consisted of photon polarisation analysis in six bases, yielding three Stokes parameters as described in Subsection 2.2.2. c) Fidelity between the density matrices $\rho(t)$ and the density matrix of the first measurement run, ρ_0. The density matrices are obtained via state tomography. The errors on the fidelity are obtained by Monte Carlo simulation, and the shown error bars are centred around the mean of the Monte Carlo (MC) samples.

statistical method called MC simulation [97, 98]: for each measured Stokes parameter, 100 samples of Stokes parameters are generated from a normal distribution with the centre value given by the Stokes parameter and a standard deviation given by the error bar on the Stokes parameter. These samples are used to generate 100 density matrices for each measurement run, from which the fidelities are calculated. The standard deviation of the ensemble of 100 fidelities with respect to the mean of the MC sample is used as the error. Since the mean of the MC sample does not correspond to the fidelity obtained from the measurement, the error bar in Figure 7.4c is asymmetric around the fidelity obtained from the measurement. While the first fidelity is 1 (by definition), the other fidelities agree within the shown error bars. The lowest recorded fidelity is $0.977^{+0.005}_{-0.031}$.

7.2. Ion-photon entanglement between an ion at the Technik campus and a photon at the Mutters photon detection station

The final goal of this thesis is to measure entanglement between an ion in the Lanyon lab and a photon sent through an off-campus fibre to the Mutters photon detection station. Ion-photon entanglement can serve as a basis for other experiments, such as the quantum repeater node experiment presented in Ref. [24]. The experimental results presented in this section were obtained on December 20th 2024.

Setup. The setup used to obtain the data in this section is shown in Figure 4.1, but without the waveplates 4 (half-waveplate (HWP)) and 5 (quarter-waveplate (QWP)). Off-campus fibre path 2 is used to send photons from the Lanyon lab to the Mutters photon detection station. The endcap voltages and the trap confinement are the same as in the experiment presented in Section 7.1. The QFC Setup 2 described in Subsection 3.2.2 is used to convert the 854 nm photons to 1550 nm while preserving their polarisation. Polarisation preserving means that rotating the 854 nm waveplates (QWP and HWP) at the input of QFC Setup 2 does not influence the converted 1550 nm power measured at the output (or, at least, the influence is lower than the existing fluctuations). The reasons for the absence of the two waveplates 4 and 5 are that in this experiment, the polarisation drift compensation is not checked, and that the available space at the end of the QFC Setup 2 is limited. The optical elements for the polarisation drift compensation setup were moved from QFC Setup 1 to QFC Setup 2. The Toptica 1550 nm laser is used for polarisation drift compensation. The laser light is manually blocked at the output of the laser after each polarisation drift compensation run, as it was observed to increase the number of background photons measured at the Mutters photon detection station. The increase in background photons was not observed in the experiment involving polarised photons presented in Section 7.1 using QFC Setup 1. A possible explanation is that, when the flip mirror is down (not reflecting the laser light into the off-campus fibre path), there is more scattering of the laser light in QFC Setup 2 than in QFC Setup 1. For further experiments using the polarisation drift compensation setup in combination with QFC Setup 2, it may be useful to set up another shutter to avoid the necessity of manually blocking the laser light after each polarisation drift compensation run.

Calibrations. The calibrations that were performed before distributing single photons will now shortly be described. QFC Setup 2 was optimised and characterised using laser light at 854 nm instead of single photons. The 854 nm power measured in front of the input fibre of QFC Setup 2 is 1.560(10) mW. The 1902 nm pump laser for the QFC is set to a power of 500(5) mW and tuned in frequency such that the fraction of light converted from 854 nm to 1550 nm is maximised. A power of 0.184(5) mW of converted 1550 nm light is fibre-coupled at the output of the QFC setup. Therefore, the fibre-coupled photon conversion efficiency is 0.214(6). In parallel, around 300 mW of the 1902 nm pump light is sent to QFC Setup 1 so that the frequency of the frequency-doubled 1902 nm light after the PPLN crystals can be monitored. Finally, the temperature of the FBG at the Mutters photon detection station is tuned such that the transmission of 854 nm laser light converted to 1550 nm is maximal.

Pulse sequence. The laser pulse sequence for the state preparation of the trapped ion, the generation of ion-entangled photons and the measurement of the electronic state of the ion is described in this paragraph and shown in Figure 7.5. Assuming that the time for the photons to travel through the off-campus fibre and for the detector signal to be sent back and time-tagged is $2 \times 82\,\mu s$ (assuming the refractive index of the off-campus fibre paths to be 1.4620 [95]), and that the photon is generated within the 50 µs of the Raman pulse, then the time-tag of the photon is expected to be between 164 µs and 214 µs after the start of the Raman pulse. The photon detection time window from 145 µs to 260 µs after the start of the Raman pulse is chosen to be larger than this time to allow photons to be detected also outside of this time window (for example, there are additional delays due to processing of the signals, additional fibres in the Lanyon lab and the Mutters photon detection station). The key differences from the pulse sequence for polarised photon distribution, shown in Figure 7.1, are that the Raman pulse is now bichromatic and that there is now sequence branching conditional on the detection of a photon. Specifically, if there is a detector click in the 115 µs photon detection time window, the loop is aborted and the ion-qubit state is measured. If there is no detector click within the photon detection time window, the next iteration of the loop (and photon distribution attempt) is executed. Up to ten iterations are executed consecutively within a loop. For a given set of waveplate angles at the Mutters photon detection station, the entire pulse sequence described in this paragraph is repeated 121 × 100 times. Within these repetitions, the ion is measured in different bases (σ_1, σ_2, and σ_3) while the photon measurement basis stays the same.

Sufficient information for ion-photon state tomography can be obtained by repeating the procedure with different measurement bases for the photons. The measurement bases for the photons are set by the waveplates at the Mutters photon detection station. Specifically, the waveplate angles are set in such a way that the photons are measured in the bases defined by the eigenstates of the projective measurements: H/V, V/H, D/A, A/D, R/L, and L/R. Combined with the iterations of the ion measurement bases, a total of 6×3 two-qubit measurement combinations are acquired and used for state tomography (Subsection 2.3.1). Such a measurement run, including all measurement combinations, takes approximately fifteen minutes. As in Section 7.1, the measurement runs are alternated with polarisation drift compensation runs. Specifically, polarisation drift

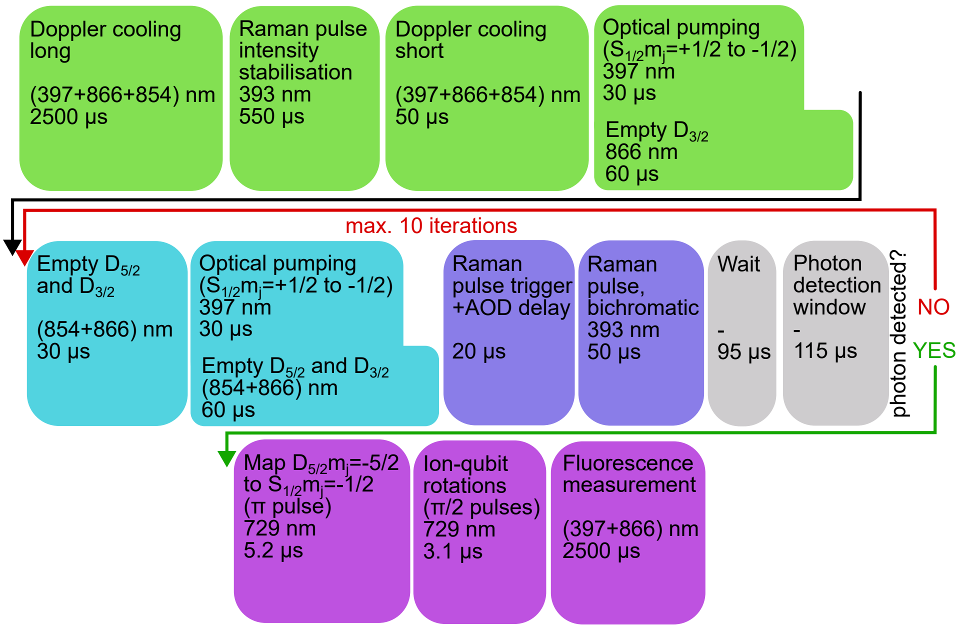

Figure 7.5: Pulse sequence for the ion-photon entanglement experiment. The pulse sequence is, apart from some differences in pulse lengths, similar to that presented in Figure 7.1. However, the Raman pulse used to generate photons is bichromatic here. A key difference lies in the branching at the end of each iteration: if a photon is detected within the 115 µs photon detection window, the ion-qubit state is measured (purple); otherwise, the loop is repeated, up to a maximum of ten times. The photon detection window starts 165 µs after the Raman pulse trigger and ends 280 µs after the Raman pulse trigger. The ion-qubit measurement comprises π and $\pi/2$ pulses (to change the observable in which the ion is measured) followed by a fluorescence measurement. The entire sequence is repeated in total 121 × 100 times.

compensation consists of a polarisation drift characterisation followed by compensation with three waveplates. Each such compensation takes approximately half a minute. There is no compensation check.

Experiments with single photons begin by performing measurements of the trapped ion and the ion-entangled 854 nm photons in the Lanyon lab. These measurements are performed by connecting the fibre, into which the photons are coupled, to a polarisation analysis setup instead of joining it with the input fibre of the QFC setup. The polarisation of the photons is characterised using an 854 nm polarisation analysis and SNSPD detector setup, as described in the upcoming PhD theses of James Bate and of Marco Canteri. The obtained data is used in this thesis to estimate the efficiency of the 854 nm in the Lanyon lab and to have a comparison of the fidelity of the ion-photon state with an ideal Bell state. The efficiency and fidelity of the last performed measurement involving 854 nm photons are given below. Next, the full experiment is performed, and ion-entangled 1550 nm photons are sent to the Mutters photon detection station. In total, eight attempts to measure remote ion-photon entanglement were made. In two cases (specifically the first and fifth attempts), reading out some of the measurement files resulted in an error. Therefore, these measurements are not taken into account in the following analysis. The fourth out of the eight measurement runs had a melting event (i.e., the ion gained energy, for example, due to a collision with another atom or molecule in the vacuum chamber), identified by a blurred image of the ion on the camera. However, the measurement run is still considered *successful* because the files can be read out. The six measurement runs considered in the following analysis were taken over approximately two and a half hours. Over the two and a half hours, a range of different checks and adjustments are performed, which are summarised in Appendix Figure A.11.

The results of the polarisation drift compensation runs performed immediately before, during and after the remote 1550 nm entanglement measurements are shown in Figure 7.6. A total of ten polarisation drift characterisations, which were taken during the two and a half hours, are considered in the following analysis. The characterised process fidelity with the initial process drops to only 0.9986 (Figure 7.6b). The lowest fidelity between sequential processes is on the order of 0.9999 (Figure 7.6c).

The wavepacket of the remote 1550 nm photons measured at the Mutters photon detection station, summed over the six successful measurement runs, is shown in Figure 7.7. The wavepacket contains a total of 4693 counts. Taking the mean of the counts registered in the range plotted in Figure 7.7 except for the wavepacket range, the average background is 9.22(17) counts per microsecond (this value is for the summation of all the attempts to generate a photon), where the uncertainty given is the standard error in the mean. The time-tagger registered a total of 4333267 attempts to distribute ion-entangled photons. When performing the pulse sequence, the average photon generation attempt rate is 835(7) Hz. Considering only the photon's travel time through the off-campus fibre and the return time of the photon detection signal to the Lanyon lab, the attempt rate would be limited to 6.1 kHz. Therefore, the photon generation attempt rate could maximally be seven times higher. The average number of background photons taking into account the number of attempts is 2.13(4) cps, which is about half of the average background reported in Section 7.1. A possible reason for the decrease in average background is the use of different filters in QFC Setup 2 compared to the filters of QFC Setup 1.

The signal-to-noise ratio is 9.2(2). The signal-to-noise ratio is almost three times higher than in the experiment presented in Section 7.1. One reason is the higher efficiency of the QFC Setup 2 (0.21) compared to QFC Setup 1 (0.12 fibre-coupled photon conversion efficiency). Another reason is the lower average background (2.13(4) cps per attempt compared to 4.06(9) cps per attempt) observed in the wavepacket sum of all successful measurement runs.

The total efficiency of the sum of the six successful measurement runs is $0.977(16) \cdot 10^{-3}$ ($1.083(16) \cdot 10^{-3}$ without background subtraction), which is higher than the total efficiency reported in Section 7.1. The main reason for the improved efficiency is the higher efficiency of the QFC. Multiplying the total efficiency by the average photon generation attempt rate results in an average photon detection rate of 0.815(13) Hz. The efficiencies of the individual six successful measurement runs of the ion-entangled remote 1550 nm photons range from $0.86(4) \cdot 10^{-3}$ to $1.04(4) \cdot 10^{-3}$ and are shown in Figure 7.8a. To estimate the expected efficiency of the ion-entangled 1550 nm photons at the Mutters photon detection

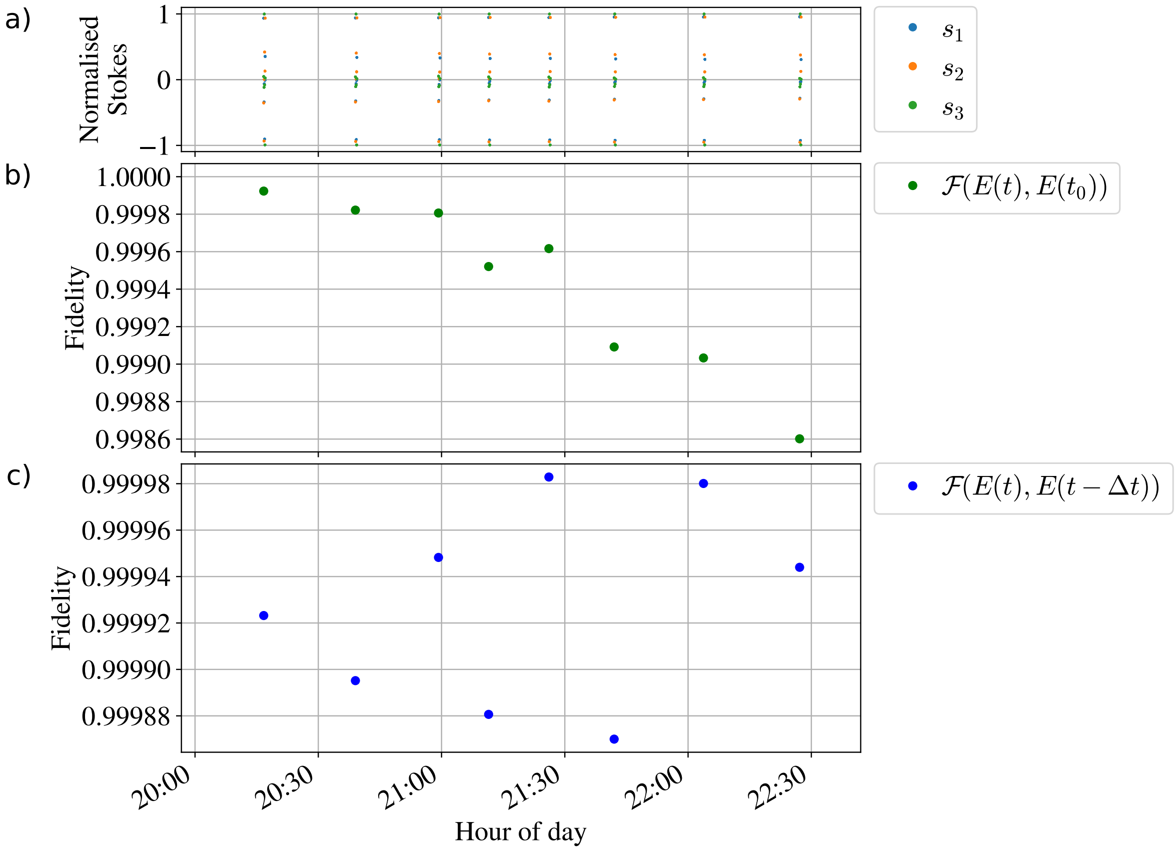

Figure 7.6: Polarisation drift compensation measurements on the day of the experiment involving ion-photon entanglement. a) Stokes parameters from the polarisation drift characterisation, obtained by performing measurements with laser light. b) Fidelities between Choi matrices E, determined through the polarisation drift characterisation, at times t and an initial time t_0. The time t_0 is chosen to be the last polarisation drift compensation measurement before the first ion-photon measurement. The fidelity shows how the process implemented by the fibre on polarised light would have changed if there had been no polarisation drift compensation. c) Fidelity of the Choi matrices describing the process implemented by the fibre $E(t)$ with respect to the previous one $E(t - \Delta t)$ (blue). The time difference Δt is the time elapsed from the previous polarisation drift compensation.

station, the last measurement of 854 nm ion-entangled photons in the Lanyon lab is taken as the starting value, and the known efficiencies of other components along the path of the 1550 nm photons to the Mutters photon detection station are taken into account. An overview is given in Table 7.1. The measured background-subtracted efficiencies of the 1550 nm ion-entangled photons at the Mutters photon detection station are lower than the expected efficiency given in Table 7.1, ranging from 74(6) % to 90(7) % of the expected value across the six measurements. One possible reason for the lower measured efficiency is that the efficiency of some components measured separately (in most cases,

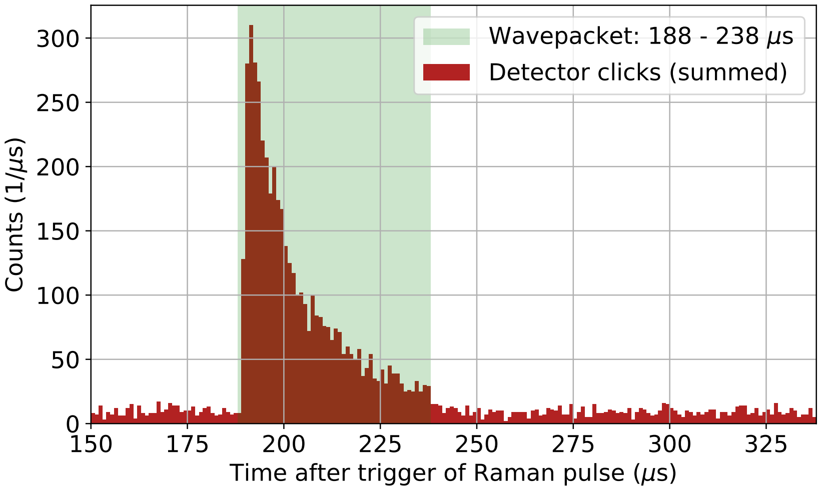

Figure 7.7: Ion-entangled photons detected at the Mutters photon detection station. The shown histogram is the sum over six successful measurement runs of the 1550 nm ion-entangled photons. The photon wavepacket is highlighted with a green background, which has the same length as the Raman pulse of 50 µs.

on a different day from the ion-photon entanglement) may vary from those on the day and time of the experiment with ion-entangled photons. For example, misalignment of a polarisation analysis board would affect the efficiency. Another possible reason is that the used fibre joiners and patch fibres (not taken into account in the calculation given in Table 7.1) significantly affect the measured efficiency. Fluctuations in the measured efficiencies of the 1550 nm ion-entangled photons can also arise due to drifts in the frequency of the 1902 nm pump laser for the QFC, and due to drifts in power or frequency of the Raman laser.

State reconstruction is performed on the data obtained from the measurements of the ion and the photons, resulting in a density matrix describing the ion-photon state (see state tomography in Subsection 2.3.1). The obtained density matrix is numerically rotated by single qubit unitary operations so that it approaches the ideal Bell state $\rho_{|\Phi^+\rangle}$ written out in Equation (2.6). The rotated reconstructed density matrix of the ion-photon state is denoted as $\rho_{\mathrm{ip}}(t)$. The goal of the rotation is to enable a comparison of the density matrix describing the ion-photon state with the ideal Bell state $\rho_{|\Phi^+\rangle}$. The rotation is necessary since the photon is sent through fibres and optical elements outside of the compensated fibre path that can rotate the photon state on the Poincaré sphere. As long as it is a single qubit unitary rotation and stable throughout the measurements in all bases, the rotation does not affect the entanglement of the ion-photon state.

The Python code used for the analysis of the ion-photon states is provided by PhD student James Bate[79] and adapted in terms of detection times and fluorescence detection thresholds to analyse the data of the performed experiment. The fidelity of the recon-

---

[79] The Python code is based on a code written by Thomas Monz in 2009, which was adapted and cleaned for the Quantum Interfaces Group by Dr. Simon Baier in 2021.

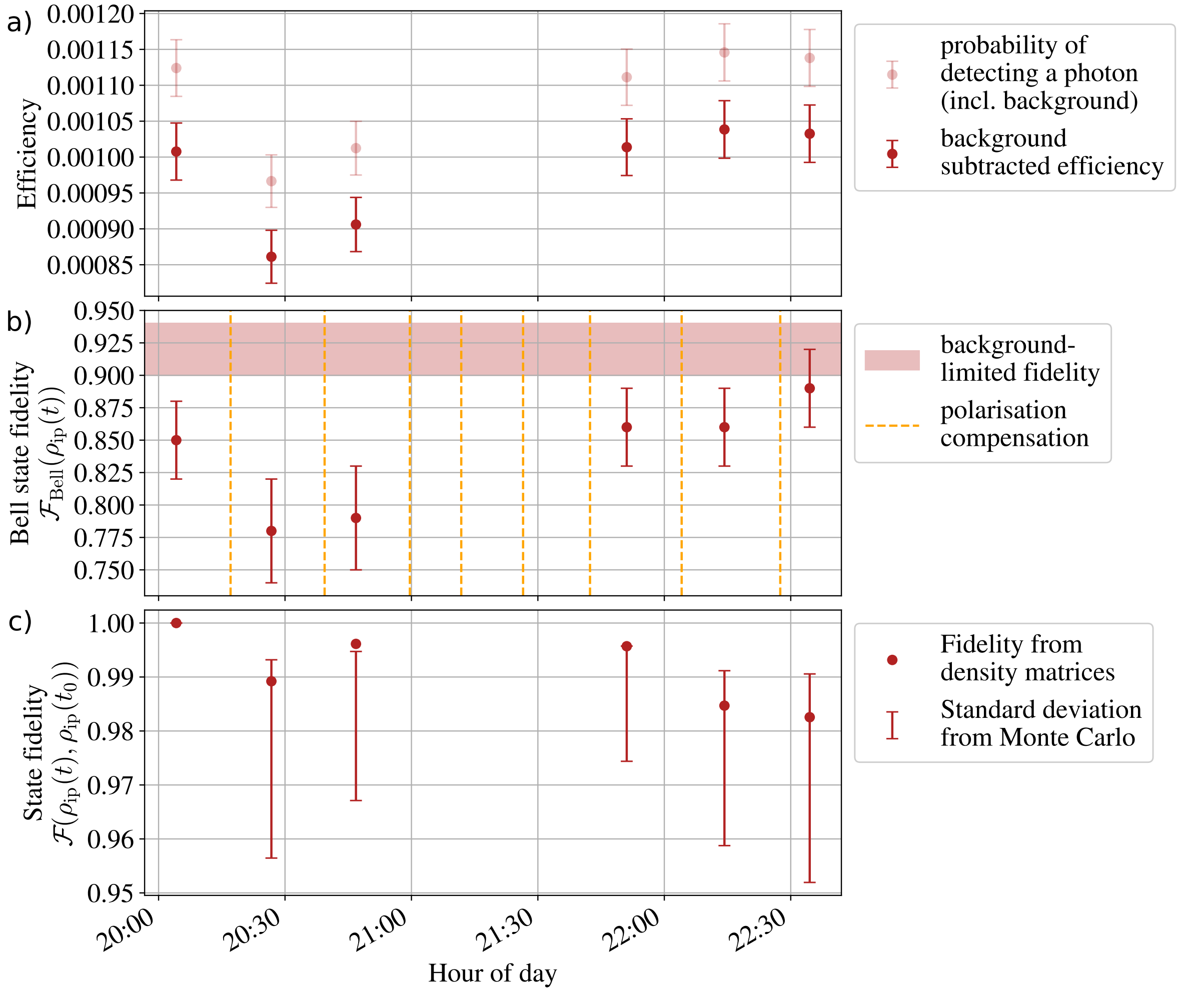

Figure 7.8: Efficiency, fidelity to nearest Bell state, and fidelity to the first measurement point of the ion-entangled 1550 nm photons measured at the Mutters photon detection station. a) Efficiency of the photons, calculated as the ratio of the number of photon detection events in the wavepacket (total number of counts minus the number of background counts) of each of the six successful measurement runs to the number of attempts. For comparison, the probability of detecting any photon (either a photon emitted from the ion or a background photon) is plotted in light red. b) Fidelity of the measured ion-photon density matrix to the nearest ideal Bell state. The red rectangle indicates the range in which the fidelity is expected to lie if the only imperfection were noise counts. c) Fidelity between the nearest Bell states found at each time t and the first one at the initial time t_0. Errors are calculated using a Monte Carlo simulation.

structed and rotated state $\rho_{\mathrm{ip}}(t)$ with the ideal Bell state $|\Phi^+\rangle$ is calculated and denoted as $\mathcal{F}_{\mathrm{Bell}}(\rho_{\mathrm{ip}}(t)) = \mathcal{F}(\rho_{\mathrm{ip}}(t), |\Phi^+\rangle\langle\Phi^+|)$.

For comparison, the ion-photon state of the last local 854 nm entanglement measurement

Table 7.1: Photon efficiency budget. The efficiencies for different components are based on either lab measurements (the date of the measurement is given in the last column) or specification sheets. "Mutters", given in brackets, refers to the Mutters photon detection station. The efficiency of the 854 nm ion-entangled photons is the background-subtracted efficiency. The board efficiencies given are the ratio between the sum of the measured powers at the two outputs (power coupled into the fibres at the output) and the power after the input collimator. The error bars on the board efficiencies are calculated by assuming an uncertainty on the last measured digit of the powers. The expected efficiency of the 854 nm ion-entangled photons is calculated by dividing the measured 854 nm efficiency by the 854 nm analysis board and 854 nm SNSPD efficiencies. The mean of the two listed SNSPD efficiencies (854 nm and 1550 nm, respectively) is used in the calculations. The expected efficiency of the 854 nm ion-entangled photons is multiplied by all components in the 1550 nm photon path to obtain the expected efficiency of the 1550 nm ion-entangled photons.

Component	**Efficiency**	**Source**
Measured 854 nm ion-entangled photons (Lanyon lab)	0.0706(7)	measured on 20.12.2024
854 nm photon polarisation analysis board (Lanyon lab)	0.854(5)	measured on 21.11.2024
854 nm SNSPD (Lanyon lab)	0.86 and 0.88	specification sheet, Subsection 3.1.1
Expected 854 nm ion-entangled photons before QFC	**0.0950(11)**	
QFC	0.214(6)	measured on 20.12.2024, Section 7.2
Off-campus fibre path 2	0.192(8)	measured on 18.06.2024, Section 5.3
FBG	0.54(2)	measured on 17.09.2024, Section 4.3
1550 nm photon polarisation analysis board (Mutters)	0.6747(10)	measured on 17.10.2024
1550 nm SNSPD (Mutters)	0.81(3) and 0.83(3)	specification sheet, Section 4.3
Expected 1550 nm ion-entangled photons (Mutters)	**0.00116(8)**	

run has a Bell state fidelity of 0.945(8). The fidelities for the remote 1550 nm entanglement measurement runs are between 0.78(4) and 0.89(3), as shown in Figure 7.8b. The average Bell state fidelity of the last three runs, taken after optimising the Raman resonance, is

0.870(17). According to calculations performed by Dr. Viktor Krutianskii, as described in the Supplementary material Section IV of Ref. [23], the fidelity is limited to 0.92(2) for a perfect Bell state with only background counts of $2.0(2)\,\mathrm{s}^{-1}$ added. Possible causes for a fidelity lower than the limit attributed to the background are the decoherence of the ion-qubit during the photon detection time window and imperfections in the ion-photon state at 854 nm. Specifically, the imperfections in the ion-photon state at 854 nm can be imperfections in the ion-qubit state preparation and manipulation, including imperfections in the bichromatic Raman pulse causing the generated ion-photon state to be slightly imbalanced (i.e., a state $|\Psi\rangle = \alpha\,|00\rangle + \beta\,|11\rangle$ with $\alpha \neq \beta$). Polarisation drifts during the measurement can also be a cause for infidelity, but the measurements shown in Figure 7.6 exclude that the polarisation drifts caused a few percent infidelity of the ion-photon state.

Comparing the ion-photon state $\rho_{\mathrm{ip}}(t)$ to the first measured state $\rho_{\mathrm{ip}}(t_0)$ by calculating the state fidelity (Equation (2.44)) shows that the last five measured states have the same fidelity with respect to $\rho_{\mathrm{ip}}(t_0)$ within the error bars (Figure 7.8c). The lowest fidelity of the reconstructed ion-photon states with respect to the first reconstructed ion-photon state is $0.983^{+0.008}_{-0.031}$. The error bars are calculated using a Monte Carlo simulation.

7.3. Conclusion

The first experiment involving single photons presented in this thesis was the distribution of polarised photons off-campus. Polarisation drift compensation was implemented and applied regularly throughout the experiment. The efficiency of the photons detected at the Mutters photon detection station fluctuated between 0.00038(3) and 0.00070(4) during the 80 minutes of the measurements. The lowest fidelity of the reconstructed density matrices describing the polarisation of the photons with the first one of these density matrices is $0.977^{+0.005}_{-0.031}$.

The second experiment involving single photons presented in this thesis is the measurement of ion-photon entanglement. The ion is located in the Lanyon lab at the Technik campus, and the photon emitted by the ion is converted in frequency, sent through the off-campus fibre path 2, and detected at the Mutters photon detection station. The efficiency was increased up to 0.00104(4) compared to the efficiency of the polarised photons. The maximum efficiency expected from independent characterisations of the photon path is 0.00116(8). Possible causes for the mismatch can be fibre joiners and patch fibres. On average, ion-entangled photons were detected at the Mutters photon detection station at a rate of 0.815(13) Hz. The fidelities of the reconstructed ion-photon states with a perfect Bell state are between 0.78(4) and 0.89(3) over six repeated measurements. Due to background counts alone, the fidelity would be limited to 0.92(2) even for an otherwise perfect ion-photon Bell state. Other sources of infidelity could be imperfections in the state preparation and manipulation of the ion-qubit and decoherence during the photon detection time window. The lowest fidelity of the reconstructed ion-photon states with respect to the first reconstructed ion-photon state is $0.983^{+0.008}_{-0.031}$, meaning that the distributed state did not significantly rotate over the six measurement runs. These fidelities are comparable to the fidelities of the reconstructed density matrices of the polarised photons with the first one. The last three characterised entangled ion-photon states were obtained after re-optimising the Raman resonance, which can be attributed to producing higher and more stable efficiencies and fidelities. The average Bell state fidelity of those last three runs is 0.870(17).

Without polarisation drift compensation, the lowest fidelity of the Choi matrices describing the process implemented by the off-campus fibre path 2 on polarised light with respect to the Choi matrix before the first measurement run is around 0.9995 for the experiment with polarised photons and around 0.9986 for the ion-photon entanglement. These fidelities are within or higher than the compensation fidelity of 0.9974 to 0.9987 presented in Chapter 6. Therefore, the compensation of the off-campus fibre path 2 did not significantly improve the fidelities of the experiments involving single photons with the given measured polarisation drifts. However, the characterisation of the polarisation drifts (as in Section 5.2) between the measurements is valuable to quantify the polarisation drifts during the experiment and to reveal when to repeat a measurement run in the case that the polarisation drifts exceed any set threshold. In future, longer experiments with single photons, polarisation drifts may become more significant, making active polarisation control advantageous.

8. Summary and outlook

This thesis introduced basic concepts of quantum information, covering how information can be encoded and manipulated using photonic polarisation qubits, as well as how quantum states and processes can be reconstructed. The fidelity (Equation (2.44)) was presented as a quantitative measure for comparing quantum states, and analogously, for comparing quantum processes represented by their Choi matrices. The pre-existing experimental setup, comprising the cavity-integrated ion trap and the quantum frequency conversion (QFC) systems, was introduced, along with the techniques established for generating and measuring ion-photon entanglement. The resulting two-qubit state consists of an ion and a photon at 1550 nm. The off-campus fibre path and the photon detection station in Mutters, to which such a photon is sent, were described. Additionally, the setup used to compensate for polarisation changes experienced by light during transmission through the off-campus fibre was presented. In the following three paragraphs, the three main achievements are summarised.

First, the off-campus optical fibre was characterised in several ways. Hundreds of background photons per second were measured in the approximately 34 km-long off-campus fibre loop. With an additional 1.5 GHz spectral filter, the average background in the off-campus fibre path 2 could be reduced to 1.209(4) counts per second, dominated by the detectors' dark count rate. Polarisation drift of the light sent through the off-campus fibre loop typically did not occur on a timescale of ten minutes, but rather over several tens of minutes to hours. The transmission efficiencies at 1550 nm of the two 17 km-long off-campus fibre paths were measured to be 0.205(8) and 0.192(3), which is half of the transmission expected for an ideal fibre without splices, connectors and fibre fan-out boxes. No polarisation-dependent loss (PDL) at the level of the statistical precision of the measurements could be measured in the off-campus fibre path 2.

Second, polarisation drift compensation was implemented on the off-campus fibre path 1 over nearly four days with ten-minute intervals between the compensations. The compensation fidelity with respect to the identity was always in the range between 0.9974 and 0.9987. Polarisation drift compensation, including the compensation check, took about one minute each time, mainly limited by the speed of the rotation of the waveplates. Performing polarisation drift compensation does not significantly slow down the experiments involving single photons presented in this thesis.

Third, two experiments involving single photons were presented. The first experiment involved repeatedly sending polarised photons emitted by the trapped ion, converted in frequency, and transmitted to the Mutters photon detection station. Eight measurement runs were conducted over 80 minutes, with polarisation drift compensation before each run. Comparing the reconstructed photon-qubit states with the first one shows that the infidelity between them is less than three percent. The second experiment aimed to demonstrate ion-photon entanglement across the off-campus fibre path 2. Six successful measurement runs were conducted over two and a half hours, with polarisation drift compensation before each run. On average, the detection rate of ion-entangled photons at the Mutters photon detection station was 0.815(13) Hz with a photon generation, conversion, transmission and detection efficiency of about one in a thousand. The fidelities of the reconstructed ion-photon states with respect to an ideal Bell state ranged from 0.78(4) to 0.89(3), confirming the presence of entanglement as they are above 0.5. The background counts alone were found to be a significant source of the infidelity of the reconstructed ion-photon states. The polarisation drifts in the off-campus fibre during the two experiments involving single photons were lower than the error of the polarisation drift compensation. Therefore, the polarisation drift compensation was not necessary for these experiments. Nevertheless, characterising the polarisation drift was valuable for confirming the stability of the off-campus fibre during the experiments. The data show that the polarisation drifts in the off-campus fibre were too small to explain the observed infidelities of the polarised photons and the reconstructed ion-photon states compared to an ideal Bell state. Instead, a significant source of infidelity was the dark count rate of the detectors.

The work presented in this thesis represents an initial step towards the demonstration of a quantum repeater node using deployed optical fibre, as proposed in Ref. [24]. At the time of writing, this repeater node experiment is ongoing, and the polarisation drift compensation setup developed in this thesis has already been employed on several occasions to mitigate polarisation drifts in the deployed fibre. The use of deployed, commercial fibre networks will play a central role in the development of large-scale quantum networks. Those networks could be built by connecting two network nodes directly by such deployed fibres, or by using quantum repeaters [99]. However, whenever quantum information is encoded in the polarisation of photons, the polarisation changes introduced by the fibre should be taken into account and possibly compensated in future implementations.

A. Appendix

A.1. Pictures of the Mutters photon detection station and quantum frequency conversion setups

Figure A.1 shows the room in which the Mutters photon detection is built as it was on 18.04.2024. Figure A.2 shows the polarisation analysis rack and the superconducting nanowire single photon detector (SNSPD) rack in that room one year later on 25.04.2025.

(a) View from the door of the Mutters office.

(b) View from the opposite side of the door.

Figure A.1: Mutters office on 18. April 2024. This is how the Mutters office, lying on the top floor of the building at Gewerbepark Mutters-Gärberbach 7, was at the beginning of my master's thesis. Windows are facing West-Northwest with an azimuth angle of about 290° estimated from basemap.at. The blinds are closed to prevent sunlight shining directly into the office.

Figure A.2: Picture of the two racks in Mutters. The rack on the left is the polarisation analysis rack. It contains several shelves, on which there are (from top to bottom) the Mutters control PC, the breadboard with the optical setup, the electronics (Arduinos, USB hub, waveplate controller, power socket), the fibre Bragg grating (FBG) next to the electro-optic converter (transmitter) and the pulse matcher, and the fibre bundle at the bottom. The rack on the right including the compressor to its side is the SNSPD. Picture taken on 25.04.2025.

A.2. Waveplate characterisation

This section explains the setup and procedure adopted for finding the optical axis of a waveplate (quarter-waveplate (QWP) or half-waveplate (HWP)). The results of the waveplate characterisation are used to set the angles of the waveplates in Chapters 5, 6, and 7. In this experiment, I am using a 1550 nm laser[80], a single-mode fibre, a fibre collimator[81], a Glan-laser polariser (GL)[82], a waveplate to be characterised (QWPs and HWPs[83] mounted in motorised stages connected to two-axis controllers[84]), a polarising beam splitter (PBS) cube[85], and a powermeter[86].

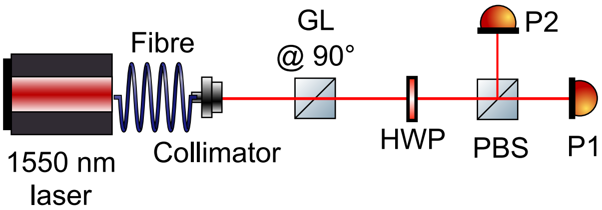

Figure A.3: Setup for characterisation of waveplates at 1550 nm. The GL is rotated such that the reflection path is perpendicular to the optical table (and the plane spanned by the output paths of the GL is perpendicular to the surface spanned by the output path of the PBS, which is parallel to the table). The HWP is shown in the place where the waveplate to be characterised (HWP or QWP were characterised for the experiments in this thesis) is placed. P1 and P2 are the positions at which a powermeter is placed to measure the power reflected or transmitted through the PBS.

The setup is shown in Figure A.3. The approach to aligning the setup is described in the following paragraph. First, the PBS is mounted in the beam path and sets the reference frame for the polarisation of the light. It transmits horizontally polarised light and reflects vertically polarised light with respect to the plane of the table, which is perpendicular to the gravitational force. Then, the GL is mounted such that its reflected beam goes down onto the table (denoted as “@ 90°” in Figure A.3, as the plane spanned by the output beams is perpendicular to the surface of the table), and the light transmitted by both the GL and the PBS is minimised by changing the angle at which the GL is mounted. Ideally, the light after the GL is vertically polarised with respect to the table surface. Furthermore, the light after the GL has high polarisation purity since the GL has a high extinction ratio. After the alignment of the GL and the PBS, the waveplate can be inserted between them as shown in Figure A.3. The powers of the reflected and

---

[80] Thorlabs S3FC1550 — DFB Benchtop Laser Source, 1550 nm, 1.5 mW, FC/PC

[81] Schäfter+Kirchhoff 60FC-SF-4-A11-45

[82] Thorlabs Mounted Glan-Laser Polariser GL10. Extinction ratio 100000:1 in transmission [84].

[83] Cening half and quarter-waveplate, zero order, optically contacted, diameter 25.4 mm, unmounted, AR coated for 1550 nm.

[84] Standa 8MPR16-1 motorised polariser rotator with 8SMC5-USB-B9-2 controller

[85] CeNing Optics, anti-reflection coated for 1550 nm, N-BK7 material. Laser line with extinction ratio of 500:1 [100].

[86] Thorlabs S148C — Integrating Sphere Photodiode Power Sensor, extended InGaAs, 1200–2500 nm, 1 µW – 1 W. S/N: 16022502

transmitted beams of the PBS can be measured. The powermeter is placed once in position P1 in Figure A.3 to measure the light transmitted through the PBS, and once in position P2 to measure the light reflected from the PBS.

For the control of the motorised stage in which the waveplate is inserted, a code written by graduated PhD student Vojtěch Krčmarský was modified. I received help from Dr. Fabitha Kodakkat for setting up the device control.

The angle of the waveplate was rotated over 360° in steps of 3° (1° corresponds to 80 steps of the motorised stage), and the power was measured after the motorised stage stopped rotating. The angle 0° on the waveplate stages (set by the "home position" of the waveplate stages) is the starting point and serves as a reference for the determination of the optical axis. For each detector position (at the reflected and the transmitted beam from the PBS), the measurement was done twice: the transmitted powers are denoted as T1 and T2, the reflected powers are denoted as R1 and R2.

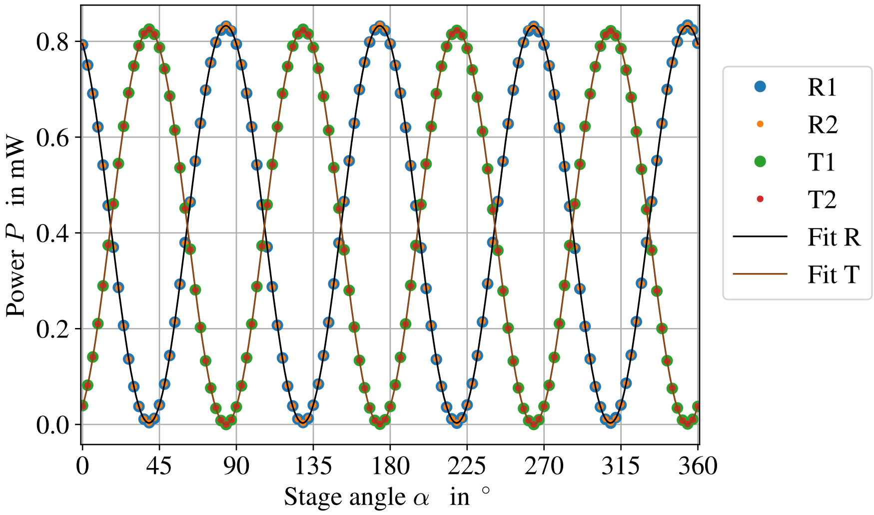

Figure A.4: HWP characterisation. When the powermeter is in position P1 (Figure A.3), the power T1 transmitted through the PBS is measured. Repeating the measurement gives T2. When the powermeter is in position P2 (Figure A.3), the powers R1 and R2 reflected from the PBS are measured. The transmitted and reflected powers are fitted separately. The fit functions Fit R and Fit T are shown in the main text in Equations (A.1) and (A.2), respectively. The fit parameters for P_R are $A = -0.82941(17)$, $T = 89.988(3)°$, $\alpha_0 = 38.856(5)°$, $c = 0.83251(11)$. The fit parameters for P_T are $A = -0.82315(16)$, $T = 89.986(2)°$, $\alpha_0 = 38.854(5)$, $c = 0.8234(10)$. The errors represent one standard deviation obtained from the covariance matrix of the fit. Measurements were taken on 27.05.2024 on HWP 2 (Figure 4.1) in the stage with the serial number 203972.

For the reflected beam, a function proportional to the cosine squared is fitted to both measurement sets R1 and R2:

$$P_\mathrm{R}(\alpha) = A\cos^2\left(\frac{\pi}{T}(\alpha - \alpha_0)\right) + c \tag{A.1}$$

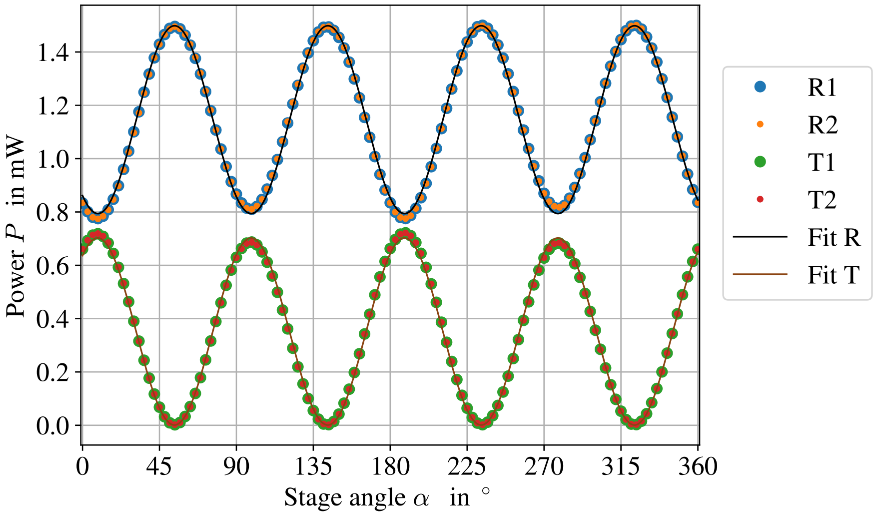

Figure A.5: QWP characterisation. The fit functions Fit R and Fit T are shown in the main text in Equations (A.1) and (A.2), respectively. The fit parameters for P_R are $A = -0.705(2)$, $T = 89.70(4)°$, $\alpha_0 = 8.99(9)°$, $c = 1.4984(14)$. The fit parameters for P_T are $A = -0.701(2)$, $T = 89.73(4)°$, $\alpha_0 = 8.90(9)$, $c = 0.7023(13)$. The errors represent one standard deviation obtained from the covariance matrix of the fit. Measurements were taken on 03.04.2024 on QWP 1 (Figure 4.1) in the stage with the serial number 179338.

where A is the amplitude, T is the period, α_0 is the phase shift corresponding to the angle of the optical axis, and c is the power offset. Similarly, a sine squared function is fitted to the transmitted beam:

$$P_\mathrm{T}(\alpha) = A\sin^2\left(\frac{\pi}{T}(\alpha - \alpha_0)\right) + c. \tag{A.2}$$

The waveplate characterisation for a HWP is shown in Figure A.4, and for a QWP in Figure A.5, including the fit parameters in the figure captions.

For the QWP, the two fits should ideally touch each other at the maximum transmission. However, the two fits in Figure A.5 do not touch. For the determination of the optical axis, the deviation from the ideal case is not relevant. Possible causes for the deviation include fluctuations in the laser power transmitted through the GL, caused by touching the single-mode fibre between the laser and the fibre collimator while the powermeter was being aligned to the new position P1 or P2.

One of the drawbacks of the setup used for waveplate characterisation is its dependency on the beamsplitters used. The angle of the first beamsplitter is aligned with respect to the second PBS, and therefore the reference angle for these measurements is set by the second PBS. The given errors for the angle of the optical axis are purely statistical and do not include this systematic error. Thus, if the waveplate is placed in another setup also involving a PBS, the reference angle could differ slightly from that used in this experiment.

In principle, the optical axis can also be determined by measuring either transmission or reflection alone. However, for these waveplates, both transmission and reflection were measured, and therefore the mean of the parameter α_0 obtained from the P_{R} and P_{T} fits is chosen to set the optical axis. However, it is not possible to determine at which angle of a QWP the light becomes left- or right-hand circularly polarised. Therefore, when setting up the experiments presented in Chapters 6 and 7, the circular polarisation is checked with a polarimeter[87]. The optical axes for waveplates 1–5 (Figure 4.1 and Figure 4.2) used for the experiments presented in Chapters 6 and 7 are listed in Table A.1. For the experiment presented in Section 5.2, the optical axis of the waveplate was known from characterisations done prior to the start of my master's thesis project.

Table A.1: Optical axes set for the waveplates used in Chapters 6 and 7. The waveplate number corresponds to the labels in Figure 4.1 and Figure 4.2. The stage number refers to the serial number written on the stage in which the waveplate is mounted. The optical axis is given in steps (1° corresponds to 80 steps), measured from the home position of the waveplate stage.

Waveplate type and number	Stage number	Optical axis (steps)
QWP 1	179338	4316
HWP 2	203973	6708
QWP 3	183300	1652
HWP 4	183384	5540
QWP 5	226797	5821

A.3. Dependence of the background counts in the off-campus fibre loop on external factors

This section aims to display the possible influence of some external factors on the background counts in the off-campus fibre loop. Specifically, Subsection A.3.1 shows the temperature and irradiation in Innsbruck during the background light measurement presented in Section 5.1. Subsection A.3.2 shows the dependence of the background counts in the off-campus fibre loop on the status (on/off) of the lights in the Lanyon lab and in the room of the Zentraler Informatik Dienst at the University of Innsbruck (ZID).

A.3.1. Background counts and weather conditions in Innsbruck

The global radiation (solar incoming radiation) and the sunshine duration are measured on the rooftop of the university building at Innrain 52f, Innsbruck. By looking at the global radiation and the sunshine duration per minute in Figure A.6, it appears that on two (Saturday and Sunday) out of the three days of measurement, the sun is shining almost continuously. While the sunshine duration is nearly discrete (either the sun

---

[87] Thorlabs PAX1000IR2(/M)

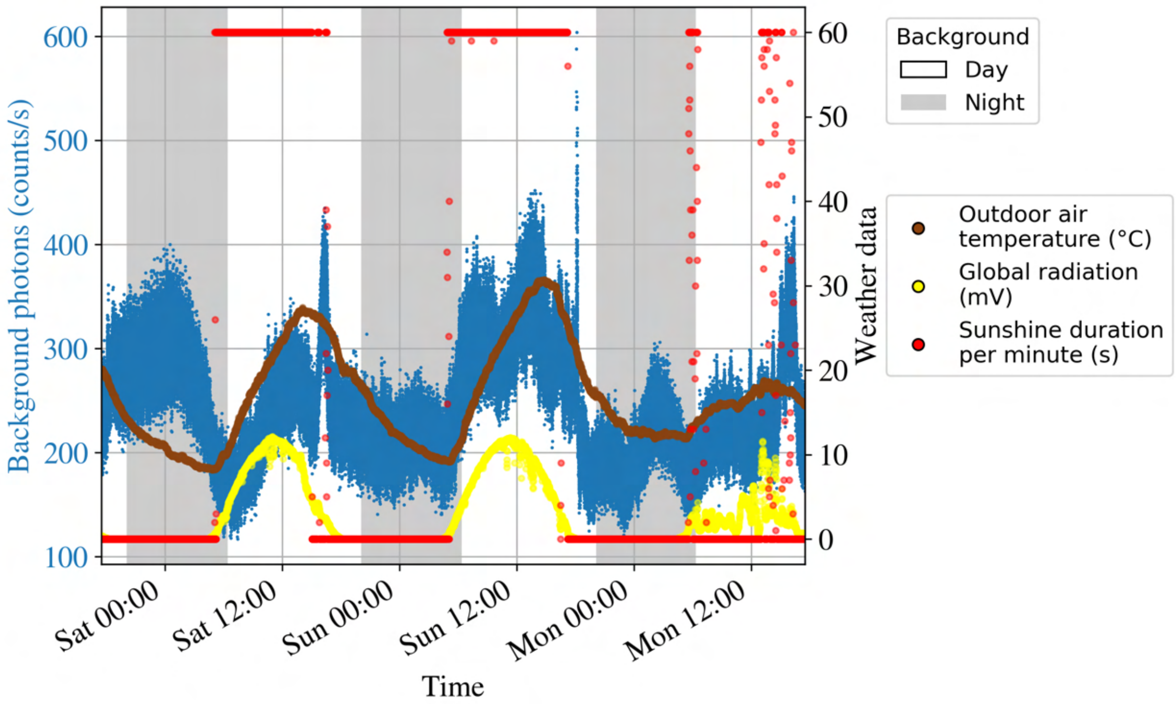

Figure A.6: Off-campus fibre loop background counts and weather conditions. The outdoor air temperature (measured in °C), the global radiation (given in units of mV as measured by a pyranometer, which could be converted to units of Watts by multiplication with a scaling factor given in Ref. [88]), and the sunshine duration per minute (given in seconds) are plotted on top of the background counts of Figure 5.1. The weather data is taken from Ref. [90]. The outdoor air temperature is measured in Schöpfstraße 45, Innsbruck. The global radiation and the sunshine duration are measured on the rooftop of the university building at Innrain 52f, Innsbruck.

is shining or it is not), the global radiation changes continuously throughout the day and peaks around lunchtime. Neither the sunshine duration nor the global radiation seems to be clearly correlated with the measured background counts. However, it can be speculated that the sharp peaks in the background counts in the afternoons are related to the setting sun illuminating an exposed part of the fibre. The outdoor air temperature depends on the global radiation, but the temperature curve changes more slowly than the radiation due to the thermal inertia of the air. Plotting the temperature over the measured background counts, as in Figure A.6, shows some overlap in the tendencies of the two values. However, the background counts exhibit fast fluctuations, and there are times when there is no overlap between the temperature and the background (for example, during the first night from Friday to Saturday). Furthermore, the outdoor air temperature does not have the sharp peaks in the afternoons that the background counts display. To summarise, the weather in Innsbruck may influence the measured background counts, but the correlation is not clear, and there are certainly other effects influencing the background counts in the off-campus fibre loop as well.

A.3.2. Increase in the number of background photons due to room lights in the off-campus fibre loop

To estimate the influence of the room lights in the Lanyon lab and in the ZID room, separate measurements are performed. The same setup as described in Section 5.1 is used: the off-campus fibre loop is used, one end is capped, and the other end is connected to the 1550 nm SNSPD in the Lanyon lab. The measurements are taken together with Dr. Fabitha Kodakkat.

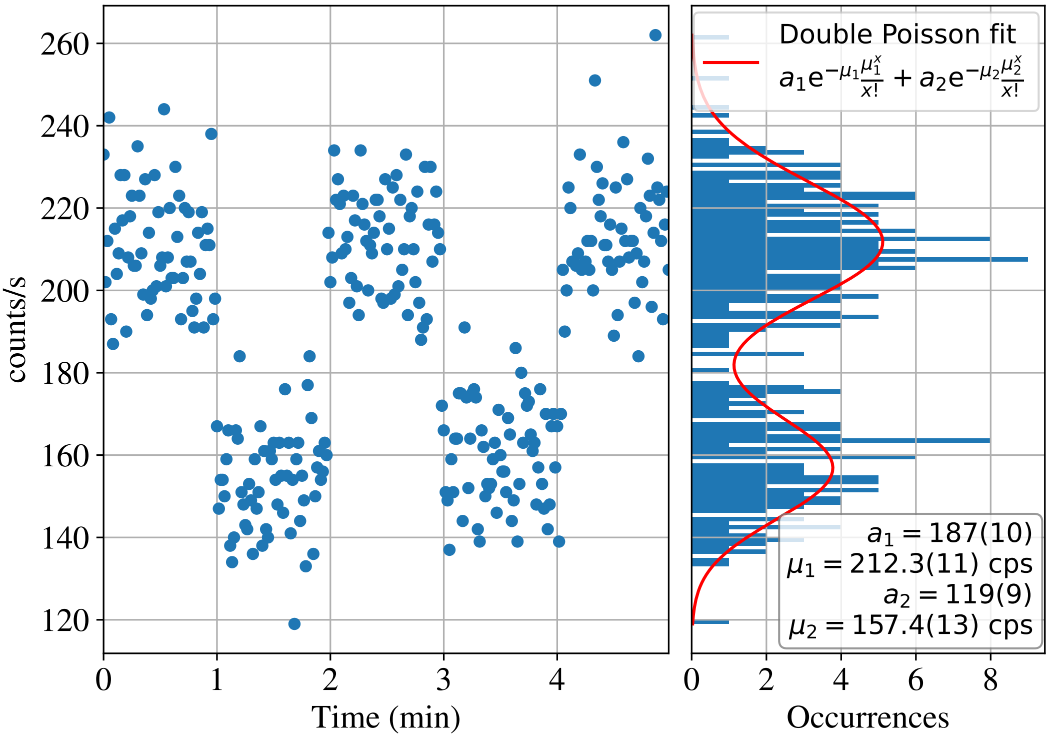

Figure A.7: Off-campus fibre loop background light dependence on the lights in the Lanyon lab. The measurement starts with the room lights in the Lanyon lab switched on. After one minute, the lights are switched off, resulting in a decrease in counts. After another minute, the lights are switched on again. The procedure is repeated and shown on the left side of the figure. The right side shows a histogram of the registered counts. The distributions are fitted with two Poissonian distributions, the amplitudes a_i and means μ_i of which are shown on the lower right. The error bars given are the square roots of the variances (i.e., the standard deviation) obtained from the fit. Data taken on 08.05.2024 from 18:04 onward.

A five-minute-long measurement where the lights in the Lanyon lab are switched on and off, alternating every minute, is shown in Figure A.7. The lights in the ZID room are assumed to be off. There is a clear change in the measured counts per second when the lights are on, compared to when they are off: 212.3(11) and 157.4(13) counts per second, respectively. The errors are the standard deviations obtained from the fit. The contribution of the lights in the Lanyon lab is 212.3(11) − 157.4(13) = 54.9(17) counts per second.

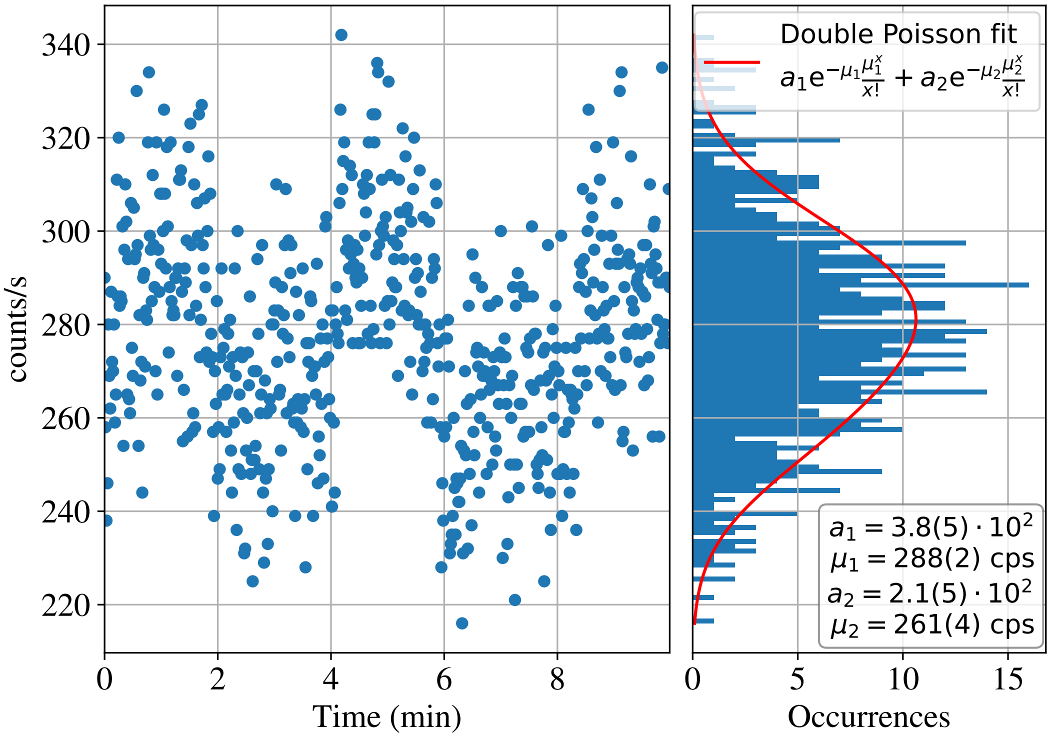

Figure A.8: Off-campus fibre loop background dependence on ZID lights. The measurement starts with the room lights in the ZID room switched on. The lights in the Lanyon lab are off during the entire measurement. After two minutes, the lights in the ZID room are switched off, resulting in a decrease in counts. After another two minutes, the lights are switched on again. The procedure is repeated and shown on the left side of the figure. The right side shows a histogram of the registered counts. The distributions are fitted with two Poissonian distributions, the amplitudes a_i and means μ_i of which are shown on the lower right. The error bars given are the square roots of the variances (i.e., the standard deviation) obtained from the fit. Data taken on 15.05.2024 from 15:16 onward.

A ten-minute-long measurement where the lights in the Lanyon lab are switched on and off, alternating every two minutes, is shown in Figure A.8. The lights in the Lanyon lab are off. Compared to the clear change in the measured counts per second when the lights in the Lanyon lab are on or off, the change observed when the lights in the ZID room are on or off is less pronounced but still evident: 288(2) and 261(4) counts per second, respectively. The contribution of the lights in the Lanyon lab is 288(2) − 261(4) = 27(5) counts per second. The measurements are taken on different days, and therefore, the "offset" background light in the off-campus fibre loop is different in Figures A.7 and A.8.

The measurements of the room lights in the Lanyon lab and in the ZID room lead to the following conclusions. Light leaks into the fibre even when the end is capped, i.e., through the outer jacket of the fibre into the fibre core. In the one-way configuration (as used in Chapter 7), the light is attenuated and possibly partially filtered by the FBG, which has a narrower bandwidth than the SNSPDs. The effect of the room lights in Mutters is not investigated, but it is expected to contribute similarly in the one-way configuration as the lights in the Lanyon lab in the off-campus fibre loop configuration shown in Figure A.7. Therefore, beyond the use of filters and shielding of the fibres and free-space paths, the room lights should be switched off during experiments with single photons to reduce the measured background light.

A.4. Measured transmission for the determination of the polarisation-dependent loss of off-campus fibre path 2

The transmission of the off-campus fibre path 2 in dependence on different polarisation states sent into the fibre is shown in Figure A.9. The shown transmission is in arbitrary units and corresponds to the optical transmission of the fibre up to a scaling factor. The fluctuations in the transmission correspond to rotations of the waveplates. At the beginning and end of the measurement, for about ten seconds each, the waveplates are not rotated while the power is measured. The maximum transmission shown in Figure A.9 is 0.920(2), the minimum transmission is 0.864(2). The resulting polarisation-dependent loss (PDL) using Equation (2.46) is 0.274(16) dB.

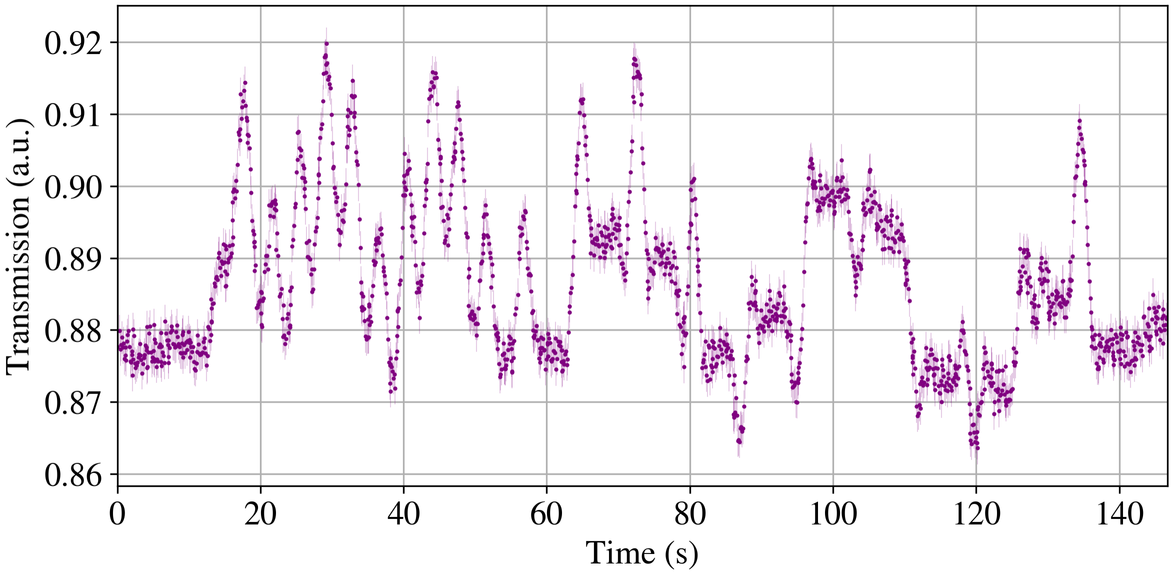

Figure A.9: Measured transmission over time during which different polarisations are prepared and sent through off-campus fibre path 2. The shown transmission is the power measured at the output of the off-campus fibre path 2 divided by the measured power reflected from the microscope slide. The error bars on each point (purple) are shown as vertical lines in light purple. A total of 1533 measurement points are displayed. Measurements taken on 12.08.2024.

A.5. From a Choi matrix to compensation angles for waveplates

This section describes how a Choi matrix E, describing a process on a polarisation qubit or polarised laser light, is approximately inverted by using waveplates. The code for these computations was written by graduated PhD student Vojtěch Krčmarský and used for the polarisation drift compensations described in this master's thesis.

Once the Choi matrix E (describing the process implemented by the fibre) is obtained, the question arises of how to reverse the process by using the waveplate combination of QWP, HWP, and QWP, such that the fibre and the waveplates implement the identity operation. As mentioned in Subsection 2.2.3, ideal waveplates can only implement unitary operations, and therefore compensate unitary processes. The Choi matrix E can describe unitary as well as non-unitary processes, so it is necessary to find the nearest unitary to E. Once the nearest unitary is found, the inverse of the unitary can be decomposed into the waveplate angles described by U_{QHQ} (Equation (2.33)).

For a single-qubit process, the 4×4 Choi matrix representing the process can be rewritten using the Kraus representation, which consists of 2×2 matrices. To do so, the Choi matrix is decomposed into its eigenvalues λ_i and 4×1 eigenvectors $\vec{v}_i$. Then, the Kraus matrices K_i can be written as [101, 102]

$$K_i = \sqrt{\lambda_i} \begin{pmatrix} v_{i,0} & v_{i,2} \\ v_{i,1} & v_{i,3} \end{pmatrix} . \tag{A.3}$$

A density matrix subjected to the process can then be represented in the Kraus matrix representation shown in Equation (2.14). Recalling the condition $\sum_i K_i^\dagger K_i = \mathbb{1}$ for the Kraus matrices to describe a trace-preserving process, and the condition that a unitary operation must fulfil $U^\dagger U = \mathbb{1}$, one can see that if there is only one K_i describing a trace-preserving process, then that K_i describes a unitary operation.

The Kraus matrix corresponding to the largest eigenvalue and having the largest "weight" in Equation (2.14) is normalised and called A.

The inversion of A is then used as the target matrix $A_{\mathrm{target}} = A^{-1}$ that should be implemented by the combination of QWP, HWP, and QWP to compensate for the process implemented by the fibre. Even though the matrix A_{target} is not a perfect unitary operation, the algorithm to decompose the matrix into the unitary operation $U_{\mathrm{QHQ}}(\alpha_1, \alpha_2, \alpha_3)$, described in Subsection 2.2.3, is applied. The algorithm should find the waveplate angles that allow the implementation of the nearest unitary to A_{target}. The initial guess for the waveplate angles is given by $\alpha_{1,\mathrm{init}} = \pi/10\,\mathrm{rad}$, $\alpha_{2,\mathrm{init}} = \pi/12\,\mathrm{rad}$ and $\alpha_{3,\mathrm{init}} = \pi/8\,\mathrm{rad}$, taken over from Vojtěch Krčmarský's code.

A different method to obtain the waveplate angles, which is not applied in this thesis but might be worth considering, would be to search for the optimal waveplate angles directly with respect to the Choi matrix E. This could be achieved by computing the inverse of $U_{\mathrm{QHQ}}(\alpha_1, \alpha_2, \alpha_3)$ for each combination, converting the unitary $U_{\mathrm{QHQ}}(\alpha_1, \alpha_2, \alpha_3)^{-1}$ to a Choi matrix $E(U_{\mathrm{QHQ}}^{-1})$, and minimising the difference between E and $E(U_{\mathrm{QHQ}}^{-1})$ by changing the waveplate angles accordingly.

A.6. Instructions for running polarisation drift compensation

The section explains the technical details of running the polarisation drift compensation with the setup presented in Section 4.4. It starts with how to make a transistor-transistor logic (TTL) signal using an Arduino controlled by a Python script. Then, the way in which the mirrors are set up and the exact sequence chosen to flip the mirrors and the shutter is explained. Finally, a checklist is presented that can be used to verify whether all parts of the polarisation drift compensation setup are working before proceeding to the execution of the Python scripts for polarisation drift compensation.

Generate TTL signals with an Arduino and Python. An Arduino is an electronics platform consisting of a programmable board (microcontroller) and an integrated development environment (IDE) software. For the polarisation drift compensation setup, three Arduino boards[88] are used: one for each of the two flip mirrors and one for the shutter. To generate TTL signals, the digital output pins are used. Each Arduino board is connected to a Universal Serial Bus (USB) hub connected to a PC.

To send TTL signals with the Arduino board, the Arduino IDE software is downloaded on the respective PC. The communication port to which the Arduino board is connected to the PC has to be selected in the software (under the header “Tools”). Then, the pre-written Arduino program *StandardFirmata* is uploaded (under “File/Examples/Firmata/StandardFirmata”) [103], allowing control of the Arduino board with Python.

An example Python code to set 5 V at the output port is shown in the snippet of Code 1.

Code 1: Controlling an Arduino pin with PyFirmata.

```python
import pyfirmata
board = pyfirmata.Arduino(’COM5’) # COM of the Arduino
board.digital[11].write(1) # digital pin number 11, write(1) sets 5 V
board.exit()
```

Similarly, the command *board.digital[11].write(0)* can be used to set the TTL signal voltage to 0 V.

Safety sequence of flipping mirrors and shutter. For safety reasons, a special sequence of flipping the mirrors and shutter is chosen such that, in the event of a power failure, no laser light is sent to the SNSPDs at the Mutters photon detection station.

The flip mirror in the Lanyon lab is mounted such that if the TTL signal is at 0 V, no laser light is sent through the off-campus fibre path. The flip mirror at the Mutters photon detection station is mounted such that if the TTL signal is at 0 V, light or photons coming out of the off-campus fibre path are directed onto the polarimeter. The shutter

---

[88] Arduino Leonardo AOOOO57 Core AT Mega32

at the Mutters photon detection station is mounted such that if the TTL signal is at 0 V, it blocks the path to the SNSPDs.

Assume that photons from the ion have been sent to the SNSPDs in Mutters (i.e., shutter and flip mirror at the Mutters photon detection station have a TTL signal of 5 V). Now, assume that laser light should be sent to the polarimeter to do polarisation drift compensation. The sequence is as follows:

1. Flip the shutter and mirror at the Mutters photon detection station.
2. Flip the mirror in the Lanyon lab to direct the laser light into the off-campus fibre path.

Upon completion of step 1, a notification is transmitted to the computer controlling the flip mirror in the Lanyon lab. Step 2 is executed only upon receipt of this notification. To resume sending photons, the sequence is performed in reverse order: step 2 is executed and, following confirmation of its successful completion, step 1 is subsequently performed.

Checklist before running Python scripts for polarisation drift compensation. Before attempting to run the Python scripts used for polarisation drift compensation with the setup shown in Figure 4.2, it is advisable to verify that the control of the individual components functions properly. A list of tasks is now given:

- Switch on the 1550 nm laser before the experiment so that it can warm up and is stable during experiments. The frequency should be tuned such that the transmission through the FBG at the Mutters photon detection station (tuned with respect to the 1550 nm light of the quantum frequency conversion (QFC)) is maximal.
- Make sure that the client-server connection is working. This can be done by running Python scripts on the client and on the server, sending and receiving a message.
  - Note that the IP addresses set in the scripts have to match the addresses on the respective PCs.
  - The port number has to be the same in both scripts and correspond to the port number set in the router settings (EdgeMax, “firewall/NAT” tab).
  - On the Mutters control PC, one should be logged in to two websites that allow passing the firewalls of campus Technik and campus Innrain.
- Check that the control of the waveplates in the Lanyon lab is working.
  - Open the software *XiLab* on the Analysis PC and rotate the waveplates.
  - Check the speed of the waveplate rotation. The maximum speed is 1920 steps/s, corresponding to 4 turns per minute [104].
  - Check that after execution of the command “go home”, the counter of the position of the waveplate shows a multiple of 28800 steps (=360°). This is important since the optical axes are measured with respect to the home position.

  - After the checks, do not forget to close *XiLab* so that the waveplates can be accessed and controlled by the Python code.

- Check the control of the shutter and the flip mirrors by running simple scripts, such as the one in Code 1. For control of the shutter via TTL signals, the knob on the control board has to be in the correct position (other positions of the knob are for manual flipping of the shutter).

- Check the control of the polarimeter at the Mutters photon detection station using the Thorlabs polarimeter app. When light is shone on the polarimeter, the polarisation and the power should be measured. Do not forget to close the app at the end, so that the polarimeter can be accessed and controlled by the Python code.

A.7. Actions taken in the Lanyon lab before and during the experiments involving single photons

The actions taken during the experiment involving polarised photons on 29.11.2024 are shown in Figure A.10. The actions taken during the experiment involving ion-entangled photons on 20.12.2024 are shown in Figure A.11. The lights in the Lanyon lab and at the Mutters photon detection station are off during all the attempts to generate and measure ion-photon entanglement.

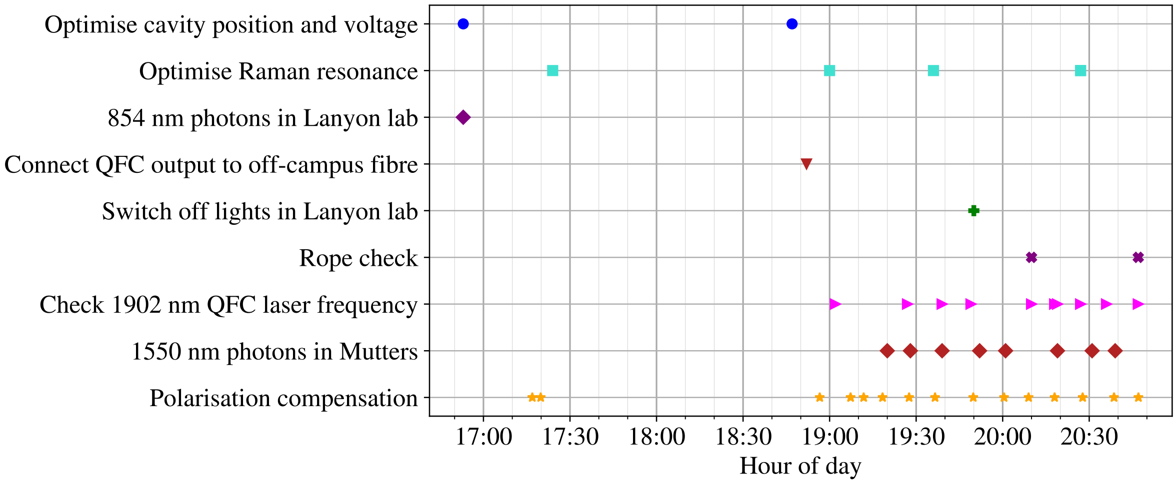

Figure A.10: Overview of actions taken during the experiment with polarised photons. The shown times are the start times of the actions. The most important actions are the purple and red diamonds, showing the times at which photons were measured at 854 nm in the Lanyon lab and at 1550 nm at the Mutters photon detection station, respectively. The polarisation drift compensations (orange stars) are alternated with the measurements of the 1550 nm photons at the Mutters photon detection station. The other actions are calibrations, checks and optimisations, including voltage tuning and position alignment of the cavity (blue dots), and optimisation of the Raman resonance with adjustments of the 393 nm Raman laser frequency if needed (turquoise squares). The term “rope check” refers to a method in which a flip mirror inside the mu-metal shield is moved using a rope, without opening the shield. Rope checks (purple crosses) allow attenuated 854 nm laser light to be sent into the same path followed by the 854 nm photons emerging from the vacuum chamber. These checks are used to maximise the QFC efficiency by adjusting the frequency of the 1902 nm pump laser.

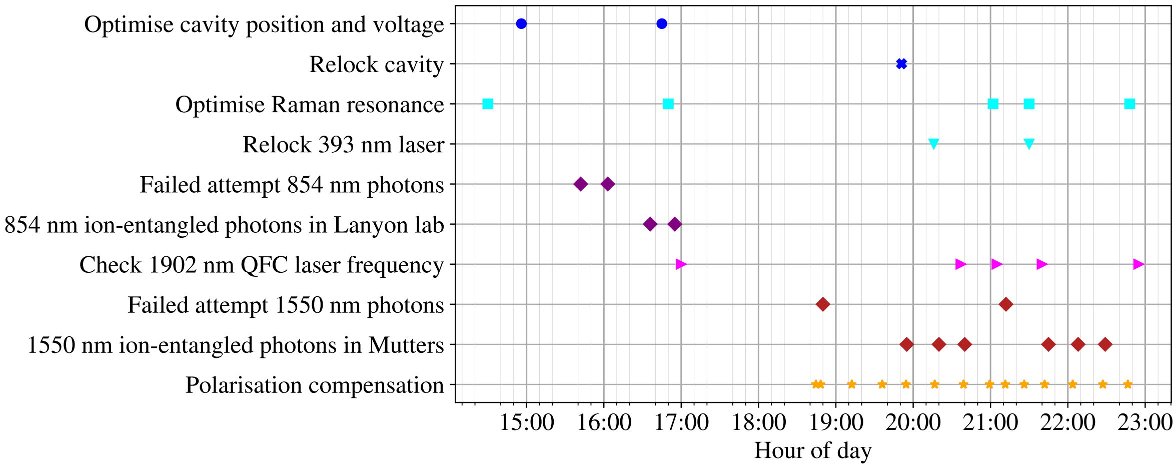

Figure A.11: Overview of actions taken during the experiment with ion-entangled photons. The shown times are the start times of the actions. The most important actions are the purple and red diamonds, showing the times at which ion-entangled photons are generated through the bichromatic cavity-mediated Raman transition (BCMRT). The failed attempts to generate entanglement between the ion and an 854 nm photon are either due to technical reasons or improperly set parameters in the code used to control the experiment. The failed attempts to generate entanglement between the ion and a 1550 nm photon at the Mutters photon detection station are due to errors in the readout of the measurement files. The polarisation drift compensations (orange stars) are alternated with the measurements of the 1550 nm photons at the Mutters photon detection station. The other actions are calibrations, checks and optimisations.

Bibliography

[1] I. M. Georgescu, S. Ashhab, and F. Nori. “Quantum simulation”. In: *Reviews of Modern Physics* 86.1 (2014), pp. 153–185. DOI: 10.1103/RevModPhys.86.153.

[2] S. McArdle et al. “Quantum computational chemistry”. In: *Reviews of Modern Physics* 92.1 (2020), p. 015003. DOI: 10.1103/RevModPhys.92.015003.

[3] P. W. Shor. “Polynomial-time algorithms for prime factorization and discrete logarithms on a quantum computer”. In: *SIAM review* 41.2 (1999), pp. 303–332. DOI: 10.1137/S0036144598347011.

[4] K. Shannon, E. Towe, and O. K. Tonguz. “On the use of quantum entanglement in secure communications: a survey”. In: *arXiv preprint arXiv:2003.07907* (2020). DOI: 10.48550/arXiv.2003.07907.

[5] N. Gisin et al. “Quantum cryptography”. In: *Reviews of modern physics* 74.1 (2002), p. 145. DOI: 10.1103/RevModPhys.74.145.

[6] V. Giovannetti, S. Lloyd, and L. Maccone. “Quantum-enhanced measurements: beating the standard quantum limit”. In: *Science* 306.5700 (2004), pp. 1330–1336. DOI: 10.1126/science.1104149.

[7] C. L. Degen, F. Reinhard, and P. Cappellaro. “Quantum sensing”. In: *Reviews of modern physics* 89.3 (2017), p. 035002. DOI: 10.1103/RevModPhys.89.035002.

[8] H. J. Kimble. “The quantum internet”. In: *Nature* 453.7198 (2008), pp. 1023–1030. DOI: 10.1038/nature07127.

[9] S.-H. Wei et al. “Towards real-world quantum networks: a review”. In: *Laser & Photonics Reviews* 16.3 (2022), p. 2100219. DOI: 10.1002/lpor.202100219.

[10] A. S. Cacciapuoti et al. “When entanglement meets classical communications: Quantum teleportation for the quantum internet”. In: *IEEE Transactions on Communications* 68.6 (2020), pp. 3808–3833. DOI: 10.1109/TCOMM.2020.2978071.

[11] M. Caleffi et al. “Distributed quantum computing: a survey”. In: *Computer Networks* 254 (2024), p. 110672. DOI: 10.1016/j.comnet.2024.110672.

[12] Z. Zhang and Q. Zhuang. “Distributed quantum sensing”. In: *Quantum Science and Technology* 6.4 (2021), p. 043001. DOI: 10.1088/2058-9565/abd4c3.

[13] P. Komar et al. “A quantum network of clocks”. In: *Nature Physics* 10.8 (2014), pp. 582–587. DOI: 10.1038/nphys3000.

[14] P. Maunz et al. “Quantum interference of photon pairs from two remote trapped atomic ions”. In: *Nature Physics* 3.8 (2007), pp. 538–541. DOI: 10.1038/nphys644.

[15] L. Stephenson et al. “High-rate, high-fidelity entanglement of qubits across an elementary quantum network”. In: *Physical review letters* 124.11 (2020), p. 110501. DOI: `10.1103/PhysRevLett.124.110501`.

[16] V. Krutyanskiy et al. “Entanglement of trapped-ion qubits separated by 230 meters”. In: *Physical Review Letters* 130.5 (2023), p. 050803. DOI: `10.1103/PhysRevLett.130.050803`.

[17] S. Ritter et al. “An elementary quantum network of single atoms in optical cavities”. In: *Nature* 484.7393 (2012), pp. 195–200. DOI: `10.1038/nature11023`.

[18] M. Pompili et al. “Realization of a multinode quantum network of remote solid-state qubits”. In: *Science* 372.6539 (2021), pp. 259–264. DOI: `10.1126/science.abg1919`.

[19] A. Delteil et al. “Generation of heralded entanglement between distant hole spins”. In: *Nature Physics* 12.3 (2016), pp. 218–223. DOI: `10.1038/nphys3605`.

[20] S. Zaske et al. “Visible-to-Telecom Quantum Frequency Conversion of Light from a Single Quantum Emitter”. In: *Phys. Rev. Lett.* 109 (2012), p. 147404. DOI: `10.1103/PhysRevLett.109.147404`.

[21] M. Bock et al. “High-fidelity entanglement between a trapped ion and a telecom photon via quantum frequency conversion”. In: *Nature communications* 9.1 (2018), p. 1998. DOI: `10.1038/s41467-018-04341-2`.

[22] T. Walker et al. “Long-distance single photon transmission from a trapped ion via quantum frequency conversion”. In: *Physical review letters* 120.20 (2018), p. 203601. DOI: `10.1103/PhysRevLett.120.203601`.

[23] V. Krutyanskiy et al. “Light-matter entanglement over 50 km of optical fibre”. In: *npj Quantum Information* 5.1 (2019). DOI: `10.1038/s41534-019-0186-3`.

[24] V. Krutyanskiy et al. “Telecom-wavelength quantum repeater node based on a trapped-ion processor”. In: *Physical Review Letters* 130.21 (2023), p. 213601. DOI: `10.1103/PhysRevLett.130.213601`.

[25] V. Krutyanskiy et al. “Multimode ion-photon entanglement over 101 kilometers”. In: *PRX Quantum* 5.2 (2024), p. 020308. DOI: `10.1103/PRXQuantum.5.020308`.

[26] Z.-H. Xiang et al. “Long-term transmission of entangled photons from a single quantum dot over deployed fiber”. In: *Scientific reports* 9.1 (2019), p. 4111. DOI: `10.1038/s41598-019-40912-z`.

[27] T. Van Leent et al. “Entangling single atoms over 33 km telecom fibre”. In: *Nature* 607.7917 (2022), pp. 69–73. DOI: `10.1038/s41586-022-04764-4`.

[28] J. V. Rakonjac et al. “Transmission of light–matter entanglement over a metropolitan network”. In: *Optica Quantum* 1.2 (2023), pp. 94–102. DOI: `10.1364/OPTICAQ.501048`.

[29] QGIS Development Team. *QGIS Geographic Information System*. QGIS Association. 2024. URL: `https://www.qgis.org`.

[30] Data source: basemap.at. *Open Government Data Österreich Lizenz CC-BY 4.0*. 2024. URL: https://basemap.at/.

[31] S. Kucera et al. "Demonstration of quantum network protocols over a 14-km urban fiber link". In: *npj Quantum Information* 10.1 (2024), p. 88. DOI: 10.1038/s41534-024-00886-x.

[32] E. Bersin et al. "Development of a Boston-area 50-km fiber quantum network testbed". In: *Physical Review Applied* 21.1 (2024), p. 014024. DOI: 10.1103/PhysRevLett.130.213601.

[33] A. J. Stolk et al. "Metropolitan-scale heralded entanglement of solid-state qubits". In: *Science advances* 10.44 (2024), p. 6442. DOI: 10.1126/sciadv.adp6442.

[34] M. A. Nielsen and I. L. Chuang. *Quantum computation and quantum information*. Cambridge University press, 2010.

[35] R. Horodecki et al. "Quantum entanglement". In: *Rev. Mod. Phys.* 81 (2009), pp. 865–942. DOI: 10.1103/RevModPhys.81.865.

[36] N. Gisin and H. Bechmann-Pasquinucci. "Bell inequality, Bell states and maximally entangled states for n qubits". In: *Physics Letters A* 246.1-2 (1998), pp. 1–6. DOI: 10.1016/S0375-9601(98)00516-7.

[37] S. Ghosh et al. "Distinguishability of maximally entangled states". In: *Physical Review A—Atomic, Molecular, and Optical Physics* 70.2 (2004), p. 022304. DOI: 10.1103/PhysRevA.70.022304.

[38] V. S. Sambhaje, S. Sinha, and A. Chaurasia. "Entanglement of Bell Diagonal States Induced by Quantum Channels". In: *2023 International Conference on Computing, Communication, and Intelligent Systems (ICCCIS)* (2023), pp. 1029–1034. DOI: 10.1109/ICCCIS60361.2023.10425105.

[39] E. Hecht. *Optics*. 5th ed. Global Edition. Pearson Education Limited, 2017.

[40] W. Demtröder. *Laser spectroscopy 1: basic principles*. Springer, 2014.

[41] W. A. Shurcliff. *Polarized light: production and use*. Harvard University Press, 1962.

[42] S. N. Savenkov. "Jones and Mueller matrices: structure, symmetry relations and information content". In: *Light Scattering Reviews 4: Single Light Scattering and Radiative Transfer* (2009), pp. 71–119. DOI: 10.1007/978-3-540-74276-0_3.

[43] M. Chekhova. *Chekhova research group - Teaching SS2018: Lecture 4.9 - Polarization in Quantum Optics*. Max Planck Institute for the Science of Light. 2018.

[44] D. F. James et al. "Measurement of qubits". In: *Physical Review A* 64.5 (2001), p. 052312. DOI: 10.1103/PhysRevA.64.052312.

[45] N. K. Langford. "Encoding, manipulating and measuring quantum information in optics". PhD thesis. University of Queensland, 2007.

[46] B. N. Simon, C. Chandrashekar, and S. Simon. “Hamilton’s turns as a visual tool kit for designing single-qubit unitary gates”. In: *Physical Review A—Atomic, Molecular, and Optical Physics* 85.2 (2012), p. 022323. DOI: `10.1103/PhysRevA.85.022323`.

[47] R. Simon and N. Mukunda. “Minimal three-component SU(2) gadget for polarization optics”. In: *Physics Letters A* 143.4-5 (1990), pp. 165–169. DOI: `10.1016/0375-9601(90)90732-4`.

[48] M. Passos et al. “Spin-orbit implementation of the Solovay-Kitaev decomposition of single-qubit channels”. In: *Physical Review A* 102.6 (2020), p. 062601. DOI: `10.1103/PhysRevA.102.062601`.

[49] S. G. Reddy et al. “Measuring the Mueller matrix of an arbitrary optical element with a universal SU(2) polarization gadget”. In: *Journal of the Optical Society of America A* 31.3 (2014), pp. 610–615. DOI: `10.1364/JOSAA.31.000610`.

[50] *Scipy Optimize function description: fsolve*. URL: `https://docs.scipy.org/doc/scipy/reference/generated/scipy.optimize.fsolve.html`. (accessed on 24. April 2025).

[51] J. Fiurášek. “Maximum-likelihood estimation of quantum measurement”. In: *Physical Review A* 64.2 (2001), p. 024102. DOI: `10.1103/PhysRevA.64.024102`.

[52] J. Řeháček et al. “Diluted maximum-likelihood algorithm for quantum tomography”. In: *Physical Review A—Atomic, Molecular, and Optical Physics* 75.4 (2007), p. 042108. DOI: `10.1103/PhysRevA.75.042108`.

[53] Y. S. Teo et al. “Quantum-state reconstruction by maximizing likelihood and entropy”. In: *Physical review letters* 107.2 (2011), p. 020404. DOI: `10.1103/PhysRevLett.107.020404`.

[54] Z. Hradil et al. “Maximum-likelihood methods in quantum mechanics”. In: Springer, 2004. Chap. 3 of Quantum state estimation, pp. 59–112. DOI: `10.1007/978-3-540-44481-7_3`.

[55] G. H. Golub and C. F. V. Loan. *Matrix Computations*. 3rd. Baltimore, MD: Johns Hopkins University Press, 1996, p. 55.

[56] R. Jozsa. “Fidelity for mixed quantum states”. In: *Journal of modern optics* 41.12 (1994), pp. 2315–2323. DOI: `10.1080/09500349414552171`.

[57] H. Haeffner et al. “Robust entanglement”. In: *Applied Physics B* 81 (2005), pp. 151–153. DOI: `10.1007/s00340-005-1917-z`.

[58] A. Gilchrist, N. K. Langford, and M. A. Nielsen. “Distance measures to compare real and ideal quantum processes”. In: *Physical Review A—Atomic, Molecular, and Optical Physics* 71.6 (2005), p. 062310. DOI: `10.1103/PhysRevA.71.062310`.

[59] G. Benenti and G. Strini. “Computing the distance between quantum channels: usefulness of the Fano representation”. In: *Journal of Physics B: Atomic, Molecular and Optical Physics* 43.21 (2010), p. 215508. DOI: `10.1088/0953-4075/43/21/215508`.

[60] A. Y. Kitaev, A. Shen, and M. N. Vyalyi. *Classical and quantum computation*. 47. American Mathematical Society, 2002.

[61] *Universität Innsbruck: Distributed Quantum Systems - B. P. Lanyon*. URL: https://www.uibk.ac.at/en/exphys/research/dqs/. (accessed on 31. October 2025).

[62] V. Krčmarský. "A Trapped-Ion Quantum Network over 230 m". PhD thesis. University of Innsbruck, 2023.

[63] J. Schupp. "Interface between Trapped-Ion Qubits and Travelling Photons with Close-to-Optimal Efficiency". PhD thesis. University of Innsbruck, 2021.

[64] M. Meraner. "A Photonic Quantum Interface between Trapped Ions and the Telecom C-Band". PhD thesis. University of Innsbruck, 2022.

[65] M. Canteri et al. "Photon-Interfaced Ten-Qubit Register of Trapped Ions". In: *Physical Review Letters* 135.8 (2025), p. 080801. DOI: 10.1103/v5k1-whwz.

[66] H. Hainzer. "Laser locking for trapped-ion quantum networks". Master thesis. University of Innsbruck, 2018.

[67] A. Winkler. "Frequency Stabilization of a 729 nm Ti:Sa Laser for Qubit Manipulation in Trapped Calcium Ions". Master thesis. University of Innsbruck, 2023.

[68] *Scontel catalog for low-noise detectors (2021)*. URL: https://www.scontel.ru/wp-content/uploads/2021/06/Catalog-2021v2.pdf. (accessed on 1. July 2025).

[69] P. Schindler. "Frequency synthesis and pulse shaping for quantum information processing with trapped ions". Master thesis. University of Innsbruck, 2008.

[70] *Universität Innsbruck - AG Quantum Optics and Spectroscopy: Simulating 2D Spin Lattices with Ion Crystals*. URL: https://quantumoptics.at/en/research/2d-crystals.html. (accessed on 11. June 2025).

[71] P. Barton et al. "Measurement of the lifetime of the $3d^2D_{5/2}$ state in $^{40}\mathrm{Ca}^+$". In: *Physical Review A* 62.3 (2000), p. 032503. DOI: 10.1103/PhysRevA.62.032503.

[72] A. Kramida et al. NIST Atomic Spectra Database https://physics.nist.gov/asd. National Institute of Standards and Technology, Gaithersburg, MD. 2024.

[73] J. Jin and D. Church. "Precision lifetimes for the Ca^+ $4p^2P$ levels: Experiment challenges theory at the 1% level". In: *Physical review letters* 70.21 (1993), p. 3213. DOI: 10.1103/PhysRevLett.70.3213.

[74] D. Leibfried et al. "Quantum dynamics of single trapped ions". In: *Rev. Mod. Phys.* 75 (2003), pp. 281–324. DOI: 10.1103/RevModPhys.75.281. URL: https://link.aps.org/doi/10.1103/RevModPhys.75.281.

[75] C. Law and H. Kimble. "Deterministic generation of a bit-stream of single-photon pulses". In: *Journal of Modern Optics* 44.11-12 (1997), pp. 2067–2074. DOI: `10.1080/09500349708231869`.

[76] A. Stute et al. "Tunable ion-photon entanglement in an optical cavity". In: *Nature* 485.7399 (2012), pp. 482–485. DOI: `10.1038/nature11120`.

[77] J. Helgert. "Radio frequency control of a trapped-ion quantum network node". Master thesis. University of Innsbruck, 2024.

[78] J. Schupp et al. "Interface between Trapped-Ion Qubits and Traveling Photons with Close-to-Optimal Efficiency". In: *PRX Quantum* 2 (2021). DOI: `10.1103/PRXQuantum.2.020331`.

[79] V. Krutyanskiy et al. "Polarisation-preserving photon frequency conversion from a trapped-ion-compatible wavelength to the telecom C-band". In: *Applied Physics B* 123.9 (2017), p. 228. DOI: `10.1007/s00340-017-6806-8`.

[80] M. M. Choy and R. L. Byer. "Accurate second-order susceptibility measurements of visible and infrared nonlinear crystals". In: *Physical Review B* 14.4 (1976), p. 1693. DOI: `10.1103/PhysRevB.14.1693`.

[81] E. Arenskötter et al. "Telecom quantum photonic interface for a $^{40}\mathrm{Ca}^{+}$ single-ion quantum memory". In: *npj Quantum Information* 9.1 (2023), p. 34. DOI: `10.1038/s41534-023-00701-z`.

[82] *LightMachinery: Etalon designer tool.* URL: `https://lightmachinery.com/optical-design-center/etalon-designer/`. (accessed on 26. September 2025).

[83] S. Stopiński et al. "Optical Time Domain Reflectometer Based on Application Specific Photonic Integrated Circuit". In: *2019 Conference on Lasers and Electro-Optics Europe and European Quantum Electronics Conference* (2019), p. 1. DOI: `10.1109/CLEOE-EQEC.2019.8872144`.

[84] *Thorlabs: Glan-Laser Calcite Polarizers - Specs.* URL: `https://www.thorlabs.com/newgrouppage9.cfm?objectgroup_id=815&pn=GL10`. (accessed on 11. September 2025).

[85] *Thorlabs: Polarimeter Systems with High Dynamic Range, Operating Principle.* URL: `https://www.thorlabs.com/newgrouppage9.cfm?objectgroup_id=1564`. (accessed on 24. April 2025).

[86] *INNET - Das Datennetz der Uni Innsbruck - Ein Überblick.* URL: `https://www.uibk.ac.at/zid/netz-komm/innet-e/uebersicht.html`. (accessed on 9. October 2025).

[87] *Suntimes: sunset and sunrise time calculation in Python.* URL: `https://pypi.org/project/suntimes/`. (accessed on 1. July 2025).

[88] *TAWES UIBK: routine meteorological station operated by Zentralanstalt für Meteorologie und Geodynamik.* URL: `https://acinn-data.uibk.ac.at/pages/tawes-uibk.html`. (accessed on 1. July 2025).

[89] *Quantum Opus: Product information*. URL: https://www.quantumopus.com/web/product-info/. (accessed on 22. September 2025).

[90] Zentralanstalt für Meteorologie und Geodynamik (ZAMG) and Department of Atmospheric and Cryospheric sciences (ACINN), Universität Innsbruck. *ACInn Station Portal: Download of meteorological raw data (outdoor air temperature and other meteorological variables)*. https://acinn-data.uibk.ac.at/station/1/RAWDATA/. 2025.

[91] I. G. Hughes and T. P. A. Hase. *Measurements and their Uncertainties: A Practical Guide to Modern Error Analysis*. Oxford University Press, 2010.

[92] *Thorlabs S148C - Integrating Sphere Photodiode Power Sensor*. URL: https://www.thorlabs.com/thorproduct.cfm?partnumber=S148C. (accessed on 14. July 2025).

[93] *Socket Programming in Python (Guide)*. URL: https://realpython.com/python-sockets/. (accessed on 12. September 2025).

[94] *Python - Forest Benchmarking Documentation: Superoperator Transformations*. URL: https://forest-benchmarking.readthedocs.io/en/latest/operator_tools/transform.html. (accessed on 24. July 2025).

[95] *Corning SMF-28 ULL Optical Fiber Portfolio - Product Information*. URL: https://www.corning.com/media/worldwide/coc/documents/Fiber/product-information-sheets/PI-1470-AEN.pdf. (accessed on 3. September 2025).

[96] J. Yin et al. "Experimental quasi-single-photon transmission from satellite to earth". In: *Opt. Express* 21.17 (2013), pp. 20032–20040. DOI: 10.1364/OE.21.020032.

[97] N. Metropolis and S. Ulam. "The Monte Carlo Method". In: *Journal of the American statistical association* 44.247 (1949), pp. 335–341. DOI: 10.1080/01621459.1949.10483310.

[98] B. Efron and R. Tibshirani. "Bootstrap Methods for Standard Errors, Confidence Intervals, and Other Measures of Statistical Accuracy". In: *Statistical Science* (1986), pp. 54–75. DOI: 10.1214/ss/1177013815.

[99] H.-J. Briegel et al. "Quantum repeaters: the role of imperfect local operations in quantum communication". In: *Physical Review Letters* 81.26 (1998), p. 5932. DOI: 10.1103/PhysRevLett.81.5932.

[100] *Cening Optics: Polarization Beamsplitters*. URL: https://www.cn-optics.com/products/PBS.asp. (accessed on 11. September 2025).

[101] *Forest-Benchmarking: Superoperator representations - Choi to Kraus*. URL: https://forest-benchmarking.readthedocs.io/en/latest/superoperator_representations.html#choi-to-kraus. (accessed on 6. May 2025).

[102] J. A. Miszczak. "Singular value decomposition and matrix reorderings in quantum information theory". In: *International Journal of Modern Physics C* 22.09 (2011), pp. 897–918. DOI: 10.1142/S0129183111016683.

[103] *Arduino: Installing Standard Firmata*. URL: https://www.instructables.com/Arduino-Installing-Standard-Firmata/. (accessed on 12. September 2025).

[104] *8MPR16-1 - Motorized Polarizer Rotator*. URL: https://www.standa.lt/products/catalog/motorised_positioners?item=613. (accessed on 12. September 2025).

Acknowledgements

I would like to express my heartfelt thanks to all the people who supported me throughout my studies here in Innsbruck. Without your encouragement, help, and moral support, completing my studies would have been much more difficult.

First and foremost, I would like to thank Ben Lanyon for giving me the opportunity to be part of his Distributed Quantum Systems group at the University of Innsbruck (DQS) and for providing such valuable insights into the various experiments conducted in his lab. He is not only a dedicated scientist but also an excellent teacher. I am grateful for his extensive and incredibly fast feedback, as well as his constant availability for discussions.

I am particularly grateful to my office-mates Viktor Krutianskii, who eventually became my second supervisor, and Fabitha Kodakkat for always answering my questions and assisting me in the lab. Thank you, Marco Canteri and James Bate, for helping me with data analysis and for explaining the operation of the ion trap. I would also like to thank Armin Winkler, Pascal Wintermeyer, Yash Wath, and Felix Bernecker for the fruitful discussions and the positive atmosphere. Thanks to your passion for science, the long days in the lab were not so long. I would also like to thank the former members of the DQS group for successfully setting up DQS1, which we can use even after their departure. A special thanks goes to Vojtěch Krčmarský, who laid the groundwork for polarisation drift compensation and supported me in getting started with it.

My gratitude extends to the members of the Quantum Optics and Spectroscopy group, founded by Rainer Blatt, and the Quantum Interfaces group, led by Tracy Northup. I could always count on your help when needed, and I learned a great deal from you all.

I want to thank the staff at the Institute of Experimental Physics at the University of Innsbruck, without whom the scientific work would not be possible in its present form: Wolfgang Kuen, Kilian Prokop, and Ronny Njoroge Wehinger from the electronics laboratory, as well as Christoph Wegscheider, Anton Schönherr, and Lukas Market from the mechanical workshop. A special thank you goes to Claudia Mevenkamp for her support on the administrative side, as well as for her patience and kindness. I would also like to thank the employees of the ZID, especially Thomas Wachtler and René Fischer, and the employees of the University and State Library, especially Hartwig Musenbichler and Jürgen Tomasi.

Finally, I would like to thank my parents for their unwavering support, for encouraging me through difficult times, and for supporting my decision to study physics, a field that is uncharted territory for our family. *De gra per dut!* I am also deeply grateful to my long-standing friends from Val Gardena and to all the friends I made in Innsbruck, especially Hannah and Sebi[89], and Matthias.

Part of the language editing and grammar correction was supported by the use of ChatGPT (OpenAI) and Grammarly.

---

[89] Sebastian Spreitzer taught me how to use the quantum geographic information system (QGIS), which I used to make Figure 1.1.